universität wien

MAGISTERARBEIT

Titel der Magisterarbeit

X Herculis and TX Piscium: The interaction of their stellar winds with the ISM observed by Herschel

Verfasser

Andreas Mayer, Bakk.

angestrebter akademischer Grad

Magister der Naturwissenschaften (Mag.rer.nat.)

Wien, 2011

Contents

Kurzbeschreibung

Diese Arbeit beschäftigt sich mit der Wechselwirkung stellarer Winde von Asymptotic Giant Branch (AGB) Sternen mit dem Interstellaren Medium (ISM). Ein Stern mit kleiner oder mittlerer Masse erreicht am Ende seines Sternlebens den AGB, eine Region im Hertzsprung-Russell-Diagramm (HRD) der kühlen Temperaturen und hohen Leuchtkräfte. Sterne auf dem AGB haben im Inneren ihr Wasserstoff zu Helium fusioniert und anschließend das Helium zu Kohlenstoff und Sauerstoff. Der Fusionsprozess im Kern ist aufgrund mangelnder Masse abgeschlossen. Jedoch bilden sich Brennschalen um den Kern, welche die Sternatmosphäre expandieren lassen und der Stern verliert einen Großteil seiner Masse in Form eines staubreichen Sternenwindes. Im Normalfall, wenn der Stern relativ zu seinem umgebenden Medium in Ruhe steht, bildet der Sternwind eine sphärisch symmetrische Hülle. In einigen Fällen bewegt sich der AGB Stern jedoch relativ zum ISM und es bildet sich eine Stoßfront in Bewegungsrichtung und die Hülle wird stark deformiert. Bislang wurde dies nur bei einer Handvoll AGB Sternen beobachtet, doch mit den neuen Beobachtungen des Herschel-Satelliten zeigt sich die Vielfalt dieser Objekte. Besonders facettenreich sind die Hüllen von X Herculis und TX Piscium, die in der vorliegenden Diplomarbeit analysiert werden.

In der Einleitung wird die theoretische Grundlage der Interaktion und die Beobachtungen in anderen Sternklassen behandelt. Im Folgenden wird näher auf die beiden Sterne X Her und TX Psc eingegangen und ihre Bewegungsgeschwindigkeit berechnet, bevor die Analyse der Beobachtungsdaten erfolgt. Es werden Schlüsse aus den vorliegenden Strukturen gezogen und eine Temperaturabschätzung einzelner Regionen gemacht. Das letzte Kapitel beschäftigt sich mit Simulationen zur Interaktion des Sternwindes mit dem ISM. Die analytische Lösung der Hüllenform wird an den beiden Sternen modelliert und Abweichungen mit Instabilitäten verglichen, die numerische Modelle zeigen.

Die vorliegende Arbeit entstand im Rahmen des MESS-Konsortiums in Zusammenarbeit mit Alain Jorissen, Franz Kerschbaum, Sophie van Eck, Roland Ottensamer, Toshiya Ueta, Joris Blommaert, Leen Decin, Martin Groenewegen, Josef Hron, Walter Nowotny, Hans Olofsson, Thomas Posch, Lorant Sjouwerman, Bart Vandenbussche und Christoffel Waelkens und ist zusammengefasst vor kurzem in Astronomy & Astrophysics erschienen (Jorissen et al. 2011).

Abstract

This work deals with the interaction of the stellar wind of an Asymptotic Giant Branch (AGB) star with the interstellar medium (ISM). A star with low or intermediate mass moves at the end of his evolution process towards the AGB, a region in the Hertzsprung-Russell diagram (HRD) of cool temperatures and high luminosities. Stars on the AGB have burnt all their hydrogen in the core to helium and subsequent the helium to carbon and oxygen. The mass of these stars is too low to assemble other elements and the fusion process in the core is completed. However, burning shells around the core take over the fusion process and the stellar atmosphere expands and expels most of the stellar mass in form of a dust enriched stellar wind. Normally, when the star is at rest with the ambient medium, the stellar wind forms a spherically symmetric circumstellar envelope (CSE). In some cases, however, the star moves with a certain speed relative to the ISM and forms a shock front in direction of the space motion and the CSE is significantly distorted. Up to now, these structures were observed only for a handful of AGB stars, but new observations from the Herschel Space Observatory show a great variety of interaction shapes. Diverse structures are observed around the stars X Herculis and TX Piscium, which are discussed in this thesis.

The introduction will give insight to the theoretical concept of the stellar wind - ISM interaction and previous observations. In the following X Her and TX Psc are discussed in more detail and the space velocities of both stars are calculated before the analysis of the observational data begins. After the data reduction conclusions are drawn from the observed CSE structures and a temperature is estimated for specific regions. In the last chapter simulations and models for the interaction scenario are shown. The analytic solution for the shape of the interaction zone is fitted to the observations and deviations are compared with instabilities that arise in numerical simulations.

The present work was carried out in the framework of the MESS-consortium in collaboration with Alain Jorissen, Franz Kerschbaum, Sophie van Eck, Roland Ottensamer, Toshiya Ueta, Joris Blommaert, Leen Decin, Martin Groenewegen, Josef Hron, Walter Nowotny, Hans Olofsson, Thomas Posch, Lorant Sjouwerman, Bart Vandenbussche and Christoffel Waelkens and a short version was recently released in Astronomy & Astrophysics (Jorissen et al. 2011).

Danksagung/Acknowledgement

First, I would like to thank Franz Kerschbaum for giving me the opportunity to work on this exciting topic and for the mentoring of this thesis. There was always an open door and (almost) no question remained unsolved. To the same degree I thank Alain Jorissen for inviting me to Brussels and the productive time there. This great collaboration made the thesis even possible!

Furthermore there are people who also contributed to this work and shouldn't remain unnamed: Roland Ottensamer, Marko Mecina and Armin Luntzer helped a lot with the data reduction and the Wilkin fit, Sophie van Eck added some precious scientific comments and Verena Baumgartner spent hours for the time-consuming proofreading. Thank you for all the help!

Und nicht zuletzt geht auch ein Dank an alle Freunde und meine Eltern für die großartige Unterstützung! Ohne Euch wäre das Studium kein Spaß und nicht möglich gewesen.

1. Introduction

1.1. The Herschel Space Observatory

The results that are presented in this work are based on observations with the Herschel Space Observatory, in short *Herschel* (Pilbratt et al. 2010). Herschel[1] is one of the cornerstone missions of the European Space Agency's (ESA) long-term policy plan Horizon 2000. It was primary proposed in 1982 under the name Far InfraRed and Sub-millimetre Telescope (FIRST) but then renamed in the year 2000 to Herschel. In the following years the industrial production of the space observatory began and Herschel was finally launched together with the Planck spacecraft with an Ariane 5 ECA rocket on the 14th of may 2009 from the Guiana Space Centre in French Guiana. Until mid-july 2009 Herschel manoeuvred to its final parking position at the second Lagrangian point (L2), where the gravitational forces of the sun and earth balance the centrifugal force on the satellite. The L2 is approximately 1.5 million kilometres away from the earth.

The main reason to observe from space is the absence of atmospheric disturbances that affect all ground-based observations. In the infra-red (IR), where Herschel is observing, it is also the emission of the atmosphere that has bad influence on the observations. The location of the L2, with sun, earth and moon on one side, provide the telescope with thermal stability which is of special importance for observations in the IR and sub-millimetre region. Together with a low telescope emission this is a key factor for sensitive photometric observations.

As mentioned, Herschel is an infra-red space telescope and so filling the shoes of successful IR space missions like the Infrared Astronomical Satellite (IRAS), the Infrared Space Observatory (ISO), Spitzer and Akari. The advantage of Herschel is that it offers a much better resolution due to a significantly larger aperture and with its wavelength range from approximately 55 to 671 μm it is the first IR space facility that discovers a wavelength region beyond 200 μm. The main components of the space craft and its abilities are shown in the next

---

[1] A detailed description of the Herschel mission can be found at `http://herschel.esac.esa.int/Publ/2008/SPIE2008_Herschel_paper.pdf` which is also the background for this section.

4

paragraphs.

Observing the infra-red wavelength regime means to observe the cool parts of the universe. A body with a temperature of about 5–50 K emits radiation that peaks in the wavelength range for which Herschel is sensitive. This continuum radiation mainly comes from the thermal emission of small dust grains that are heated up by the absorption from shorter wavelength radiation. But also cool gases with a temperature of 10 to a few hundred Kelvin show their brightest atomic and molecular lines in the infra-red. This makes Herschel a tracer for the cooler events in the universe like the early epochs of galaxy formation, the evolving Active Galactic Nucleus (AGN) - starburst symbiosis, the mechanisms that trigger star and planetary formation and also give an insight to the late stages of stellar evolution and the interaction of these stars with the interstellar medium. The present work will discuss the latter topic with the help of Herschel's observations of two objects, TX Psc and X Her.

The main goals of the mission although lie more in the ISM/star formation and galaxy/AGN fields. This is revealed with a look at the 21 Guaranteed Time Key Programmes (GT KPs) which take up 5879 of the 19776 hours that Herschel will spend observing. From this 21 GT KPs ten deal with ISM and star formation, five with galaxies and AGNs, three with cosmology, two with stars and one with the solar system. The Open Time Key Programmes (OT KPs) are distributed in a similar manner and contain 5379 hours of observation. In total, both Key Programmes have an allocated observing time of 11258 hours, 57 % of Herschel's available science time. In July 2010, an Astronomy & Astrophysics special feature with the title *Herschel: The first science highlights* was released which included 152 articles with early results from the Key Programmes.

1.1.1. The spacecraft

Herschel is, with a 3.5 m mirror, the largest infra-red space telescope ever launched and will bear that title until the launch of the James Webb Space Telescope (expected 2015). The spacecraft has a height of 7.5 m and a width of 4 m and had a mass of slightly over 3 tons at the start. It consists of the telescope mirror and two modules, the extended payload module (EPLM) and the service module (SVM). The EPLM houses 2300 litre of liquid helium in a cooling tank, the optical bench with the focal plane units (FPUs) (see Section 1.1.2), the sunshade for the mirror and the payload associated equipment. An artist's impression of Herschel and the devices can be seen in Fig. 1.1. As discussed before, the cooling mechanism is essential for observations in the IR and therefore most of the instruments are cooled with super-fluid helium

Figure 1.1.: Artist's impression of Herschel and the devices. *Image courtesy of ESA.*

down to a temperature of approximately $0.3\,\mathrm{K}$. Herschel relies on the same cryostat technology as ISO did, but with a longer mission lifetime of 3.5 years compared to ISO's 2.5 years. After the 3.5 years the helium is depleted and the cooling of the instruments is no longer ensured. The second module, the SVM, hosts the parts of the spacecraft that don't need to be cooled. These are the power supply, the altitude and orbit control, communication and safety devices and the on-board data handling. Herschel's position in space at L2 has the advantage that earth and sun are always at the same direction making the sunshade an appropriate appliance to keep the mirror at a stable temperature. In shade the telescope operates at a near uniform temperature in the vicinity of $80\,\mathrm{K}$.

The telescope itself is made out of silicon carbide and has a classical Cassegrain design with a primary mirror of $3.5\,\mathrm{m}$ diameter and a secondary with $34\,\mathrm{cm}$. While the secondary mirror is made out of a single piece, the primary mirror is subdivided by 12 segments that are put together to form a monolithic mirror of $3\,\mathrm{mm}$ thickness. Both mirrors are coated with a reflective aluminium layer and covered by silicon oxide for protection. The wavefront error of the system is less than $5.7\,\mu\mathrm{m}$, working at diffraction limit at wavelengths longer than $80\,\mu\mathrm{m}$.
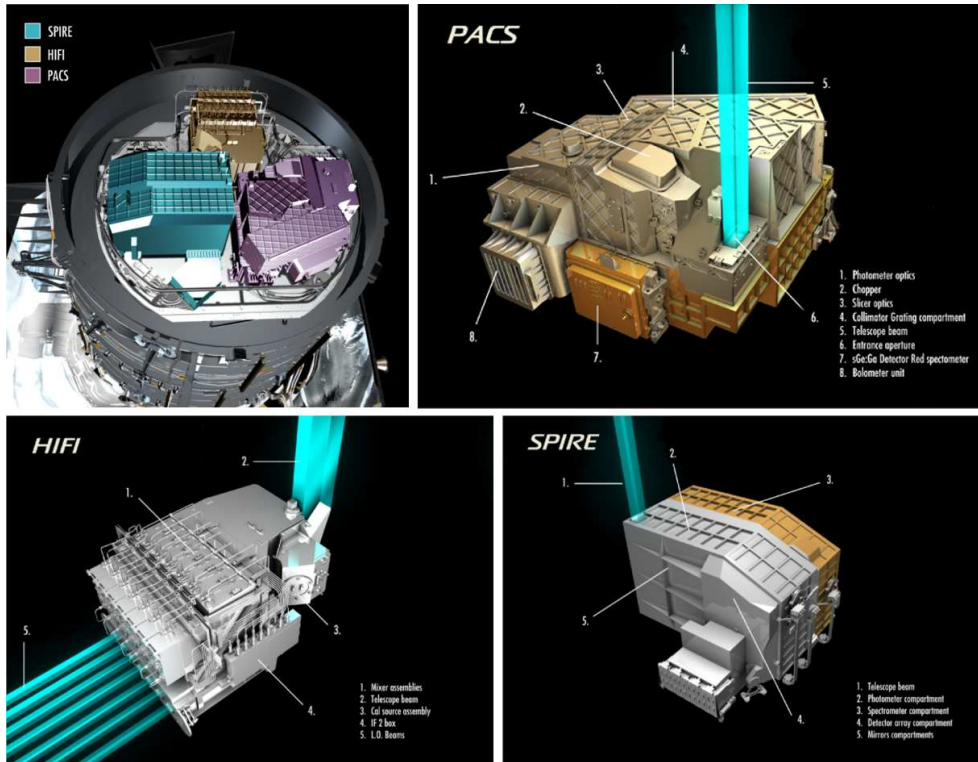
Figure 1.2.: Artist's views of the instruments of Herschel. The upper left panel shows the alignment of the three instruments PACS, SPIRE and HIFI in the focal plane. The panels from upper right to lower left show a close up of PACS, SPIRE and HIFI. *All images courtesy of ESA.*

1.1.2. The instruments

When the light is reflected from the mirrors and collimated to the focal plane three instruments are waiting to detect the incoming beam: the Photoconductor Array Camera and Spectrometer (PACS), the Spectral and Photometric Image REceiver (SPIRE) and the Heterodyne Instrument for the Far-Infrared (HIFI). These instruments are the heart of Herschel. The upper left panel of Fig. 1.2 shows the arrangement of the three instruments in the focal plane.

Photoconductor Array Camera and Spectrometer (PACS)

The observations that are discussed in this work are all obtained with the PACS instrument[2][3]. A detailed view of the device is shown in the upper right panel of Fig.1.2. PACS can be used as an imaging photometer or a low-resolution integral field line spectrometer in the short wavelength part of the IR, operating from 55–$210\,\mu$m. It contains four detector arrays, two bolometer arrays for photometry and two germanium–gallium photoconductor arrays for spectroscopy.

PACS is divided into three mayor segments: the front optics section, the photometer camera and the spectrometer. The front optics section is the first section the beam passes coming from the secondary mirror. It hosts a first blocking filter and the focal plane chopper that switches between the field of view and two calibration sources. After the chopper a mirror splits the beam off to the spectrometer channel or let it pass through to the photometry channels.

In the photometry channel the beam is again split into two channels: two short channels with a bandwidth of 60–$85\,\mu$m (blue) and 85–$130\,\mu$m (green) and a long wavelength channel from 130–$210\,\mu$m (red). The red channel can either be combined with the blue (common) or the green channel for a simultaneous observation. In the blue and green channels the beam hits the short wavelength bolometer array with a size of 64 x 32 pixels and in the red channel the long wavelength bolometer array with a size of 32 x 16 pixels. This corresponds to a field on the sky of $3.2''$ x $3.2''$ per pixel and $6.4''$ x $6.4''$ per pixel for blue/green and red, respectively. Both arrays are divided into a 4 x 2 monolithic sub-array of 16 x 16 pixels each which is then read out after the detection.

In spectroscopy mode the wavelength range of 55–$210\,\mu$m is achieved with a simultaneous observation in two channels. The field of view is $47''$ x $47''$ resolved onto 5 x 5 spatial image pixels. In the integral field unit an image slicer disposes the light through the 1 x 25 pixels entrance slit of the spectrograph after which the Littrow grating disperses the light into an instantaneous 16 pixels spectrum. A dichroic beam splitter feeds the two detectors with light of 55–105 and 105–$210\,\mu$m. The detectors themselves are 25 x 16 pixels Ge:Ga photoconductor arrays.

In the present work only photometric data are used. A description of the observing mode and the data processing can be found in Section 3.1.

---

[2]A full description of PACS can be found in Poglitsch et al. (2010).

[3]The Austrian contribution to PACS is described in Ottensamer & Kerschbaum (2008).

Spectral and Photometric Image REceiver (SPIRE)

SPIRE[4] is the long wavelength equivalent for PACS operating from 194–671 μm. The layout can be seen in the lower right panel of Fig.1.2. SPIRE also works as a photometer and low-resolution spectrometer but other than PACS the photometer observes simultaneously in three spectral bands centred on 250, 350 and 500 μm while the spectrograph is an imaging Fourier-transform spectrometer designed with two overlapping channels.

In the photometry channel two dichroids split the beam into the above mentioned three spectral bands. The light is observed by three feed-horn-coupled neutron transformation doped bolometer arrays containing 43 (500 μm), 88 (350 μm) and 139 (250 μm) detectors.

The spectroscopy channel uses two broadband intensity beam splitters that cut the beam into two overlapping bands of 194–313 μm and 303–671 μm. In the following a Michelson interferometer with a movable mirror (the Fourier transform spectrometer) producing an interferogram in which the spectrum is encoded on the two bolometer arrays. The arrays have a similar architecture as the ones in the photometry channel but with 37 detectors in the short and 19 in the long wavelength array.

Heterodyne Instrument for the Far-Infrared (HIFI)

HIFI[5] is Herschel's high resolution spectrograph with spectral resolution from 300 to 0.03 km s^{-1} and a frequency coverage of 480–1250 GHz in five bands and 1410–1910 GHz in two bands. HIFI's layout can be seen in the lower left panel of Fig.1.2. When observing in the HIFI mode the telescope beam gets split up in 7 sub-beams by a chopper mechanism. In addition a local oscillator creates seven beams in the focal plane unit. The corresponding pairs of beams are then assembled by seven pairs of mixers and amplified by a low-noise IF amplifier box. To avoid unwanted failure modes only one mixer band is operating at a time.

HIFI has implemented two spectrometers, a high resolution (HRS) and a wide-band (WBS) spectrometer. The HRS converts the input signal of the IF amplifier and analyses it in a bandwidth of 235 MHz. The WBS uses a Bragg crystal to disperse the signal of the IF amplifier to a low-power and wideband spectrum.

---

[4]A full description of SPIRE can be found in Griffin et al. (2010).
[5]HIFI is extensively described by de Graauw et al. (2010).

1.2. The MESS Guaranteed Time Key Program

This work is part of Mass-loss of Evolved StarS (MESS) (Groenewegen et al. 2011), one of 21 GT KPs for Herschel, and examines a sample of about 150 evolved stars with imaging and spectroscopy using the PACS and SPIRE instruments. The aim of the program is to study the mass loss history of evolved stellar objects, like asymptotic giant branch (AGB) stars to which X Her and TX Psc belong, but as well post-AGB stars, planetary nebulae (PNe), red supergiants (RSGs), luminous blue variables (LBVs), Wolf-Rayet (WR) stars and supernova remnants (SNRs). Although previous IR satellite missions like IRAS, ISO, Spitzer and AKARI added much to the understanding of the mass loss process, many basic aspects are still poorly understood, e.g. the time dependence of the mass loss rate, the nature of the formed dust species or the shaping of the circumstellar envelope (CSE) due to the interaction with the interstellar medium (ISM). The last mentioned is the topic of the present work.

The MESS GTKP is carried out by a collaboration of universities from Belgium, the UK, Austria, Germany, USA and The Netherlands with an allocated time of 300 hours, from which 170 are spent for imaging and the remaining 130 for spectroscopy. The main aim of the imaging part is the observation of CSE around AGB and RSG stars. The selection of the objects is based on the ISO archive and the IRAS observations of stars showing extended emission and included 300 objects. To cover the various types of evolved stars, 30 oxygen-, 9 sulphur- and 37 carbon-rich AGB and RSG stars were chosen to be imaged with the PACS instrument from the master sample. X Her and TX Psc are part of this selection. From the selection a smaller sub-sample of total 26 objects is in addition observed with SPIRE.

A total number of 33 objects from the imaging selection was also examined in spectroscopy mode with the PACS and SPIRE instruments. While TX Psc is not part of the spectroscopy selection, X Her was observed with the PACS spectrometer. However, the data of this observation are not used for the present work, because the dust composition plays a negligible role in the interaction scenario of a stellar wind with the ISM.

Even though the main aim of MESS are the CSEs of AGB and RSG stars also a notable sample of 20 post-AGB stars and PNe are observed. The aims for these objects are similar to the ones for the AGB stars, namely the imaging of the CSE and the examination of the dust composition through spectroscopy. A small fraction of the guaranteed time is foreseen to examine the dust shells of eight massive stars and to trace newly formed cold dust in five SNRs.

1.3. Asymptotic Giant Branch stars

The field of AGB stars gained more and more attention during the last 25 years after IRAS had opened the view to this stellar class with its infrared full-sky survey in 1984. An essential overview of all science cases regarding AGB stars offers Habing & Olofsson (2004) which is also the basis for the whole section. The term "giant" can be traced back about 100 years to the time when Henry Draper collected data for his famous HD catalogue and some stars showed narrower absorption lines than usual. They were labelled "c" and in the year 1905, Hertzsprung found out that when reducing the stars of the same spectral class to the same apparent magnitude, the c stars have very small proper motions. He concluded that these stars must be very distant and thus more luminous. The term "giant" then appeared in the first Hertzsprung-Russell diagrams (HRDs) by Hertzsprung (1911) and Russell (1914), where some giants are included. This topic was laid to rest for more than 30 years until new observing facilities, with the highlight being the 200-inch telescope opened on Mount Palomar in 1949, offered a giant leap in observation. Also the upcoming electronic devices made numerical calculations for the stellar evolution possible.

Stellar evolution became a very hot topic in the second half of the 20th century. With the new quality of observation also the HRDs got more comprehensive. The position of the giants in the red part of the diagram along a branch was now already known. A question remained: why are these stars so luminous? The correct answer was given by Sandage & Schwarzschild (1952). They were calculating stellar evolution models starting at the end of the main-sequence where the stars have burnt all their hydrogen in their cores to helium. In the models the helium core contracted after the end of the burning phase with a hydrogen envelope around the core expanding towards a larger size. The star became more luminous. It was understood that giant stars must be old stars. One year later Arp et al. (1953) found in the colour-magnitude diagram of the globular cluster M 92 a bifurcation of the red giant branch. This feature became later known as the Asymptotic Giant Branch.

In the following, the evolution of a star up to the end of the AGB phase is discussed as well as the main characteristics of an AGB star. Both observed objects, X Her and TX Psc, are members of this stellar class. This is important because one feature of this class, namely the strong mass loss, is crucial for the whole work.

1.3.1. Stellar evolution, structure and nucleosynthesis

The birth of a star begins with the ignition of hydrogen in its innermost part. The composition of the star is given by the composition of the cloud from which the star forms. This is mainly hydrogen (in the order of over $70\,\%$ of the mass) with a significant part of helium (over $25\,\%$) and a small contamination of heavier elements (less than $5\,\%$), hereafter called metals. With the production of energy through fusion of hydrogen the star reaches the zero-age main sequence on the HRD. The evolution of a $1\,M_\odot$ star from the main sequence until the end of its active life is shown in Fig.1.3 by Lattanzio & Wood (2004). The arrival on the main-sequence is point (1) in the diagram. Lattanzio & Wood (2004) and also Iben (1991) give great overviews of the AGB star evolution and are the base of this section.

The question how stars produce the energy they radiate was a hot topic in the first half of the 20th century. Arthur Stanley Eddington was able to show that stars are spheres of gas in which the gravity and the pressure are in equilibrium. He also predicted that the fusion of hydrogen to helium could be the way how stars produce the pressure to withstand the gravity. When combining four hydrogen atoms to a helium core, the mass balance is not zero because four protons are heavier than a helium core with two protons and two neutrons. The excess mass, or energy, leaves the atom as a gamma-quantum. But Eddington did not succeed to find the mechanism.

The question remained unsolved until 1938, when Carl von Weizsäcker found a cycle where hydrogen can transform into helium with the help of carbon as a catalyst, the so called Carbon-Nitrogen-Oxygen (CNO) cycle. In the main branch of the CNO cycle a proton combines with a pre-existing ^{12}C core and forms ^{13}N which undergoes beta-plus decay to ^{13}C. ^{13}C and a proton then form ^{14}N, which also reacts with another hydrogen core to ^{15}O. ^{15}O is unstable and decays to ^{15}N via beta-plus decay. In about $99\,\%$ the final reaction of the chain is

$$^{15}\text{N} + {}^{1}\text{H} \rightarrow {}^{12}\text{C} + {}^{4}\text{He}. \tag{1.1}$$
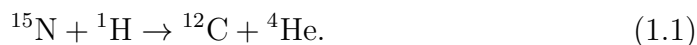
With the recycled ^{12}C the cycle can begin from new. In every reaction of the chain a gamma-quantum leaves the atom core and the result is a conversion of mass into $26.8\,\text{MeV}$ that is leaving the core through radiation in every full cycle. In the remaining $1\,\%$ another cycle forms the helium core over heavier elements. In all cases, however, the yield of the CNO cycle is heavily dependent on the temperature of the core, being proportional to T^{17}. This and the starting temperature of $1.3 \times 10^{7}\,\text{K}$ implicate that only stars above $1.3\,M_\odot$ use the CNO cycle as their main energy producer.
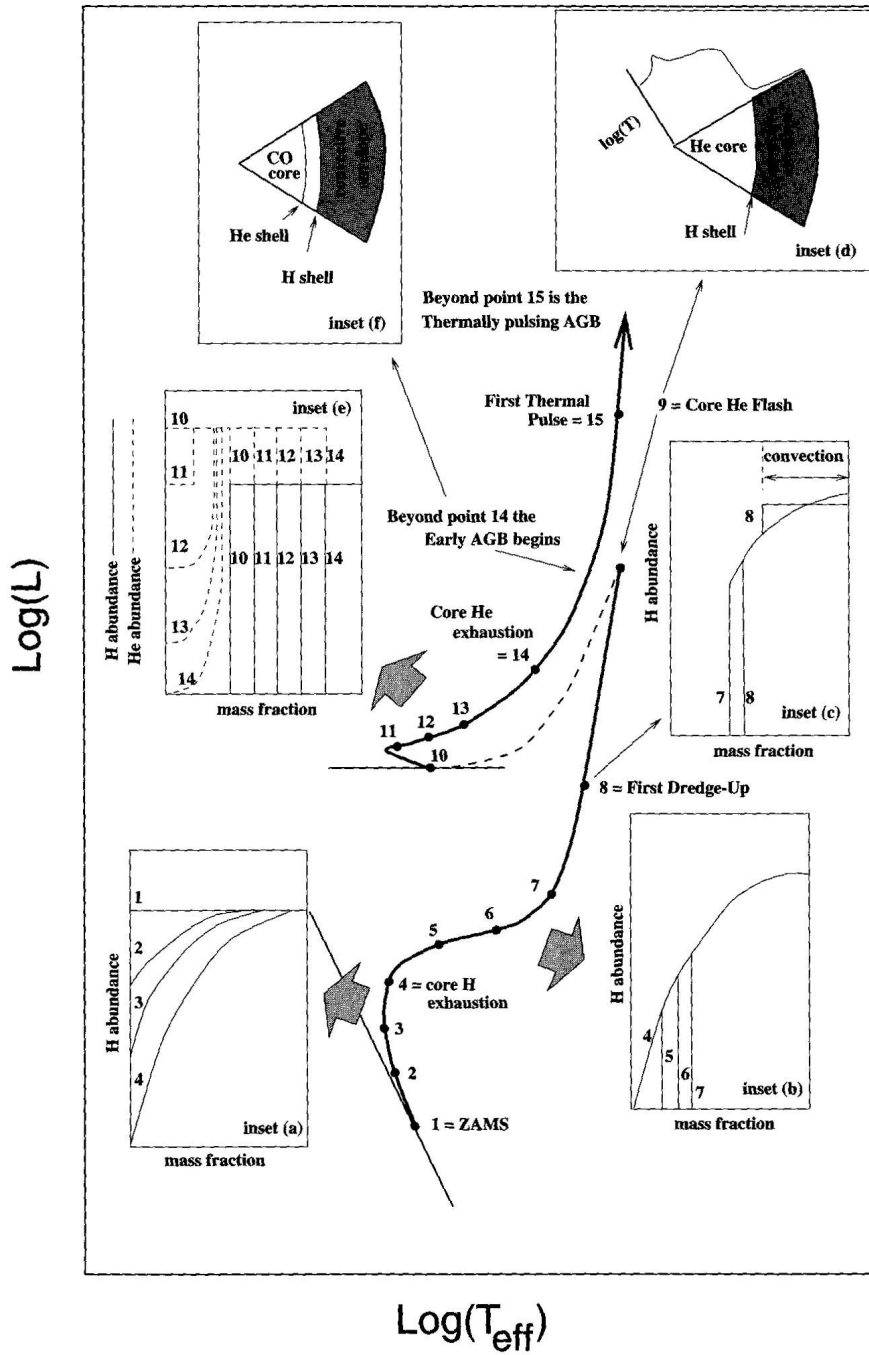
Figure 1.3.: HRD with the evolutionary track of a star with $1\,M_\odot$ from the hydrogen burning at the main sequence until the thermal pulse phase by Lattanzio & Wood (2004). All stages from (1)–(15) are explained in the text below.

One year later Bethe (1939) found the CNO-cycle independently but also another chain, which has a lower starting temperature of 4×10^6 K making it the favoured chain for lower mass stars. This chain doesn't need a catalyst and runs only with hydrogen, the name is therefore Proton-Proton (pp) chain. Because of that the pp-chain is the way helium was formed in the primordial nucleosynthesis and it's also the chain the very first stars used for the energy production since carbon was not available yet.

The pp-chain starts with the fusion of two protons to a deuterium core. This reaction is extremely unlikely and the conversion takes about 10^{10} years. This is the reason for the long and steady lifetime of low mass stars. In terms of the HRD, this reaction makes stars stay long on the main sequence. When deuterium has formed it reacts with a proton to ^{3}He. In the ppI-chain, which is run in 86 %, the last reaction is

$$^3\text{He} + {}^3\text{He} \rightarrow {}^4\text{He} + 2\,{}^1\text{H}. \tag{1.2}$$

In the other 14 %, three other pp-chains, which involve Li, Be and B, produce helium in the core. The dominant ppI-chain produces 26.7 MeV which is radiated away from the nucleus by gamma-quanta which interact with surrounding electrons and protons. This radiation pressure holds the gravity in equilibrium until the hydrogen in the core is exhausted.
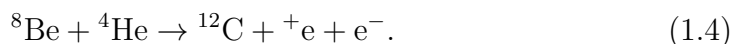
During the hydrogen burning the molecular weight in the core increases and so does the temperature and the pressure. A low mass star which converts hydrogen to helium mostly by the pp-chain moves slightly away from the main sequence towards more luminosity in the HRD. In Fig. 1.3 this is indicated by points (2)–(4). The CNO-cycle and its strong temperature dependence creates strong convection from the outer core region towards the envelope of more massive stars. This changes the opacity and the extent of the core and the star moves to the right in the HRD, towards a higher spectral class.

When the hydrogen in the core of low mass stars is exhausted the core becomes electron degenerate and contracts. The energy production although is given by an active hydrogen burning shell that manifests around the He core expanding the stellar envelope. In the outer layers deep convection zones establish and the star moves towards the Hayashi-line, the boarder of fully convective stars. This happens in points (5)–(7) of Fig. 1.3. Due to the strong convection, isotopes that are part of the CNO cycle, like ^{14}N and ^{13}C are mixed to the surface (Iben 1975). This is called the First Dredge-Up, marked as point (8) in Fig. 1.3.

When the core contracts further the star moves up the giant branch until it reaches a certain temperature and suddenly the helium in the core ignites. This is called the Helium Core Flash, point (9) in Fig. 1.3. All stars over $0.85\,M_\odot$

generate a temperature sufficient to fuse helium. Stars with masses above $2.5\,M_{\odot}$ have no Helium Core Flash because their masses are large enough to ignite the helium right after the exhaustion of hydrogen in the core. In these stars the core is fusing helium while hydrogen is burnt in a shell around the core.

The mechanism of the helium fusion was not understood for a long time because ^{8}Be which is formed from two ^{4}He nuclei instantaneously decays after 6.7×10^{-17} s. The half-life is much shorter than the timespan needed to capture another helium core (Salpeter 1952). It was Fred Hoyle, a famous person in nuclear astrophysics, who predicted a resonance state of ^{12}C and ^{8}Be with the same energy as ^{4}He, which in turn makes the reaction much more possible. By the end of the 1950s both resonances were found by William Fowler. The reaction is known as the triple-alpha process:

$$^4\text{He} + {}^4\text{He} \rightarrow {}^8\text{Be} \tag{1.3}$$

$$^8\text{Be} + {}^4\text{He} \rightarrow {}^{12}\text{C} + {}^+\text{e} + \text{e}^-. \tag{1.4}$$

After the ignition of helium, stars with low masses and low metallicity move directly to the Horizontal Branch while metal-rich stars move to the Red Clump right next to it in the HRD (point (10) in Fig. 1.3). The star is now burning helium in the core with a surrounding hydrogen burning shell. Convection is still active and mixes the produced carbon and oxygen (existing through helium fusion with carbon) to the outer layers (points (11)–(13)). When the helium in the core has completely transformed into carbon and oxygen, stars under $8\,M_{\odot}$ do not have enough core mass to compress the inner part and cause a temperature increase to make the fusion of carbon and oxygen possible. Instead, the core remains inactive and the degeneration leads to cooling when neutrinos carry away the energy. The only energy production of a low mass star occurs in the He-burning shell around the core where the fusion still goes on. This is the beginning of the AGB (point (14) in Fig. 1.3).

In stars with intermediate masses ($> 4\,M_{\odot}$) the beginning of the AGB phase is marked with the establishment of a He-burning shell and the simultaneous extinction of the H-burning shell. Convection penetrates deep into the inactive shell and mixes the products of the H-burning efficiently to the surface but also hydrogen from the envelope inwards. This is called the second dredge-up. After this dredge-up the H-burning shell reignites, the star becomes more luminous and moves up the AGB.

When a low mass star ($< 4\,M_{\odot}$) begins to ascend the AGB with its inactive core the energy of the star is exclusively produced in the He-shell
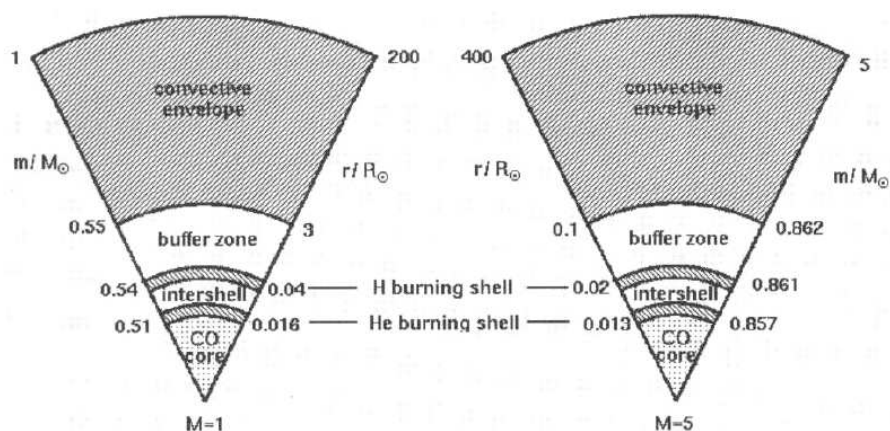
Figure 1.4.: Schematic view of the interior of an AGB star with $1\,M_\odot$ (left panel) and $5\,M_\odot$ (right panel) by Lattanzio & Wood (2004).

around the core and the AGB star becomes susceptible to thermal instabilities (Schwarzschild & Härm 1965). In the first stages of its AGB phase the star burns the He around the core and also the remaining He from the H-burning shell that lies in an intershell between the thick He-layer and the H-shell. A schematic view of the structures of a 1 and $5\,M_\odot$ AGB star is shown in Fig. 1.4. When the He-burning approaches the He-intershell and the intershell becomes thinner the temperature increases in the H-shell and the burning process is essentially enhanced. The H-burning shell is now the primary energy source of the star while the He-burning luminosity decreases and suddenly begins to oscillate due to the positive temperature perturbation from the active H-shell. The energy produced by the triple-alpha process is for a short time larger than the energy the thin shell can remove. This thermal instability is called a *thermal pulse* and is a characteristic trait of an AGB star. The thermal pulse is repeated many times and marks the final stage of a low mass star's life. With every thermal pulse the star loses mass until the energy production in the shells stops and the envelope gets blown away as a planetary nebula with the remaining carbon and oxygen core now known as a white dwarf.

However, this final stage brings a lot of interesting facts about. Iben (1975) and Sugimoto & Nomoto (1975) revealed that the thermal pulses alter significantly the composition of the stellar envelope by having a strong phase of mixing, the third dredge-up. When the He-burning shell is producing an energy over-shoot a convection zone establishes between the He-burning shell and the outer H-shell. This convection zone lasts only for a few hundred years. With the

dilution of the He-burning the convection zone disappears and the intershell region expands and pushes the H-shell outwards to a region of low temperature and density. A mixing of the intershell material, which hosts mainly ^{12}C from the triple-alpha process, with the H-shell occurs. The produced carbon is then picked up by the convective envelope and changes the composition on the surface. Depending on the ratio of elements the star becomes either a carbon star or oxygen rich.

In this mixing process, protons are simultaneously moved from the H-shell down to the He-shell where they fuse with ^{12}C to ^{13}N which decays to ^{13}C. This enriches the He-shell significantly with ^{13}C. In the next dredge-up phase it comes then in contact with helium and another fusion occurs:

$$^{13}\text{C} + {}^{4}\text{He} \rightarrow {}^{16}\text{O} + n. \tag{1.5}$$

This reaction releases a free neutron and is the corner stone for the slow-neutron-capture process (s-process). This process was primary shown in the famous work by Burbidge et al. (1957) where they describe all nucleosynthesis processes in stars. In the s-process the free neutrons react with present nuclei and form neutron-rich isotopes that become even more neutron-rich with every reaction. This works until the core becomes unstable and decays via beta-minus decay, transforming a neutron into a proton. The flux of free neutrons is comparable low, in most cases the time for a neutron capture is much longer than the half-life of the isotope. The reaction path is going along the valley of instability in the table of nuclides and creates elements up to ^{210}Po where the next isotope is unstable towards the alpha-decay with a very short half-life. The result is a cycle between ^{209}Bi and ^{210}Po.

The importance of the s-process is immense as it is together with the r-process, which occurs in supernova explosions, the only major production process of elements heavier than iron. The newly assembled isotopes are removed from the He-shell during the thermal pulses and mixed with material from the convective envelope. The atmosphere of the AGB star and the transition towards a stellar wind are discussed in the next two paragraphs.

1.3.2. Stellar atmosphere and the formation of dust grains

In this paragraph the main features of the atmosphere are discussed. An extensive description of the atmospheres of AGB stars can be found in Gustafsson & Höfner (2004), which is also the base of this paragraph. The stellar atmosphere is in principle the transition region from the optical thick stellar interior to the optically thin outermost stellar layers where photons can leave the star, thus the layers that are visible from outside. For a main sequence star, the structure of the interior is simple with a H-burning core and a spherically symmetric envelope that is in thermodynamic and hydrodynamic equilibrium. Mass flows are not existing and the radiation field is isotropic. This simple picture fails for the atmosphere of an AGB star. With an extension of about $300 \, R_\odot$ the gravity of the system is relatively low and therefore the spherical symmetry is easily disturbed. In addition, mass flows due to the convection in deeper layers don't allow an hydrostatic and isothermal treatment. The temperature in the atmosphere is about 2000–3500 K and the flux peaks in the IR at about 1–3 μm. At this temperatures molecules are able to form and their lines are visible in spectra of AGB stars. Depending on the third dredge-up the observed molecules are either compositions with oxygen, like CO, TiO, H_2O, SiO, OH or carbon compositions like CO, CN, C_2, CH. As CO has the highest binding energy its formation is favoured and after that the other compositions are put together. High resolution spectroscopy of CO lines by Tsuji (1986) showed evidence for turbulent velocity fields in the order of 2–5 km s^{-1} on the surface of AGB stars. This small scale motions cause a turbulent pressure

$$p_\mathrm{t} = \beta_\mathrm{t} \rho v_\mathrm{t}^2,$$ (1.6)

where β_t is a parameter in the order of 0.5–1, ρ the density and v_t the turbulent velocity. After Gustafsson et al. (1975) this leads to an additional pressure term for the pressure scale height

$$H = \frac{R_*^2}{GM} \left(\frac{kT}{m_\mathrm{H}\mu} + \beta_t v_\mathrm{t}^2 \right),$$ (1.7)

where R_* is the stellar radius, M the stellar mass, T the temperature, G the gravitational and k the Boltzmann constant, m_H the atomic mass unit and μ the mean molecular weight. With typical values for AGB stars of $T = 3000 \, \mathrm{K}$, $\mu = 1.4$, $\beta_\mathrm{t} = 0.5$ and $v_\mathrm{t} = 5 \, \mathrm{km \, s^{-1}}$ one finds that the extension of the atmosphere increases due to the additional turbulent pressure by 50 % (Gustafsson & Höfner 2004). The convection that occurs in the interior (see previous paragraph) adds more inhomogeneities to the surface. The hydrodynamic description is not easy since the material gets ionized in the deeper
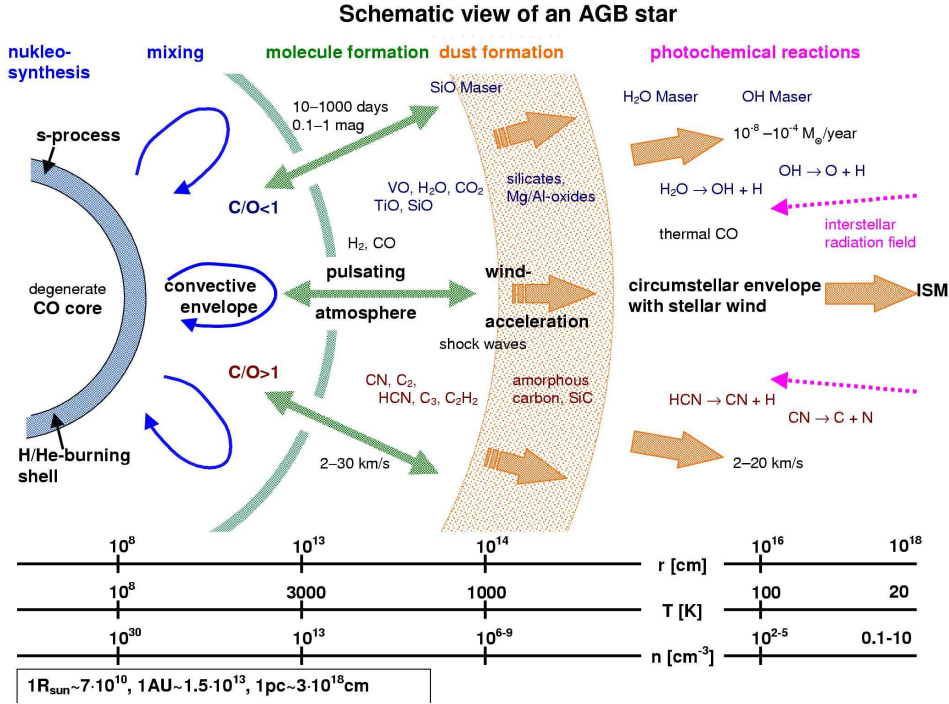
Schematic view of an AGB star

Figure 1.5.: Schematic view of the core, the convective envelope, the atmosphere and the CSE of an AGB star (upper part). Below, the scales of the parts are given. *Image courtesy of J. Hron.*

zones and recombines when dragged to upper layers where it releases energy through radiation. Freytag (2006) carried out 3D hydrodynamic simulations to calculate the influence of the convection on the AGB atmosphere and found convection cells causing huge variable deformations of the stellar surface.

The convection itself is a periodic motion, the layers in the interior are periodically modulated. Near its origin at the stellar interior the motion is slow and subsonic. But with increasing distance the temperature decreases in the stellar atmosphere and thus also the local sound speed decreases and the motion becomes supersonic. With the transition from subsonic to supersonic a strong shock establishes in front of the convective material. A more detailed description of shock fronts is given in Section 1.4.4 where it is needed to describe the stellar wind propagation. In the AGB star the shock front compresses, heats and pushes the gas outward. At the same time the gas is decelerated by the gravity until it reaches steadiness and falls backwards to the center. However, strong shocks are able to propagate through the whole atmosphere and levitate the surface of the AGB star. These strong shock waves are crucial for the

formation of dust.

Due to the decreasing temperature in the outermost layers of the atmosphere complex molecules form from the dredged-up atoms and with enough time these molecules form clusters. If the temperature is low enough more atoms stick to the surface of the cluster than evaporate and the cluster grows with time. When the cluster reaches a size where the properties are those of a solid particle it is called dust grain. The growth rate of a grain is given by

$$R_{\text{growth}} = A_1 \alpha_1 n_1 \frac{1}{4} \langle v \rangle \left(1 - \frac{R_{\text{evap}}}{R_{\text{cond}}} \right), \qquad (1.8)$$

where A_1 is the surface unit, α_1 the sticking coefficient, $\langle v \rangle$ the average speed of a particle, n_1 the number density of monomers, R_{evap} the evaporation and R_{cond} the condensation rate. The growth time can be expressed as

$$t_{\text{growth}} = 3 \frac{a_{\text{gr}}}{a_1} R_{\text{growth}}^{-1}, \qquad (1.9)$$

where a_{gr} is the radius of the grain, a_1 the radius of a monomer. A typical carbon grain has a radius of 10^{-6} cm and contains 10^8 atoms. The growth time of such a particle is about 10^7 s, or about 1.5 years. However, grain formation occurs at a temperature of about 1000 K, higher temperatures would lead to strong evaporation. The ideal grain growth temperature is much lower than the present temperature in the atmosphere, thus the formation of dust grains starts outside the atmosphere at a distance of around $2 \, \text{R}_*$. However, at this distance the density decreases so steeply that the grains can not complete the condensation to become a solid particle.

At this point the shock waves come into play. As discussed before, strong shock waves levitate the surface and alter its structure. A levitation of the surface leads to a sudden decrease in temperature with an increasing density. The temperature falls under the evaporation limit and the high density favours the interaction of atoms with the dust grain. The growth of the dust grain is significantly enhanced. Since the grain growth time ($\approx 10^7$ s) is comparable to the pulsation period of an AGB star, the wake of the shock wave is the ideal spot for dust formation. This theoretical picture was confirmed by interferometric observations by Danchi et al. (1994) who measured the inner radius of dust shells and found them to be only a few stellar radii away from the star.

1.3.3. Mass loss

Losing mass in form of a gaseous outflow is a feature of most stellar classes. The relation for the mass loss rate $\dot{M}$ was derived empirically by Reimers (1975):

$$\dot{M} \propto \frac{L_{\odot}R_{\odot}}{M_{\odot}}, \tag{1.10}$$

where $L_{\odot}$, $R_{\odot}$ and $M_{\odot}$ are the stellar luminosity, radius and mass, respectively. What makes the AGB mass loss special is the high mass loss rate in the order of 10^{-7}–$10^{-4}\,M_{\odot}\,\mathrm{yr}^{-1}$ compared to $10^{-13}\,M_{\odot}\,\mathrm{yr}^{-1}$ of low mass main sequence stars. The wind itself though is very slow compared to other stellar types, only reaching a terminal velocity of typically 5–15 km s^{-1}. A deeper insight to the mass loss topic is given by Bowen (1988) and Gustafsson & Höfner (2004) which is also the base for this paragraph.

Regarding the structure of an AGB star (see Fig. 1.5) the star itself is bound by the atmosphere with a decreasing temperature and density profile where shock waves propagate due to pulsation mechanisms in the stellar interior. Outward the mass outflow forms a region called the circumstellar envelope (CSE) where the outflow reaches its terminal velocity. For an undisturbed outflow the density increases with r^{-2}. The structure of the CSE will be discussed in detail in Section 1.4.2. Between the atmosphere and the CSE lies a transition region with a time-dependent structure where the conditions for the mass loss are set. In this part the gas is accelerated to overcome the local escape velocity.

The mechanisms that drive the mass loss must be outward-directed forces strong enough to exceed the gravitation from the stellar interior. This limits the selection to two forces. The first is the thermal pressure of the gas in the wind forming region which is generated by the radiative heating of the gas. The second is the direct radiation pressure on the outer layers. The radiation from the stellar radiation field gets absorbed which creates an outward directed force.

Here, again, the pulsation and shock waves come into play. As discussed in the previous paragraph shock waves propagate through the star, compress, heat and push the gas outward what levitates the surface. The temperature in the shocked gas drops through radiative cooling and dust formation is enhanced in the cool and dense environment. Solid particles have higher absorption coefficients than gases and therefore the radiative pressure is more effective on dust grains. The grains get pushed outward and drag the surrounding gas with them via momentum transfer and friction. The material is pushed outside the atmosphere with its termination velocity. These winds are called
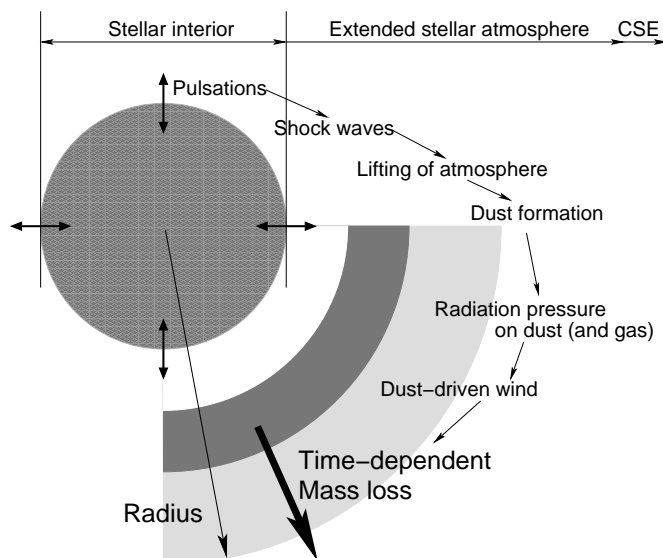
The outer parts of the AGB star

Figure 1.6.: Schematic view of the stellar interior, atmosphere and CSE with the relevant driving mechanisms for mass loss. *Image courtesy of C. Sanders.*

pulsation-enhanced dust-driven winds and it is the most generally accepted theoretical model of mass loss in AGB stars since stellar pulsation alone is not able to produce the high mass loss rates. The importance of radiation pressure for mass loss in AGB stars is quantified in the value β, the ratio of the momentum carried away by the wind to the momentum of the radiation field:

$$\beta = \frac{v_{\text{t}} \dot{M} c}{L}, \tag{1.11}$$

where v_{t} is now the termination velocity and c the speed of light. Knapp (1986) showed in observations of CO emission lines that most stellar winds are optically thin. This means that $\beta < 1$ and the winds are accelerated by the radiation pressure on dust grains.

During the phase when the dust grain leaves the outer layers of the atmosphere the grain growth proceeds further due to the present temperature decrease. The limit is reached when the gas density becomes so low that it slows down the growth completely. The wind forms a CSE according to the dynamics of the outflow, probably with a shell structure and instabilities. The propagation of the stellar wind and its structure are the topics of the next section.

1.4. Stellar winds

In the previous section the composition of the AGB star and the mechanisms of mass loss that are responsible for the stellar wind were discussed. The contents of this section are the structure of a stellar wind and its propagation into the ISM. To get the general aspects of stellar winds the physics are kept simple, any bipolar outflows or instabilities are neglected, the wind expands freely and isotropic as a spherical shell. The structure of this shell is important to understand how the stellar wind - ISM interface obtains its form and structure.

The physical properties of the spherically expanding stellar wind were first described by Parker (1958). The following physical introduction of stellar winds and shock fronts are based on Lamers & Cassinelli (1999); Simis & Woitke (2004); Kippenhahn & Weigert (1994) and a lecture in stellar astrophysics by Ernst A. Dorfi which is in turn based on Parker (1958); Falle (1975) and Weaver et al. (1977).

1.4.1. The wind equation

The wind equation is a relation for the stellar wind flow as a fact of the distance r from the star. The physical description starts as usual in hydrodynamics with the continuity equation

$$\frac{\delta \rho_{\mathrm{w}}}{\delta t} + \frac{1}{r^2} \frac{\delta}{\delta r}(r^2 \rho_{\mathrm{w}} v_{\mathrm{w}}) = 0, \tag{1.12}$$

where ρ_{w} is the density of the stellar wind and v_{w} the wind velocity. The temporary change of mass in a body is equal to the mass flow through the boundary layer of the body. By integrating this equation one obtains the mass loss rate of the body for the stationary case:

$$4\pi r^2 v_{\mathrm{w}} = const. = \dot{M}. \tag{1.13}$$

For the wind flow the equation of motion, also called Euler equation, has to be considered:

$$\rho_{\mathrm{w}} \left(\frac{\delta v_{\mathrm{w}}}{\delta t} + v_{\mathrm{w}} \frac{\delta v_{\mathrm{w}}}{\delta r} \right) = -\frac{\delta P}{\delta r} - \frac{GM\rho_{\mathrm{w}}}{r^2} + F, \tag{1.14}$$

where P is the pressure of the gas and F outward-directed forces like, e.g. the radiation pressure on dust grains that was discussed in the previous section. F is for simplicity reasons set equal zero, although in reality it plays an important role. The motion is therefore only affected by the thermal pressure (first term

on the right side of the equation) and the gravity (second term on the right side). Staying in the stationary case the equation of motion is

$$\rho_{\mathrm{w}} v_{\mathrm{w}} \frac{dv_{\mathrm{w}}}{dr} = -\frac{dP}{dr} - \frac{GM\rho_{\mathrm{w}}}{r^2}. \tag{1.15}$$

Another simplification has to be applied to the temperature of the stellar wind. In the following the wind is set isothermal. AGB winds are far from isothermal, but have a temperature gradient that depends on the distribution of gas and dust. However, the isothermal approach is still good enough to provide a general insight to the topic. In the isothermal case, the pressure can be replaced by the sound speed

$$c_{\mathrm{s}}^2 = \gamma \frac{P}{\rho_{\mathrm{w}}}, \tag{1.16}$$

where γ is the specific heat coefficient of the gas.
Substituting the pressure and the mass loss in the Euler equation leads finally to the important *wind-equation* of an isothermal wind (Parker 1958):

$$\frac{1}{2} \left(1 - \frac{c_{\mathrm{s}}^2}{v_{\mathrm{w}}^2} \right) \frac{dv_{\mathrm{w}}^2}{dr} = -\frac{GM}{r^2} \left(1 - \frac{2c_{\mathrm{s}}^2 r}{GM} \right). \tag{1.17}$$

The equation describes directly the velocity of a wind at a distance r from the star and is valid for all types of stellar winds, not depending on temperature, density, velocity or the mechanism that drives them. An important fact of the equation is that it has a critical point at

$$r = r_{\mathrm{crit}} = \frac{GM}{2c_{\mathrm{s}}^2}, \tag{1.18}$$

where the right side of the wind equation is zero

$$\frac{1}{2} \left(1 - \frac{c_{\mathrm{s}}^2}{v_{\mathrm{w}}^2} \right) \frac{dv_{\mathrm{w}}^2}{dr} = 0. \tag{1.19}$$

The solutions for this equation are

$$\frac{dv_{\mathrm{w}}^2}{dr} = 0 \text{ or } v_{\mathrm{w}} = \pm c_{\mathrm{s}}. \tag{1.20}$$

This leads to six different types of solutions for the wind equation, from which four are stable:
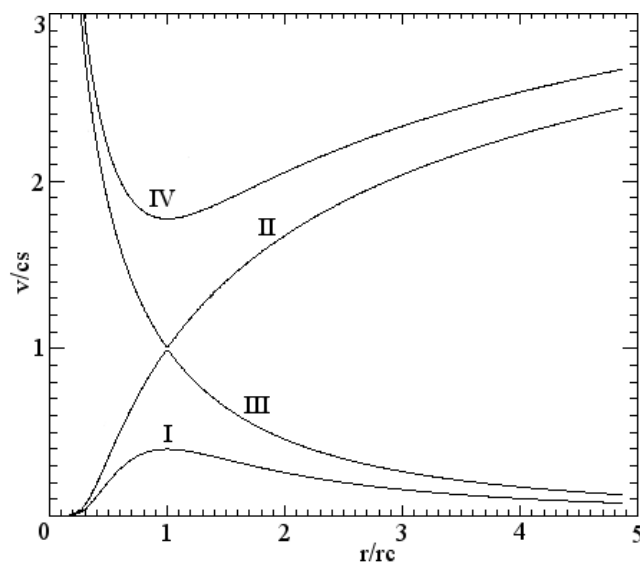
Figure 1.7.: Schematic plot of four possible solutions of the wind equation. Two solutions (I and IV) remain always subsonic or supersonic, solution II and III describe transitions regarding the sound speed. $r_c = r_{crit}$. *Image courtesy of A. Hood.*

- Class I is a very slow wind that is moving sub-sonically. It has a maximum at the critical point but stays subsonic and disappears at infinity.

- Class II is the solution for a stellar wind. The wind starts sub-sonically but gets accelerated and reaches the critical point with a positive tangent. For $x \to \infty$, $y^2 \propto 4 \ln x$ and thus the velocity rises with a finite supersonic velocity at infinity. This seems wrong and is caused by the applied simplification of an isothermal wind. In reality the stellar wind is somewhere limited by a shock wave. At this point the wind leaves the isothermal condition and a fraction of the kinetic energy is transformed into heat. This will be discussed in the next paragraph.

- Class III is the opposite case to Class II: a wind that is supersonically but slowing down and reaching the critical point with a negative tangent. This is the case for an accretion flow onto an object, also known as Bondi-accretion (Bondi 1952).

- Class IV is a very fast wind that is supersonic with a minimum at the critical point but never drops subsonic.

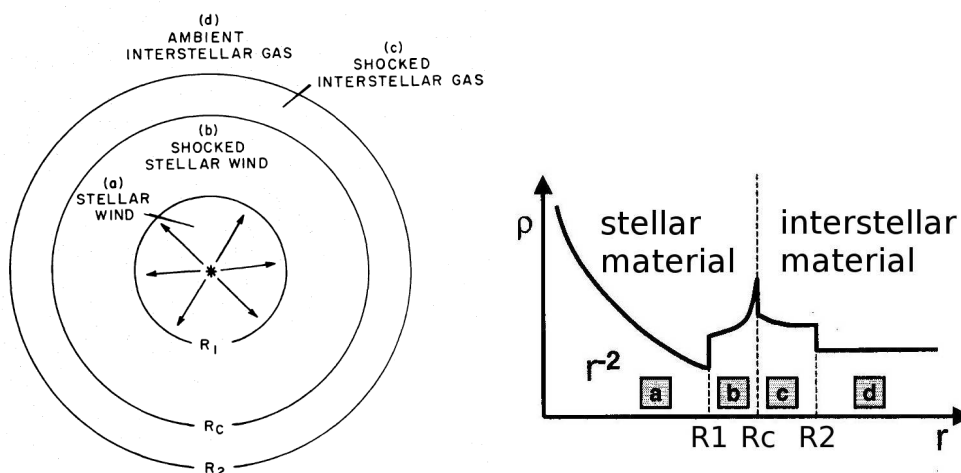A schematic sketch of the solutions can be found in Fig. 1.7.

Figure 1.8.: *Left panel*: Schematic structure of a stellar wind bubble, or CSE, by Weaver et al. (1977). The bubble is divided into four distinct zones and three boundaries. Although this model was derived for massive early type stars with large stellar wind velocities, it is also valid for AGB stars with low wind velocities. *Right panel*: Schematic radial density profile of a stellar wind bubble and the surrounding ISM. The x-axis is the radius, y-axis the density. *Image courtesy of E. Dorfi*.

1.4.2. Structure of a stellar wind bubble

With the wind-equation the general kinematics of the stellar wind with the assumption of free expansion are explained. This is, however, again a simplification as the expanding wind has to work against the ISM that surrounds the star. In the first phase of the stellar wind expansion it has to push away the surrounding medium with the result that the pushed away ISM piles up. This was described by Oort (1951) where the interaction of supernova and nova shells with the ISM are discussed. Today this first phase of expansion is known as Oort's snow plough model. This chapter deals with the structure of the piled up wind. A detailed description of the whole stellar wind structure and the kinematics is provided by Falle (1975) and Weaver et al. (1977).

Due to the pile-up of material the structure of the CSE, or wind bubble, becomes slightly more complicated. A schematic view of the structure is displayed in the left panel of Fig. 1.8. It consists of four regions. In region (a) the stellar wind expands with a velocity higher than the sound speed and with small thermal pressure. The wind velocity can be regarded as constant at

distances larger than a few stellar radii from the star. As the mass loss rate is also constant the density drops simply with r^{-2}. A radial density profile of the wind is shown in the right panel of Fig. 1.8. The boundary of region (a) is a thin shock front R_1, the so called termination shock. It transforms almost all of the kinetic energy of the stellar wind into thermal energy.

The shocked stellar wind region is layer (b) in the figure. The shock compresses the material and radiative cooling lets the density profile rise steeply in the shocked region. The outer boundary of the shocked stellar wind layer is the contact discontinuity R_c. It is the boundary of the stellar wind and the ISM and dissolves by enduring thermal conduction of the stellar wind and the ISM or shows instabilities because of the different density properties of both constituents. This is discussed in more detail in Section 4.2.

Layer (c) displays the piled up density enhanced interstellar gas by the stellar wind. The boarder of this layer is again a shock front, R_2. The free and undisturbed ISM with density ρ_0 is shown as region (d) in the diagram. The expansion of this structure is the topic of the next paragraph.

1.4.3. Expansion of a stellar wind bubble

For the treatment of the wind bubble expansion it is helpful to simplify its four-split structure. The kinetic energy of the gas in layer (a) and (b) is transformed into thermal energy and has the pressure P and a temperature T_s. During the expansion a lot of ISM gets piled up in layer (c) and this layer dominates the mass balance of the wind bubble but its size is very small compared to overall extent. The wind bubble expansion is therefore treated as an expansion of a thin shell. By assuming a constant density inside the shell the momentum of the sphere can be written as

$$\frac{d}{dt}\left(\frac{4\pi}{3}R^3\rho_0\dot{R}\right) = 4\pi R^2 P, \tag{1.21}$$

where ρ_0 is the density of the ISM, R the radius of the wind bubble and $\dot{R}$ its expansion velocity. This gives directly the pressure P inside the shell

$$P = \rho_0\dot{R}^2 + \frac{1}{3}\rho_0 R\ddot{R}. \tag{1.22}$$

Another expression for the pressure is found in the energy balance of the system. The variation of the energy in the wind bubble is equal to the energy $\dot{E}_*$ that the star puts in the system less the energy that the bubble needs to

expand:

$$\frac{d}{dt}\left(\frac{4\pi}{3}R^3\frac{3}{2}P\right) = \dot{E}_* - P\frac{d}{dt}\left(\frac{4\pi}{3}R^3\right).$$
(1.23)

When putting the pressure relation into this term the result is an unhandy differential equation that can be simplified through an ansatz $R(t) = At^\alpha$ with the solution for the coefficients

$$\alpha = \frac{3}{5} \text{ and } A = \left(\frac{125\dot{E}_*}{154\pi\rho_0}\right)^{\frac{1}{5}},$$
(1.24)

or

$$R(t) = \left(\frac{125}{154\pi}\right)^{\frac{1}{5}}\left(\frac{\dot{E}_*}{\rho_0}\right)^{\frac{1}{5}}t^{\frac{3}{5}}.$$
(1.25)

The expansion is proportional to $t^{3/5}$ and is depending solely on the star's output and the density of the ambient medium. The differentiation of this equation leads directly to the expansion velocity of the shell

$$\dot{R}(t) = \frac{3}{5}At^{-\frac{2}{5}},$$
(1.26)

and to its kinetic energy

$$E_{kin} = \frac{1}{2}m\dot{R}^2 = \frac{15}{77}\dot{E}_*t.$$
(1.27)

The energy balance shows that $\frac{15}{77}$ or $19.4\,\%$ of the output of the star is transformed into kinetic energy.

1.4.4. Shock fronts

In the previous paragraph it was found that multiple shock fronts are part of the stellar wind structure. The termination shock is the border of the free flowing stellar wind and drives a shock wave through the stellar wind material. In the outer region a second shock front separates the piled-up ISM and the free flowing ambient medium. A brief discussion about the basic physics of shock fronts is important to understand the following section about stellar wind bow shocks.

A shock front can be seen as an expansion of a discontinuity that changes the medium irreversible. The propagating wave has an infinitesimal thickness in the order of the mean free path. To simplify the physics the equations are in the coordinate system of the shock front moving in direction of the x

coordinate and the system is always stationary. The medium in front of the shock has always the index 0 and after the index 1. The equation of continuity in the common form is given by

$$\int_V \nabla \cdot (\rho u) = \oint_O \rho u \, df = 0, \tag{1.28}$$

where ρ is the density of the fluid and u the velocity of the shock and the mass balance is therefore

$$\rho_0 u_0 = \rho_1 u_1. \tag{1.29}$$

Thus, the fluid is less dense and the shock front faster before the shock and denser and slower afterwards. The momentum balance brings in the pressure:

$$\rho_0 u_0^2 + P_0 = \rho_1 u_1^2 + P_1, \tag{1.30}$$

where $\rho \, u^2$ is the ram pressure on the surface. The energy balance is given by

$$\epsilon_0 + \frac{P_0}{\rho_0} + \frac{u_0^2}{2} = \epsilon_1 + \frac{P_1}{\rho_1} + \frac{u_1^2}{2}, \tag{1.31}$$

where P/ρ is the work that the system performs on the expansion and $\frac{u^2}{2}$ is the kinetic energy. The term $\epsilon + \frac{P}{\rho}$ is also known as the enthalpy h for an ideal gas and can be written as

$$h = \epsilon + \frac{P}{\rho} = \frac{\gamma}{\gamma - 1} \frac{P}{\rho} = \frac{\gamma}{\gamma - 1} \frac{kT}{m}, \tag{1.32}$$

where k is the Boltzmann-constant of the gas. The simplified form of the energy balance is then

$$h_0 + \frac{u_0^2}{2} = h_1 + \frac{u_1^2}{2}. \tag{1.33}$$

The equations for continuity, momentum and energy balance are also called *Rankine-Hugoniot conditions* and contain six unknown parameters: pressure, density and velocity each before and after the shock front. The solution of the equations give direct relations of the conditions before and after the shock. This is achieved by the introduction of the specific volume $V = 1/\rho$. The mass, momentum and energy balance and also the enthalpy term can be rewritten and the relations deduced. For the pressure this is

$$\frac{P_1}{P_0} = \frac{(\gamma + 1)V_0 - (\gamma - 1)V_1}{(\gamma + 1)V_1 - (\gamma - 1)V_0}, \tag{1.34}$$

and for the density and velocity

$$\frac{V_1}{V_0} = \frac{\rho_0}{\rho_1} = \frac{u_1}{u_0} = \frac{(\gamma - 1)P_1 + (\gamma + 1)P_0}{(\gamma + 1)P_1 + (\gamma - 1)P_0}. \tag{1.35}$$

The last relation of interest is the temperature of the system. By assuming an ideal gas the temperature relation is

$$\frac{T_1}{T_0} = \frac{P_1 V_1}{P_0 V_0}. \tag{1.36}$$

For a strong shock the temperature in the shock front can be simplified to

$$T \approx \frac{3\overline{m}v^2}{16k}, \tag{1.37}$$

where $\overline{m} = 10^{-27}$ kg is the mean weight of a particle in the shock front, which is mainly composed of hydrogen.

These three relations describe the conditions in regions before and after the shock front. The visualization of the results is the so-called Hugoniot curve which shows that the enthalpy $S \propto lnP/\rho$ increases after the shock and every shock front compresses the gas and raises the pressure.

1.5. Stellar wind bow shocks

1.5.1. Analytic solution

In the previously described case a spherically symmetric shell was established because the star stood at rest with respect to the medium around it. In reality however an AGB star moves typically with a velocity of $30\,\mathrm{km\,s}^{-1}$ through the ISM (Feast & Whitelock 2000) but can reach a space motion as high as $v_* = 125\,\mathrm{km\,s}^{-1}$. For the typical motion the spheric symmetric shell is a good approach but at higher velocities the structure of the bubble differs significantly from spherically symmetric.

This scenario can be described as follows. The structure of the wind bubble is the same as in Section 1.4.2. When the star is moving through the ambient medium the outermost layer is facing highly supersonically the oncoming ISM. This forms a forward shock that propagates into the ISM. The layers in between constantly mix and if the post shock cooling is effective the shell gets compressed with an insignificant thickness compared to the distance to the star. The cooling is discussed in detail in Section 4.2.1. The *bow shock* is then the layer that is bound on the inner side by the termination shock and outside by the forward shock. The shape of the bow shock around the star is akin to the shape of a comet.

The theory of momentum-supported stellar bow shocks was initially brought up by Baranov et al. (1971). They solved numerically the shape of a bow shock produced by the collision of an isotropic stellar wind with a uniform ISM when a star is moving supersonically through the ISM. The theory was applied to HII regions around moving O stars by van Buren et al. (1990); Mac Low et al. (1991) and Raga et al. (1995), to the movement of objects with a magnetic field through a medium (Cordes et al. 1993) and to winds around pulsars (Aldcroft et al. 1992). The first exact analytic solution to this numerical approach was then derived by Wilkin (1996) as well as Wilkin et al. (1997) and is used in various fields of stellar astrophysics to calculate the shape of bow shocks around stars. The here presented description of the theory and analytic solution of stellar wind bow shocks is a summary of the work by Wilkin (1996) which is in turn based on Baranov et al. (1971).

As discussed in Section 1.4.2 the pressure of the stellar wind decreases with the square of the radius and so does the ram pressure of the wind while the ram pressure of the ISM is constant. Therefore, at a certain point the ram pressure of the stellar wind balances the oncoming ISM:

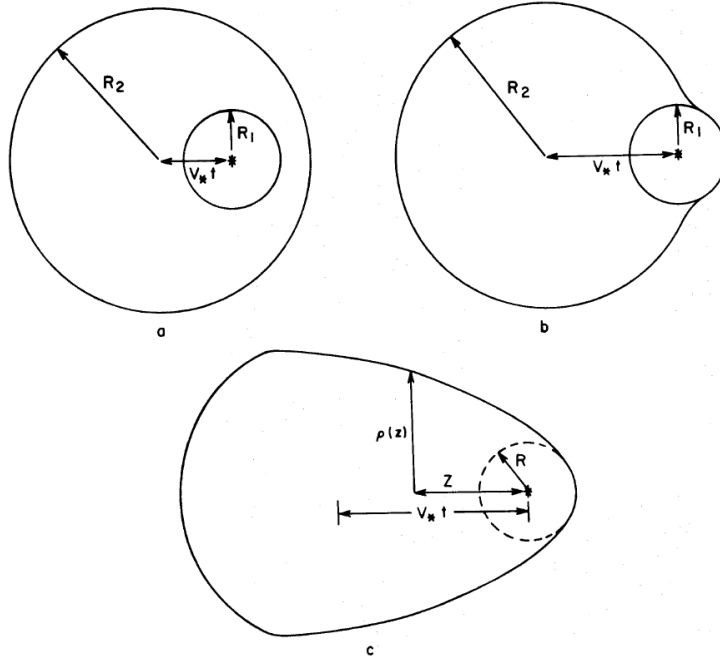$$\rho_{\mathrm{w}} v_{\mathrm{w}}^2 = \rho_0 v_*^2, \tag{1.38}$$

Figure 1.9.: Schematic structure of a stellar wind bubble distorted by the motion of the star. At panel (a) the star has a low space velocity, panel (b) shows the star with an intermediate and panel (c) with a high velocity as stated by Weaver et al. (1977).

or, after Borkowski et al. (1990), written as a critical density of the wind

$$\rho_{\mathrm{w,crit}} \propto \left(\frac{v_* + v_{\mathrm{w}}}{c}\right)^2 \rho_0. \tag{1.39}$$

In Wilkin (1996) the distance of the star to the point of the bow shock where the ram pressure of the wind balances with the ambient medium is called *stand-off distance* R_0. Baranov et al. (1971) found for it

$$R_0 = \sqrt{\frac{\dot{M} v_{\mathrm{w}}}{4\pi \rho_0 v_*^2}}. \tag{1.40}$$

As seen later, the stand-off distance is the scaling factor for the shape of the bow shock.

By switching to a spherical coordinate system the fluxes of mass and momentum crossing an annulus of the shell are given by $\Phi_{\mathrm{m}} = (R\sin\theta)\sigma v_{\mathrm{t}}$ and

$\Phi_t = (R\sin\theta)\sigma v_t^2$, respectively. In steady state the mass traversing a ring of the shell at a polar angle θ from the stand-off point is given by

$$2\pi\Phi_m = \dot{M}\frac{\Omega}{4\pi} + \pi\omega^2\rho_0 v_*, \qquad (1.41)$$

where $\Omega = 2\pi(1 - \cos\theta)$ is the shell solid angle from the axis to a point at an angle θ and $\omega = R\sin\theta$ is the cylindrical radius. From this point on the shape of the bow shock was solved numerically with differential equations by Baranov et al. (1971). The analytic solution is based on the examination of the vector momentum that is deposited by the ambient medium Φ_a and the stellar wind Φ_w on a small wedge $\Delta\phi$ of the bow shock cone. For the stellar wind this can be written as

$$\Phi_w\Delta\phi = \frac{\dot{M}v_w}{8\pi}[(\theta - \sin\theta\cos\theta)\hat{e}_\omega + (\sin^2\theta)\hat{e}_z]\Delta\phi, \qquad (1.42)$$

where $\hat{e}_z$ is the unit vector in z-direction and $\hat{e}_\omega$ the unit vector in direction of the cylindrical radius ω. The momentum flux of the ambient medium that is deposited on the wedge has the form

$$\Phi_a\Delta\phi = -\frac{1}{2}\omega^2\rho_0 v_*^2\hat{e}_z\Delta\phi. \qquad (1.43)$$

The total tangential momentum flux is then the sum of both. In length units of R_0, marked by a tilde, this leads to the equation

$$2\pi\Phi_t = \pi R_0^2\rho_0 v_*^2\sqrt{(\theta - \sin\theta\cos\theta)^2 + (\tilde{\omega}^2 - \sin^2\theta)^2} \qquad (1.44)$$

for the vector momentum flux and to a differential equation

$$\frac{d\tilde{z}}{d\tilde{\omega}} = \frac{\Phi_{t,z}}{\Phi_{t,\omega}} = \frac{-\tilde{\omega}^2 + \sin^2\theta}{\theta - \sin\theta\cos\theta} \qquad (1.45)$$

for the shell's shape. By transforming this equation from the cylindric coordinate system $(\tilde{\omega}, \tilde{z})$ to the more convenient $(\tilde{r}, \theta)$ coordinate system, and finding a suitable substitution the resulting final equation is the exact integral for the shell's shape:

$$R(\theta) = R_0\csc\theta\sqrt{3(1 - \theta\cot\theta)}, \qquad (1.46)$$

where θ is the polar angle from the axis of symmetry as seen from the star, which is at the coordinate origin. Hence, the shape of the bow shock is only linearly depending on the stand-off distance R_0, which means that the shape is simply scaled by the stand-off distance and the outline does not change. Fig. 1.10 shows the shape of the stellar wind-ISM bow shock which is a conic section of the 3D *wilkinoid*.
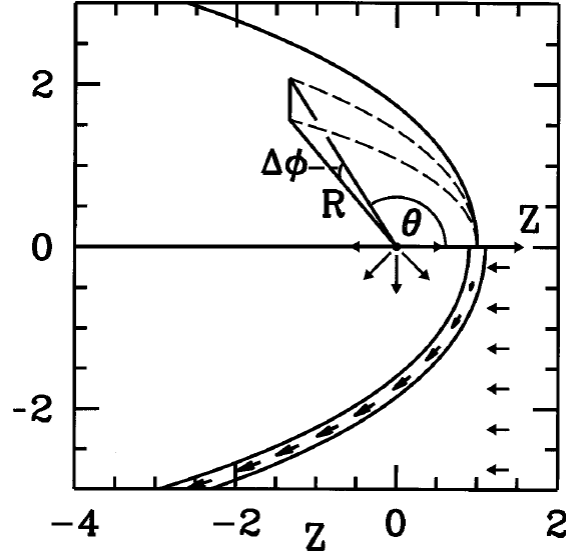
Figure 1.10.: Thin-shell bow shock model by Wilkin (1996). The upper panel
shows the model with the star at the origin and the parameters
R and θ that define the spherical coordinate system. Th lower
panel shows the ambient wind flow and the tangential flow in the
frame of the star.

1.5.2. Previous observations and results

Bow shocks were for the first time proposed around the earth as a product of
the solar wind hitting the earth's magnetosphere and around the sun at the
boarder where the solar wind interacts with the ISM. With the start of the
Explorer and Vela satellite programmes in the late 1950's and early 1960's,
respectively, it was possible to verify the hypothesis of the bow shocks around
earth and sun due to observational evidence (Strong 1968; Greenstadt et al.
1968). Subsequently, Gurzadian (1969) proposed that it should be possible to
observe planetary nebulae that show tail structures and brightened poles as
indication of compression and shear by the motion of the nebula through the
ISM. Baranov et al. (1971) and Smith (1976) numerically solved the shape of
the solar wind and the PN bow shock, respectively. Dyson (1975) described a
scenario where the stellar wind is pushed by a globule in an HII region. The
first observational evidence for bow shocks outside the solar system was shown
by Phillips et al. (1977) with the observation of NGC 6543 where they found
the tails and brightened poles that were predicted by Gurzadian (1969).
The first consideration that also stars that move rapidly through the ISM can
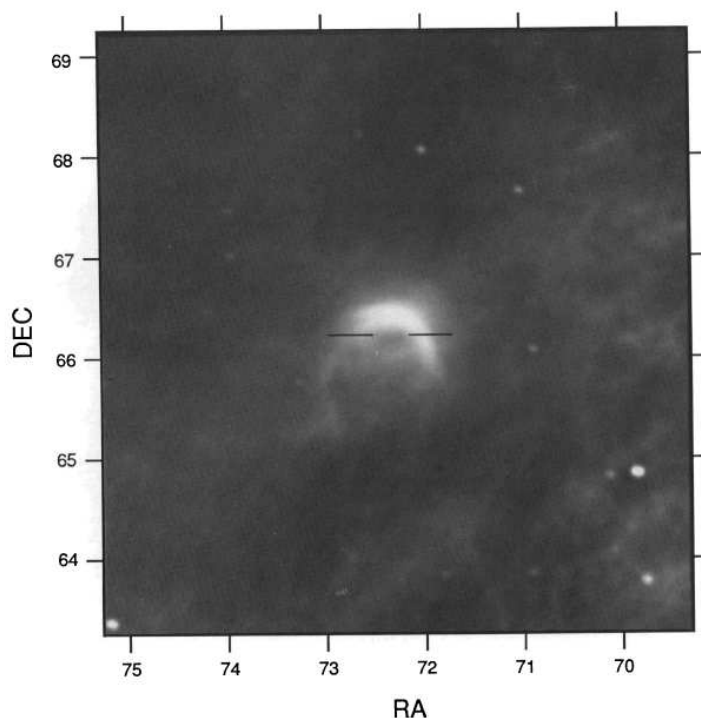
Figure 1.11.: Bow shock structure around α Cam on the IRAS image by van Buren & McCray (1988). The central position of the star is indicated by the two bars.

produce bow shocks was drawn by Falle (1975) and Weaver et al. (1977). They calculated the effect of the large space velocity of an early type OB star on the stellar wind bubble. Their results are distorted wind bubble structures but they do not directly relate the results to a bow shock. A schematic illustration of the distorted wind bubble that is very similar to a bow shock structure is shown in Fig. 1.9. The first stellar wind bow shock was then found by Gull & Sofia (1979) when they observed the runaway O stars LL Ori and ζ Oph at Hβ and recognized arcuate structures around the stars.

Another giant leap in the field of stellar bow shocks was made with the launch of IRAS in 1983. It was the first astronomical IR satellite and provided enormous data at wavelengths that are cut off by the earth's atmosphere. A large number of runaway O stars were observed and van Buren & McCray (1988) found 14 of them showing strong bow shocks. Fig. 1.11 shows the bow shock around α Cam in the IRAS data. In this work the authors also extend the physical picture of stellar wind bow shocks with new details. Based on the

length scale of the point where the ram pressure of the free flowing stellar wind balances with the shocked stellar wind (Weaver et al. 1977)

$$l_1 = 1.74 \text{ x } 10^{18} \ \dot{M}_{*,-6}^{1/2} \ v_{\mathrm{w},6}^{1/2} \ \mu_{\mathrm{H}}^{1/2} \ v_{*,6}^{-1} \ \rho_0^{-1/2} \mathrm{cm}, \tag{1.47}$$

they found for the stand-off distance

$$R_0 \approx 1.47 \ l_1 \tag{1.48}$$

by assuming that the shocked gas between the termination shock and the bow shock does not cool down effectively and the gas has a constant density and temperature.

The swept up ambient material in the bow shock is radiative and the density can be written as

$$n_{\mathrm{shell}} = M^2 n_0, \tag{1.49}$$

where M is the Mach number of an isothermal gas

$$M^2 = \left(\frac{u_0}{c_\mathrm{s}} \right)^2 = \frac{\rho_1}{\rho_0}. \tag{1.50}$$

The upper limit for the displaced mass of ambient medium was given by Borkowski et al. (1990)

$$M_{\mathrm{ISM}} \leq \frac{3}{4} \pi R^3 \rho_0 \begin{cases} \frac{1}{4} \left(2 + \frac{v_*}{v_{\mathrm{exp}}} + \frac{v_{\mathrm{exp}}}{v_*} \right) & v_* \geq v_{\mathrm{exp}} \\ 1 & v_* \leq v_{\mathrm{exp}}. \end{cases} \tag{1.51}$$

Subsequent conclusions made in the work by van Buren & McCray (1988) are all about the surrounding medium that is ionized through the UV radiation of the hot star. These conclusions are not applicable to the extended environment of a cool AGB star.

In addition to the hot runaway O stars IRAS also observed stars in the late stage of their evolution. Stencel et al. (1988) give an overview of about 80 observed RGB stars and OB associations. They focused on the far IR shells of these objects and found about 1/3 of them having extended shells at $60 \, \mu$m, among which is also X Her. Although, the resolution and signal to noise ratio of the images does not allow to derive any morphology apart from spherical, so the authors were only able to distinguish if an object has a dust shell or not and derive the temperature of the dust.

With the launches of ISO in 1995 and Spitzer in 2003 infra-red observation and the field of stellar bow shocks proceeded with big steps. The MIRIAD project
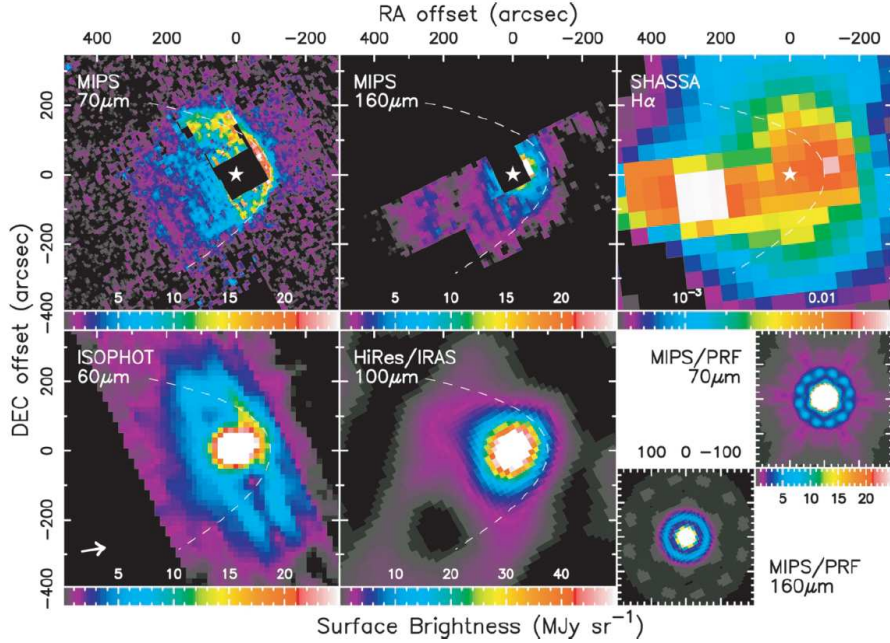
Figure 1.12.: First detection of a bow shock around an AGB star by Ueta et al. (2006). The image shows a overview of observations of R Hya and clearly reveal a bow shock around the star. A parabolic curve with the $y = x^2/3l$ is drawn in as a dashed white line to represent the outline of the bow shock.

(MIPS InfraRed Imaging of AGB Dust shells) revealed the first bow shock around an AGB star, R Hya (Ueta et al. 2006). R Hya is an AGB star with a space velocity of $50 \pm 1 \, \mathrm{km \, s^{-1}}$ and was mapped with the Multiband Imaging Photometer for Spitzer (MIPS) in 70 and $160 \, \mu\mathrm{m}$ (see Fig. 1.12). Ueta et al. (2006) found an arclike surface brightness distribution of about $400''$ diameter around the star. The shape of this bright region is parabolic with the apex at a distance of about $0.08 \, \mathrm{pc}$ ($100''$) from the star. The authors also found Hα emission along the parabolic apex, showing the presence of ionized gas and related the far-IR emission of the bow shock front to heated dust emission and to shock excited line emission of e.g. O[I] at 63 and $146 \, \mu\mathrm{m}$.

The last infrared space telescope that brought new insights in the AGB wind-ISM interaction scenario was the japanese AKARI telescope launched in 2006. AKARI's Far IR Surveyor (FIS) instrument works in four bands from $65 \, \mu m$ to $160 \, \mu m$ and Ueta et al. (2008) found a distinct bow shock around α Ori. After the previous detections of stellar wind bow shocks with infrared space

telescopes it was expectable to find these structures also with Herschel due to the three times higher resolution of PACS (full width half maximum (FWHM) at $70\,\mu m$ of $5.6''$) compared to Spitzer's MIPS ($18.6''$ at $70\,\mu m$) that detected the first bow shock around an AGB star. Ladjal et al. (2010) found then Herschel's first AGB bow shock around IRC $+10\,216$ (CW Leo) which is also part of the MESS GT KP. The authors concentrated on the structure seen on the $160\,\mu m$ image and detected a bow shock at a distance of $558''$.

In the same year Sahai & Chronopoulos (2010) found similar structures around the star using the Galaxy Evolution Explorer (GALEX) telescope that observes in the ultraviolet at $1528\,\text{Å}$ and $2271\,\text{Å}$. In addition, Geise et al. (2010) showed an overview of the mass loss history of several evolved stars. This initiated the present work about the AGB wind - ISM interaction. A small and incomplete overview of bow shock objects in the MESS catalogue, among them also TX Psc and X Her, is shown in Mayer et al. (2011b). A complete overview of all resolved objects in the MESS catalogue is the topic of the forthcoming paper by Cox et al. (2011).

1.5.3. Observational constraints

The last part of the introduction deals with the possibilities to observe a stellar wind bow shock. One method is to observe the emission of ionized hydrogen atoms in the bow shock layer. The neutral medium of the ISM, which mostly consists of neutral hydrogen, gets swept up by the stellar wind and collisionally excited. Shortly after, the electron recombines with the proton and a photon of the wavelength $6562.8\,\text{Å}$, called $H\alpha$ line, is emitted. This ionization takes place only in systems with a strong shock interface, like supernova remnants or bow shocks around neutron stars (Chatterjee & Cordes 2002). For AGB stars, $H\alpha$ emission was only detected around the prototype variable star Mira (o Ceti) (Meaburn et al. 2009) and the emission stems not from the bow shock but from a fast bipolar outflow of approximately $160\,\text{km\,s}^{-1}$. This velocity added to the high space velocity of $110\,\text{km\,s}^{-1}$ can result in this strong shock interface.

The high space velocity of Mira was also the subject of another observation. Martin et al. (2007) found with GALEX a bow shock around the star and an extended tail of about $2°$ in the sky which corresponds to $4\,\text{pc}$. Together with the previously discussed observations of CW Leo by Sahai & Chronopoulos (2010) these are so far the only observations of UV emission in the environments of AGB stars. Mira has been studied in many different wavelengths and no bow shock or tail has been observed. The bow shock and tail are clearly visible and very bright in the UV and this led to a discussion about the origin
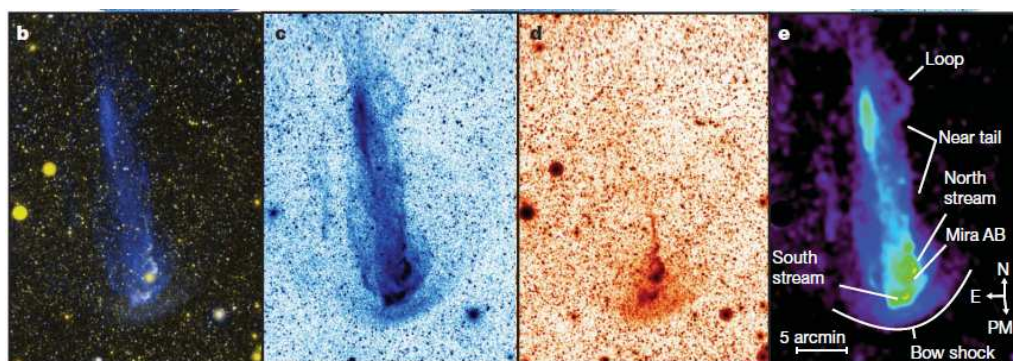
Figure 1.13.: Tail and bow shock around Mira (o Cet) in the UV by Martin et al. (2007). Mira is travelling with a space velocity of about $110 \, \mathrm{km \, s^{-1}}$ through the ISM and shows a strong bow shock and tail structure due to the ram pressure of the oncoming ISM and the shear flow that passes downstream from the bow shock apex. Images from left to right: energy scaled colour composite, histogram equalized far ultraviolet, the same for near ultraviolet and a description of the structures on the smoothed FUV image.

of the emission. Martin et al. (2007) brought up a physical picture where the high space motion of Mira produces a strong bow shock of the stellar wind with the ISM. The shock is non-radiative because the post shock gas has an isochronic cooling time of only 2000 years. The ultraviolet emissivity tracks the monotonic increase of ionization of the medium. The shear flow of the shocked gas from the apex of the bow shock cone passes the cool stellar wind and interacts shock wise with the bipolar outflow. This also explains the Hα emission observed by Meaburn et al. (2009).

The tail structure is most probably caused by H_2 emission. The H_2 molecules in the region of the cool wind get collisionally excited by hot electrons from the post shocked gas. This is also in accordance with the fact that it is not visible in other wavelength, since H_2 emission is only detectable in the ultraviolet.

Nevertheless, the best chance to observe a stellar bow shock is given in the far-IR. Although the first IR observations of stellar bow shocks took place more than two decades ago (van Buren & McCray 1988; Stencel et al. 1988) the reasons for their observability are poorly understood (Ueta 2009). It probably originates mainly from the thermal emission of the cold dust component in the density enhanced, shocked stellar wind-ISM interface. Draine (1981) describes the infra-red emission from dust in shocked gas. At moderate energies ($10 \, \mathrm{eV} \geq \mathrm{E} \leq 100 \, \mathrm{eV}$) electrons and ions collide with dust grains and

penetrate their outer layer and essentially all of the kinetic energy is dissipated and converted into thermal energy. When the impact energy of the particle is higher it penetrates the whole grain and only a small fraction of the kinetic energy is converted into heat. The IR emission of the heated up dust may account for a large fraction of the energy radiated from the grain when it cools down. Draine (1981) also gives an equation for the wavelength at which the emission peaks with relation to the shock wave speed v_{s}:

$$\lambda_{\mathrm{peak}} \approx 75\mu\mathrm{m} \left(\frac{n_{\mathrm{H}}^0}{\mathrm{cm}^{-3}}\right)^{-0.18} \left(\frac{v_{\mathrm{s}}}{100\,\mathrm{km\,s}^{-1}}\right)^{-0.3}, \qquad (1.52)$$

where n_{H}^0 is the density of the gas before the shock. The assumption, however, was made for strong shocks with a velocity of $v_{\mathrm{s}} \geq 200\,\mathrm{km\,s}^{-1}$. This can be provided by hot OB stars with winds as fast as $1000\,\mathrm{km\,s}^{-1}$ and also planetary nebulae. For AGB winds the shocks are weaker, the wind velocity is in general very small and the space motion of the star not comparable with a runaway OB star. Thus, the nature of the IR emission from the AGB wind - ISM interaction zone remains somewhat unclear. Another suggestion by Ueta (2009) is that low-excitation atomic lines such as [O I] at $63\,\mu\mathrm{m}$, [O I] $145\,\mu\mathrm{m}$ and [C II] $158\,\mu\mathrm{m}$ contribute to the brightening of the bow shock in the IR. The portion of the contribution is not clarified.

2. X Herculis and TX Piscium

Before going straight to the new observations obtained with Herschel it is help-
ful to get in touch with previous observations of the objects and collect data
to get the new observations that are presented later in the right context. Both
objects, X Her and TX Psc, are well studied and were targets of many previous
observations since they are among the brightest and nearest AGB stars of their
spectral class. In the first part of this chapter the most important observations
that are of interested for the stellar wind - ISM interaction are presented. This
includes mainly observations of the CSEs in different wavelengths but also the
bipolar outflows which are present in both objects. The second part of the
chapter deals with the motion of the stars since it plays the key role for the
interaction. The general way to calculate the space motion is presented and
the limitations of the introduced simplifications are discussed. The obtained
space motions are then compared with that of other AGB stars. The location
in the UV diagram helps to distinguish if the space motion is an exceptional
value or typical for an AGB star.

2.1. Previous observations and results

This chapter is based on the forthcoming publication of Jorissen et al. (2011) where previous observations and new results are discussed more briefly due to the shortage of space.

2.1.1. X Her

Stellar properties

X Her is classified as an M8III star. This categorizes it as an oxygen-rich giant. Typically for late type stars X Her shows small light variations in the order of $\Delta V \approx \pm 0.5\,\mathrm{mag}$ with a period of 95 days (General Catalogue of Variable Stars; GCVS). This gives it a SRb classification, a semi-regular late-type giant with poorly defined periodicity. In addition to that Hinkle et al. (2002) found a long secondary period of 658 d. Speckle interferometry and radial velocity searches failed to detect an accompanying star to X Her (Lu et al. 1987), thus no assumption of a binary system is made throughout this work.

The parallax of X Her was measured with $7.30 \pm 0.40\,\mathrm{mas}$ by the Hipparcos Satellite (van Leeuwen 2007) and corresponds to a distance of $137 \pm 8\,\mathrm{pc}$, making X Her one of the closest SRb stars. The Hipparcos data have very large errors and are not reliable when the parallax is smaller than $\approx 1.5\,\mathrm{mas}$. Since this is neither the case for X Her nor for TX Psc the values for the parallax and proper motions are adopted from the catalogue. For the proper motion this is $\mu_\alpha \cos\delta = -68.5 \pm 0.4\,\mathrm{mas\,yr^{-1}}$ and $\mu_\delta = 64.6 \pm 0.4\,\mathrm{mas\,yr^{-1}}$, right ascension and declination, respectively. The kinematic data are completed by the radial velocity of $-89.95\,\mathrm{km\,s^{-1}}$ (Famaey et al. 2005).

The temperature of X Her was determined with $3281 \pm 130\,\mathrm{K}$ by Dyck et al. (1998) who also defined the radius with $183 \pm 8\,R_\odot$. Together with the K-band magnitude of -1.42 (Kerschbaum & Hron 1994) and a red giant bolometric correction of 2.7 (Le Bertre et al. 2001) this results in a luminosity of $4800\,L_\odot$ and places X Her clearly on the AGB.

With a mass loss rate of $\dot{M} = 1.5 \times 10^{-7}\,M_\odot\,\mathrm{yr^{-1}}$ and a wind velocity $v_\mathrm{w} = 6.5\,\mathrm{km\,s^{-1}}$ (González Delgado et al. 2003) X Her represents typical values for a low mass loss rate AGB star.

Circumstellar properties and bipolar outflow

Besides the observations of the star itself, also the CSE is well studied. The dust composition was examined with the IRAS Low Resolution Spectrometer (LRS) and ISO's Short Wavelength Spectrometer by Kwok et al. (1997) who
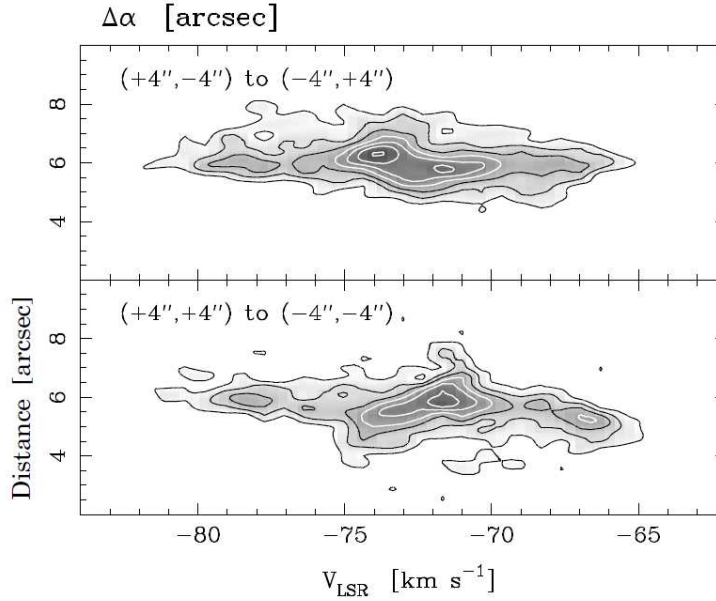
Figure 2.1.: SiO (v=0, J=1–0) maps of the environment of X Her from the VLA show evidence for a bipolar outflow in NE-SW direction. The upper panel is in NW-SE direction and the lower panel in NE-SW direction, perpendicular to the space motion of the star. Besides the bipolar outflow there is also slight evidence for a rotating disk in the lower panel.

classified X Her as E, showing amorphous silicate features at 10 and 18 μm. An unidentified feature at 13 μm was also detected (class SE6t) which is possibly related to crystalline alumina (Sloan et al. 2003).

In the 60 μm image of IRAS a large infra-red source with a diameter of 12.4′ was detected (Young et al. 1993). Its position, region IIIa, in the IRAS colour-colour diagram by van der Veen & Habing (1988) refers to a thick dust shell (see Fig. 2.4).

The morphology of the CSE was first studied by Kahane & Jura (1996) who observed the ^{12}CO(J=1–0), ^{12}CO(J=2–1) and ^{13}CO(J=2–1) transitions with the IRAM 30 m telescope. The CO profiles show a narrow central peak with wings on each side (south-west and north-east) corresponding to a systemic LSR velocity of 73.3 km s^{-1} and an expansion velocity of 2.5 km s^{-1}. The south-west wing is blue-shifted and peaks at 2.5″ while the north-east wing is red-shifted and peaks at the same distance. This is an indication of a bipolar outflow in NE-SW direction. The maxima of both wings do not coincide, thus

the bipolar flow is neither seen face-on nor edge-on due to the coexistence of the wings on the central spectrum (Kahane & Jura 1996). The direction of the outflow (PA = 45°) is almost perpendicular to the space motion (PA = 313°, see Section 2.2). The bipolar outflow was later confirmed by Nakashima (2005) in CO(1–0) observations with an extension up to 12.4″ and an hour-glass shape. The same author also found evidence for an elliptical disk with a size of 15.1″ x 12.6″ that is rotating or expanding. Castro-Carrizo et al. (2010) argued in favour for an expanding equatorial disk that lies perpendicular to the bipolar outflow. SiO thermal emission agrees with the CO observations (González Delgado et al. 2003). Fig. 2.1 shows SiO line data of X Her's environment obtained with the Very Large Array (VLA). The covered region is smaller than from the CO lines due to the fact that SiO is only excited close to the star in the innermost parts of the CSE. Nevertheless, the profiles are similar to the CO observations showing an hour-glass structure and a bipolar outflow at PA = 45°.

X Her's CSE was also observed in HI at 21 cm by Gardan et al. (2006) and Matthews et al. (2011). Former found with the Nançay Radio Telescope (NRT) a broad and centred feature and a narrow component that is red-shifted by 2–3 km s^{-1}. The line widths of the components however differ from the CO and SiO observations and do not seem to be related. The HI emission extends over 10′ and is clearly asymmetric with a concentration towards the northeast. The narrow component has a size of about 4′ and remains unresolved. Gardan et al. (2006) suggest a strong asymmetric large scale outflow, in contrast to the common picture of a spherical symmetric mass loss during the AGB phase (Huggins et al. 2009).

However, Matthews et al. (2011) point out that the previous observations by Gardan et al. (2006) were on the limit of the resolution of the NRT beam and therefore permit only a coarse characterization of the environment of X Her. The new HI observations by Matthews et al. (2011) were carried out with the VLA and the Green Bank Telescope (GBT) and offer a much higher spatial resolution. With these observations it is clear that the emission detected by Gardan et al. (2006) is not directly linked to the CSE of X Her and shows features of a large HI cloud in the north and north east of X Her. The star itself shows a peak emission at 71.7 km s^{-1} and an extended head-tail morphology with a length of 6′ or 0.24 pc. Fig. 2.2 shows the HI velocity field from this observation. The HI tail is at PA = 121° or 132° when measuring only the first 3′ of the tail. The CSE is approximately a factor two smaller than derived from the IRAS 60 μm image (Young et al. 1993). Matthews et al. (2011) relate the cometary morphology to the motion of the mass-losing star through the ISM, since similar morphologies were observed in o Ceti (Martin et al. 2007)
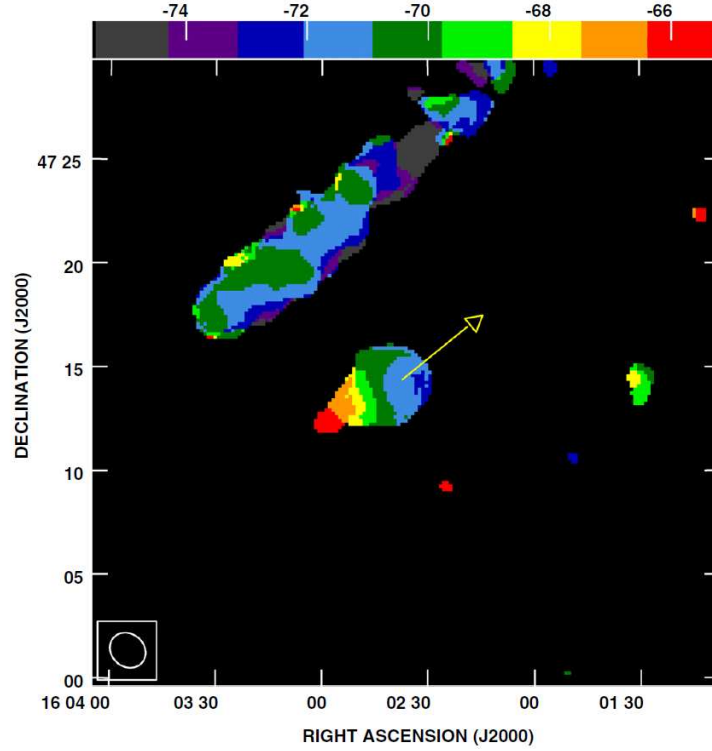
Figure 2.2.: HI velocity field of X Her and environment from VLA observations by Matthews et al. (2011). The direction of the space motion is indicated by an arrow. Clearly visible is the tail structure of X Her due to the high space velocity. The tail has a velocity gradient as indicated by the colours. The velocity is decreasing with increasing distance from the star. The structure in the north and north east is an HI high-velocity cloud.

and the position angle of the space motion is 309°, roughly opposite to the observed tail structure. In the velocity field (Fig. 2.2) the decrease of velocity with increasing distance from the star is also a hint that the material is swept back from the region of ISM interaction and subsequently gets decelerated. In an approach to estimate the age of X Her's tail the authors find $t_{\text{tail}} = 1.2 \times 10^5 \, \text{yr}$ with an error of 20 %. This exceeds the mass loss duration found by Young et al. (1993) by a factor of three.

2.1.2. TX Psc

Stellar properties

TX Psc is, like X Her, a well studied object since it is one of the brightest and nearest carbon stars. The spectral class of carbon stars is C. TX Psc shows a variability of 0.4 mag from peak to peak in the visible band and the GCVS classifies the star as Lb, a slow red irregular variable of late spectral type. Observations by Wasatonic (1995) and AAVSO measurements although show a period of 224 and 220 days, respectively. This pushes the classification towards SRa or SRb, i.e. a semi-regular late type giant, and the classification is even more stretched by CN and Ti observations of Barnbaum & Hinkle (1995) who found a large amplitude range of the radial velocity. These observations however were too patchy to allow precise conclusions. New observations made in 2009–2010 with the HERMES spectrograph of the Mercator telescope (Raskin et al. 2011) that spread over 450 days confirm the large radial velocity amplitude and found it to range from 8 to $15 \, \mathrm{km \, s^{-1}}$ (see Fig. 2.3). The velocity variation occurs in a frame that is substantially longer than the period of 224 days and it is therefore not believed to be caused by the pulsating atmosphere, but more to be an indication for a long secondary period, like observed for X Her or a binary system. However, since there is no further evidence of a companion, TX Psc is treated throughout this work as a single star.

The kinematic properties of TX Psc were studied with the Hipparcos satellite and are available from the catalogue by van Leeuwen (2007). The parallax of $3.63 \pm 0.39 \, \mathrm{mas}$ is converted to a distance of $275 \pm 30 \, \mathrm{pc}$. For the proper motion, values of $\mu_\alpha \cos \delta = -33.7 \pm 0.4 \, \mathrm{mas \, yr^{-1}}$ and $\mu_\delta = 24.5 \pm 0.3 \, \mathrm{mas \, yr^{-1}}$ in right ascensions and declination were obtained. The kinematic data are discussed in more detail in Section 2.2. The radial velocity was determined with $-11.0 \pm 0.9 \, \mathrm{km \, s^{-1}}$. The new observations discussed in the upper paragraph clearly show that this value is not appropriate (see also Fig. 2.3), thus an averaged value of $+13.0 \, \mathrm{km \, s^{-1}}$ is adopted from these observations.

The temperature for TX Psc was derived with $3046 \pm 77 \, \mathrm{K}$ together with a C/O ratio of 1.037 ± 0.021 and a luminosity of $L = 5200 \, L_\odot$ by Bergeat et al. (2001); Lambert et al. (1986). Quirrenbach et al. (1994) found an angular diameter of the star between 9.4 and 11.1 mas corresponding to 2.6 to $3.0 \, \mathrm{AU}$ or 560 to $660 \, R_\odot$ showing the nature of a giant star. Though, the evolutionary status on the AGB is unclear. The mass loss rate of $\dot{M} = 9.1 \times 10^{-8} \, M_\odot$ and the wind velocity $v_\mathrm{w} = 10.5 \, \mathrm{km \, s^{-1}}$ were derived from CO observations (Olofsson et al. 1993).
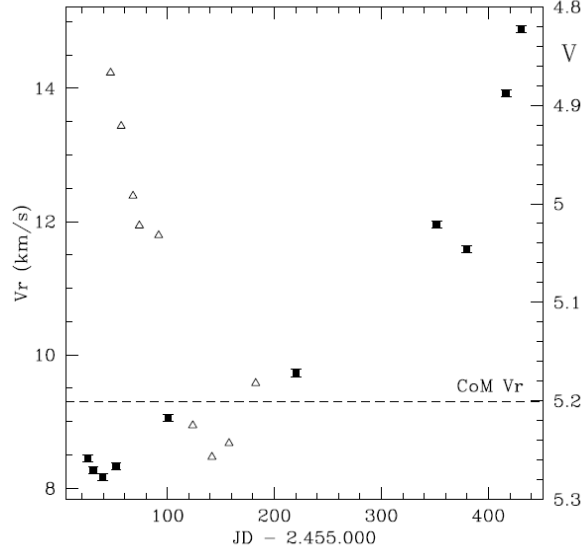
Figure 2.3.: Radial velocity variation of TX Psc observed with the HERMES
spectrograph (Jorissen et al. 2011). The amplitude ranges from 8
to $15\,\mathrm{km\,s^{-1}}$ with a period significantly larger than the observed
224 days (Wasatonic 1995).

Circumstellar properties and bipolar outflow

The circumstellar environment of TX Psc was also examined but not as exten-
sively as of X Her. Eriksson et al. (1986) found strong evidence for a circum-
stellar dust shell in high resolution spectra. Although the IRAS LRS spectra
classified the environment of TX Psc as S, showing no features (Kwok et al.
1997), even though the observations place TX Psc in region VIa of the IRAS
colour-colour diagram (van der Veen & Habing 1988), with the attribute of a
detached shell (see Fig. 2.4). Young et al. (1993) found indeed that the CSE
is extended as far as 3′, thus the classification of Kwok et al. (1997) remains
misunderstood. Wirsich (1991) calculated the dust temperatures at different
parts of the CSE based on UV and Far-IR fluxes. The author found a dust
temperature of $1155\,\mathrm{K}$ at a distance of 2.25 stellar radii decreasing towards
$410\,\mathrm{K}$ at 30 stellar radii.
The first larger investigation on the CSE was done by Heske et al. (1989).
The authors used the IRAM $30\,\mathrm{m}$ telescope to observe the CO(2–1) and (1–0)
transitions. The observations show two features, a narrow peak centred in the
(2–1) spectrum and a weaker one a bit offset where it could be assigned to
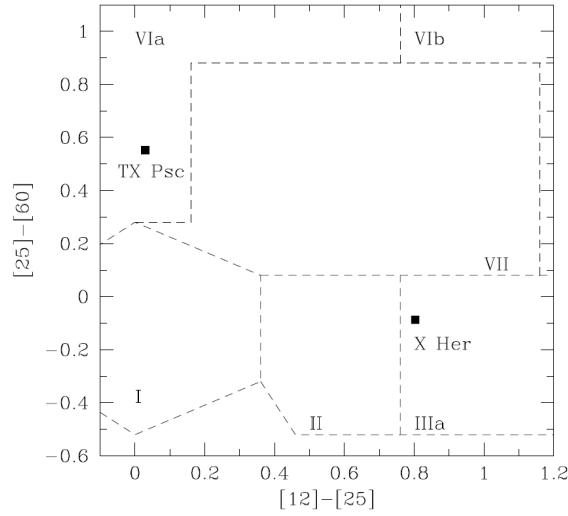a local density enhancement moving perpendicular to the line of sight. The

Figure 2.4.: Classification of the circumstellar environments of X Her and TX Psc in the IRAS colour-colour diagram by van der Veen & Habing (1988). X Her belongs to the region IIIa, indicating a thick dust shell; while TX Psc is of class VIa, typically surrounded by a detached dust shell.

second feature us the presence of asymmetric line profiles at three offset positions with the maximum emission red shifted by $4\,\mathrm{km\,s^{-1}}$. The red and blue shifted parts of the emission are separated by $10''$, oriented along the NE-SW, in direction of space motion. The authors allot the asymmetry to a bipolar outflow or to a clumpy wind.

The asymmetry was also detected in sub-milliarcsecond observations with lunar occultation observations by Richichi et al. (1995) and with help of the adaptive optics system Come-On+ by Cruzalebes et al. (1998). Former found a complex double peak profile with the extent of a few milliarcsec in the L band. Latter show asymmetric structures with a clump extended to the SW direction at a distance of $0.25''$ to the star. The direction is equal to the emission observed by Heske et al. (1989) and the direction of the space motion.

2.2. Determination of the space velocity

One of the most important parameters of the wind-ISM interaction is of course the velocity of the star with respect to the surrounding ISM. Baranov et al. (1971) showed that the stand-off distance is linearly correlated to the star's velocity:

$$R_0 = \sqrt{\frac{\dot{M} v_{\mathrm{w}}}{4\pi \rho_0 v_*^2}} \tag{2.1}$$

and the analytic shape of the bow shock is in turn correlated to the stand-off distance. However, the velocity relative to the ISM is not easy to obtain.

The simplification assumed in many papers is that the ISM flows with the same speed as the ISM does in the vicinity of the sun, the local standard of rest (LSR). This is obviously not correct when regarding the differential rotation of the galaxy and the decreasing ISM velocities with increasing distance to the galactic center. Also a turbulent ISM with unexpected flows can have a big impact on the relative velocity of the star. This however goes beyond the scope of this work and the calculation of the space velocity is carried out with respect to the LSR following Johnson & Soderblom (1987). This is justified by the relatively short distances to the stars which in turn means that the ISM flow is not very different from the ISM flow in the vicinity of the sun.

The calculation uses straightforward spherical trigonometry and the only necessary input is

- right ascension α and declination δ of the star

- $\pi \pm \sigma_\pi$, parallax in arcsec

- $\rho \pm \sigma_\rho$, radial velocity

- $\mu_\alpha \pm \sigma_{\mu_\alpha}$, proper motion of the star in right ascension

- $\mu_\delta \pm \sigma_{\mu_\delta}$, proper motion of the star in declination,

where σ gives the error of the values. The input can be summed up in two matrices

$$T = \begin{bmatrix} -0.06699 & -0.87276 & -0.48354 \\ +0.49273 & -0.45035 & +0.74458 \\ -0.86760 & -0.18837 & +0.46020 \end{bmatrix} \tag{2.2}$$

and

$$A = \begin{bmatrix} +\cos\alpha\cos\delta & -\sin\alpha & -\cos\alpha\sin\delta \\ +\sin\alpha\cos\delta & +\cos\alpha & -\sin\alpha\sin\delta \\ +\sin\delta & 0 & +\cos\delta \end{bmatrix} . \tag{2.3}$$

49

The product of this two matrices is $B = T \cdot A$ which is needed to obtain the galactic space velocity vector

$$\begin{bmatrix} U \\ V \\ W \end{bmatrix} = B \cdot C, \tag{2.4}$$

where C is

$$C = \begin{bmatrix} \rho \\ k\mu_\alpha/\pi \\ k\mu_\delta/\pi \end{bmatrix}. \tag{2.5}$$

The constant $k = 4.74057$ is the equivalent in $\mathrm{km\,s^{-1}}$ of the movement of one astronomical unit (AU) in one tropical year.

The gained $[U, V, W]$ vector is the motion of the star with respect to sun. To get rid of the heliocentric motion, the proper motion of the sun (Schönrich et al. 2010)

$$\begin{bmatrix} U \\ V \\ W \end{bmatrix}_\odot = \begin{bmatrix} 11.10 \\ 12.24 \\ 7.25 \end{bmatrix} \mathrm{km\,s^{-1}} \tag{2.6}$$

has to be added to the galactic $[U, V, W]$ vector. The length of the vector is the wanted galactic space motion with respect to the LSR

$$v_{\mathrm{LSR}} = \sqrt{U^2 + V^2 + W^2}. \tag{2.7}$$

Now it is also possible to correct the input values from the solar motion by inverting the B matrix and multiply it with the galactic $[U, V, W]$ vector

$$C' = B^{-1} \cdot \begin{bmatrix} U \\ V \\ W \end{bmatrix}. \tag{2.8}$$

From C' the solar motion corrected radial velocity and proper motions in right ascension and declination can be extracted.

With these values it is also possible to derive the position angle Φ of the space motion and the inclination i of the space motion towards the plane of the sky

$$\Phi = \arctan(\mu_{\delta,\mathrm{LSR}}/\mu_{\alpha,\mathrm{LSR}}) \tag{2.9}$$

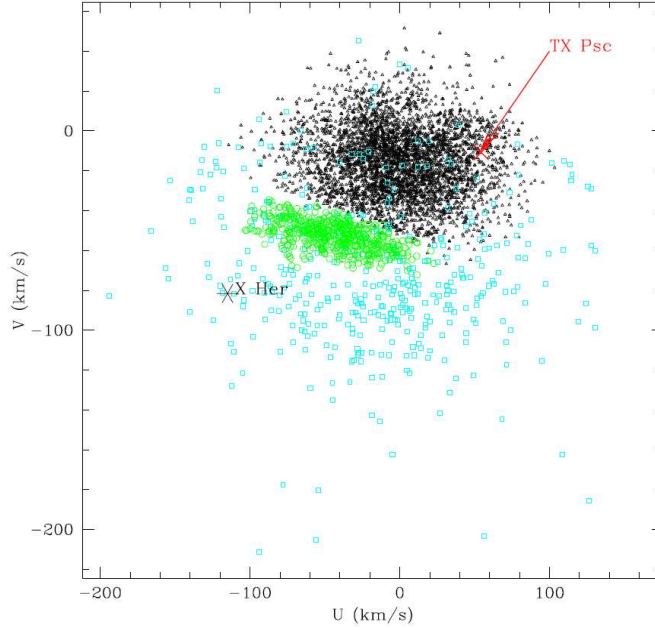$$i = \arccos(R_{\mathrm{v,LSR}}/v_{\mathrm{LSR}}), \tag{2.10}$$

Figure 2.5.: Location of TX Psc and X Her in the UV diagram of Famaey et al. (2005), adapted by Jorissen et al. (2011). X Her falls in the region of high velocity stars (blue squares) whereas TX Psc is in the region of smooth background stars (black dots). The green circles stand for Hercules stream stars, that have an outward radial velocity that lacks behind the galactic rotation.

where negative inclination values mean that the motion is towards the observer. For the errors of the heliocentric galactic space motion Johnson & Soderblom (1987) give

$$\begin{bmatrix} \sigma_U^2 \\ \sigma_V^2 \\ \sigma_W^2 \end{bmatrix} = D \begin{bmatrix} \sigma_\rho \\ (k/\pi)^2[\sigma_{\mu_\alpha} + (\mu_\alpha\sigma_\pi/\pi)]^2 \\ (k/\pi)^2[\sigma_{\mu_\delta} + (\mu_\delta\sigma_\pi/\pi)]^2 \end{bmatrix} . \tag{2.11}$$

The computation of the space velocity of TX Psc and X Her works straightforward. The input and output values are listed in Table 2.1. The proper motion values are all taken from the revised Hipparcos data (van Leeuwen 2007), the radial velocity for X Her was derived by Famaey et al. (2005) and the radial velocity for TX Psc was derived from new observations with the HERMES spectrograph of the Mercator telescope (Jorissen et al. 2011). Both R_v data lack an error bar, which is the reason for the missing error in the space velocity. The space velocities obtained for TX Psc and X Her, 66.9 and 89.9 km s^{-1},

Table 2.1.: Input values and results for the determination of the space velocity.

Input	α	δ	π	$\mu_\alpha\delta$	μ_δ	R_v
	[°]	[°]	[mas]	[mas]	[mas]	[km s^{-1}]
X Her	240.66347	+47.24020	7.30 ±0.40	-68.5 ±0.4	64.6 ±0.4	-88.95
TX Psc	356.59807	+03.48687	3.63 ±0.39	-33.7 ±0.4	-24.5 ±0.3	13.0
Results	i	Φ	v_{LSR}	$\mu_{\alpha,\text{LSR}}\delta$	$\mu_{\delta,\text{LSR}}$	$R_{v,\text{LSR}}$
	[°]	[°]	[km s^{-1}]	[mas]	[mas]	[km s^{-1}]
X Her	-55.4	309.0	89.9	-57.3	55.1	-73.6
TX Psc	13.6	242.6	66.9	-46.4	-19.0	13.4

respectively, are far above the average velocity of an AGB star (30 km s^{-1}; Feast & Whitelock (2000)). Fig. 2.5 by Famaey et al. (2005) shows the positions of the two objects in the UV diagram. X Her is clearly in the region of high velocity stars, indicated as blue circles in the figure. Famaey et al. (2005) stated that high velocity stars are probably mostly halo or thick disk stars, with a galactic height between 665 pc and 1000 pc. X Her however lies with 121 pc well below the halo or the thick disk. TX Psc however falls in the region of smooth background stars in the diagram due to its small radial velocity.

3. Observations

The topic of this chapter are the observations of TX Psc and X Her with the Herschel Space Telescope and the obtained results. The first part gives a short introduction how Herschel's PACS instrument moves over the region in the sky where the object lies and how the image is finally obtained. Following the important aspects of the image reduction in the Herschel Interactive Processing Environment (HIPE) and also in the Scanamorphos task that is working outside HIPE are discussed. This is done step by step from the raw to the final image.

The second part of the chapter deals with the analysis of the processed images. These reveal remarkable structures in both PACS bands, at 70 and $160\,\mu$m that are somewhat different to the expected morphology that was discussed in Section 1.4.2 and 1.5.1. Nevertheless, TX Psc and X Her both show a great variety of fundamental indications of wind - ISM interaction whereof some are obvious and others need more discussion. In the final part of this section a simple estimation of the dust temperature in the shocked region is made based on the black body emissivity.

3.1. Data retrieval and reduction

The images of X Her and TX Psc on which the following description of stellar wind - ISM interaction is based were obtained with PACS on board Herschel. The satellite and its instrumentation are discussed in Section 1.1 and the GT KP which is responsible for the observations, in Section 1.2.

The observations of X Her and TX Psc took place on December 20th and 21st 2009, respectively, both on the observation day 221. Both objects were observed with a scan map technique simultaneously in PACS' blue band at $70\,\mu$m and in the red band at $160\,\mu$m. This technique is the most frequently used mode for Herschel observations to map large regions of the sky and a full description is found in Poglitsch et al. (2010) on which also this section is based. In the scan map mode the satellite is slewed along parallel lines over the sky with a constant speed of $20''$ per second, where the bolometer performance is best. These parallel lines are called scan legs and a visualization of this technique can be seen in Fig. 3.1. The mapping is performed several times along the same tracks before the direction of the scan is switched by $90°$ to perform the same procedure perpendicular to the previous scan. This method guarantees the best sky coverage when combining both scan directions at the end of the data reduction process. The result of the scan map mode are several thousand single frames saved under two observation IDs (ObsID). For TX Psc they are 1342188344 and 1342188345, and for X Her 1342188322 and 1342188323. The advantages of the scan map technique are a better characterisation of the source vicinity and large scale structures in the background, a more homogeneous coverage in the final map, a higher redundancy with respect to the impact of noisy and dead pixels and a better point source sensitivity compared to a chop-nod observation (Poglitsch et al. 2010).

The raw data of both scan maps are stored as a so-called Level 0 product and can be retrieved from the Herschel Science Archive[1] (HSA). It contains also the full resolution instrument status information and the calibration data that is needed for the data analysis.

3.1.1. Data reduction with HIPE

From this point on the data reduction with the Herschel Interactive Processing Environment (HIPE) starts. HIPE is a Python based pipeline with a fully interactive user interface that includes a huge selection of implemented tasks like e.g. aperture photometry, intensity profile and source extracting tools,

---

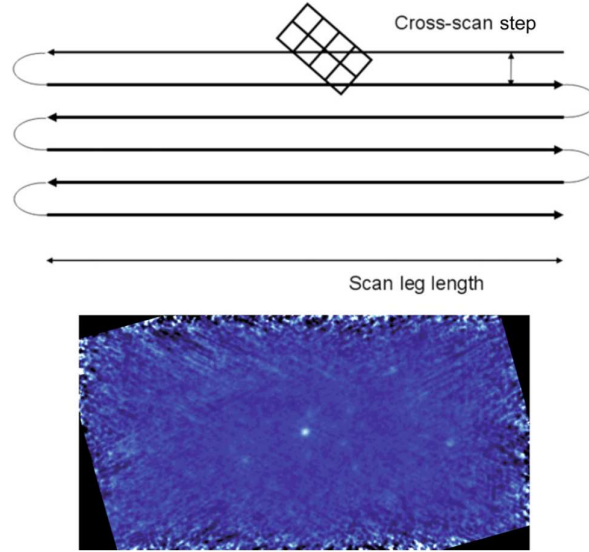[1] http://herschel.esac.esa.int/Science_Archive.shtml

Figure 3.1.: Schematic view of a PACS photometer scan map by Poglitsch et al. (2010). The upper panel shows how the spacecraft is slewed along parallel tracks called scan legs. At the end of each track the satellite turns left or right and scans the sky in the opposite direction as before. The lower panel shows the combined maps for HD 159330.

to name a few. A description of the implemented functions as well as handbooks for the data reduction with all Herschel instruments can be found on the Herschel Data Processing homepage[2]. Since the standard procedure that is described in the PACS handbook does not produce the best results yet alternative data reduction steps are outlined in the following.

The basis for the data reduction are the Level 0 data that were produced by the satellite and are available for download from the HSA. The files have to be extracted in a store directory that was created at the installation process of HIPE. All observation files of Level 0 contain a calibration tree which has to be loaded in order to apply the basic reduction steps towards Level 0.5 data. The reduction of the Level 0 data starts as follows. First of all, the calibration blocks are identified. Every observation starts with a 30 s long calibration block for the photometer where the chopper moves between two PACS internal calibration sources. This block has to be marked and removed. Since the automatic detection does not work perfectly about 120 frames of every Ob-

---

[2]http://herschel.esac.esa.int/Data_Processing.shtml

sID have to be removed manually. Next, the damaged and saturated pixels are masked and the crosstalk between the mosaic pixels is identified. The crosstalk occurs when heavily saturated parts of one pixel are reflected to another. In addition also glitches that always appear in electronic devices are masked. Unfortunately, the deglitching task creates problems because it also masks bright regions (Groenewegen et al. 2011). The generation of the Level 0.5 data is independent from the instrument and applied to all data.

From Level 0.5 on the reduction depends on the instrument that was used. For the PACS instrument and the scan map mode several additional corrections have to be applied. The responsiveness calibration of the array is done by subtraction of the flatfield image from the frames but also the drift of the telescope is corrected and the flux calibrated. In addition, the readout signal is converted to Volts, the universal coordinated time is derived from the on-board time and the centre of field coordinates are calculated for every frame and right ascension and declination are added. The reduction steps until Level 1 work completely automatically following a script by Marc Sauvage which lists the commands for each reduction task defined in the user handbook.

Level 1 marks the end of the uniform and automatic data reduction. From here on the reduction requires significant human interaction to produce the Level 2 data, that are used for the scientific work. This however depends on the observed source. In general, two reduction options are foreseen to obtain Level 2 data, although none of them was used for this work due to several problems in the final maps and the release of the Scanamorphos processing tool which returned better results for these special objects.

Nevertheless, to complete the overview of HIPE the two initial mapping methods are discussed briefly. One is the *Photproject* task that works with a high pass filter to remove the 1/f noise. The task uses a median filter which subtracts a median (masked pixels are suppressed) from each frame. The filter box size can be adjusted by the user for optimal results. For our kind of objects best results were obtained with a box size of 150–250. The final map making process is a projection of the right ascension and declination values that each frame obtained in Level 1 using the resolution of the detector ($3.2''$ per pixel at $70\,\mu$m and $6.4''$ per pixel at $160\,\mu$m). However, this method is optimised for point sources and causes a noisy and striped background. It is therefore less suitable to examine the extended and faint surroundings of stars. The stripes stem from the low frequency noise, that is discussed in detail below. Furthermore the extended emission suffers a lot from the high pass filter. A map of TX Psc created with the Photproject task can be seen in Fig. 3.2. The second implemented mapping algorithm for PACS is the Microwave Aniso-
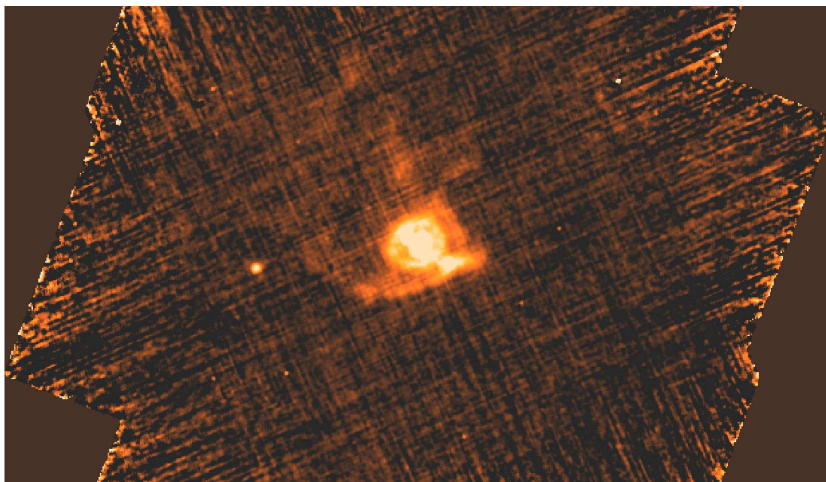
Figure 3.2.: PACS $70\,\mu$m image of TX Psc mapped with the Photproject task using high pass filtering with a box size of 200. The image is over-sampled by a factor of 3.2 to obtain a pixel size of $1''$. The background with this method remains noisy and the extended emission of the circumstellar environment is not well detected.

tropy Dataset mapper (MADmap) that, as the name suggests, was originally developed for observations of the cosmic microwave background. The advantage of this algorithm is that it is made for low spatial frequencies like the circumstellar environment. MADmap assumes that the noise is a Gaussian but knowledge is needed about the noise covariance of the low frequency noise (Poglitsch et al. 2010; Roussel 2011). Low frequency noise overlaps with the emission of the real source and is therefore difficult to distinguish. The origins of this noise are the temperature fluctuations of the cryogenic cooling bath and the non-thermal readout. The empirical noise model of each bolometer channel of the PACS instrument is implemented in the mapper. The maps produced by this algorithm have indeed a much smoother background and the extended structures are better visible than with the Photproject task. However, it has problems with bright regions and produces cross shaped shadows spreading over the image. Thus, it is not well suitable for observations containing both, faint and bright structures.

3.1.2. Advanced data reduction with Scanamorphos

In autumn 2010 a new method of image processing with Herschel data, named Scanamorphos, was released by Helene Roussel. An accompanying description,

on which also this paragraph is based, can be found in Roussel (2011). The big advantage of Scanamorphos is that it is build for scan map mode observations. It takes into account that the signal of each bolometer is modulated by a drift. Each position on the sky is sampled by several bolometers and the drift can be extracted by the redundancy of the observations. The result is a much smoother background that preserves the low spatial frequency of the extended emission undisturbed by artefacts of the bright point source. Scanamorphos is an interactive IDL language based program that works outside HIPE but requires Level 1 data for mapping. Thus, the data reduction takes place in HIPE to produce the Level 1 data and subsequent in Scanamorphos to pick the Level 1 data and continue processing. In the following the important aspects of the algorithm and the procedure to gain the final image are discussed.

The handling of the program is self explaining. The actual version of Scanamorphos at the time this is written is version 10. With the package comes also a *how-to guide* with all necessary steps and the commands that have to be entered. Before starting with Scanamorphos another HIPE script that is included in the Scanamorphos package has to be executed which converts the voltage of each bolometer to an in-beam flux density. This flux density represents the emission of a perfectly dark sky. With this conversion one can now open IDL and run the Scanamorphos tasks. Several input options are available for the user which are self-explanatory.

After the input the automatic data reduction starts with the computation of the map coordinates, space and time grids and the scan speed. In addition, the high frequency noise is computed and first pass glitches are masked as well as brightness drift with long time-scales. Though, what makes the algorithm superior to MADmap and PhotProject is that it identifies precisely the low frequency noise by the redundancy of the scan maps.

The main principle of the drift correction of redundant data is that the signal from a certain position on the sky should be the same at any time and the drift that occurs is the sum of the low frequency noise that effects the detector and the high frequency noise. To compare the signal, the region of the observed sky is cut into pieces of the size of the full width half maximum (FWHM) of the point spread function. For the $70\,\mu$m band the region has a size of $5.2''$ and at $160\,\mu$m of $12''$.

The first correction in this context is the average drift over the time series while thermal drifts are assumed to be uniform over the whole array (Roussel 2011). The brightness difference of a pair of bolometers that cover the same region on the sky is equal to the difference of the drifts at the two sampled times. The result of each pixel is stored in a matrix and subtracted from the signal series of each bolometer. This task is iterated until the drift ampli-
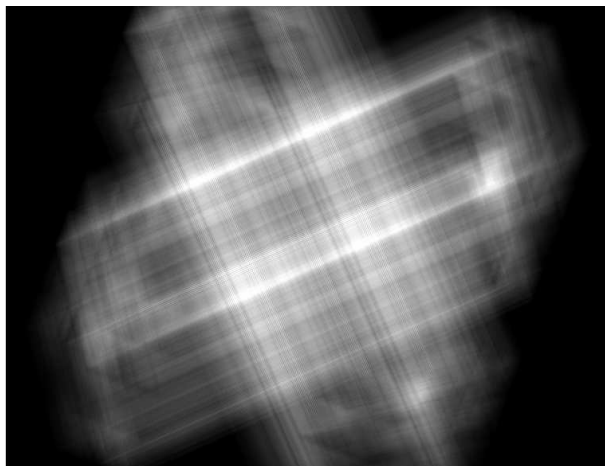
Figure 3.3.: PACS 70 μm low frequency noise map of the observation of TX Psc
obtained with the Scanamorphos algorithm. The noise map is the
sum of the average drift of all bolometer and the individual drift
of each bolometer.

tude has become smaller than the randomly appearing white noise level of the
bolometer.

The second low frequency noise correction is the individual drift of a bolome-
ter. The average drift of all bolometers is equal zero at this stage what allows
to measure the individual drift of each bolometer by comparing the signal of
each bolometer with the average signal of all bolometers at any position on the
sky. The procedure is the same as in the average drift correction and needs
several iterations. At the end the matrices are summed and subtracted from
the signal. Fig. 3.3 shows the map of the low frequency noise for the observa-
tion of TX Psc.

For the final step of the reduction process a projection produces a corrected
sky map, a weight map which include the inverse square of the white noise,
an error map for the high-frequency noise and a low-frequency map. These
are stored in one data cube. The sky map can then be extracted from this
cube with a HIPE task. The final sky maps for TX Psc and X Her in 70
and 160 μm are shown in Fig. 3.5, 3.6, 3.7 and 3.8. To display the images in
a certain colour and set the cuts for the lower and upper boundaries of the
colour distribution the fits files have been edited in the *SAOImage DS9* (DS9)
data visualization application. The color scheme used if not different stated is
"heat" for all images.

A full description and discussion of the noticeable structures as well as a de-
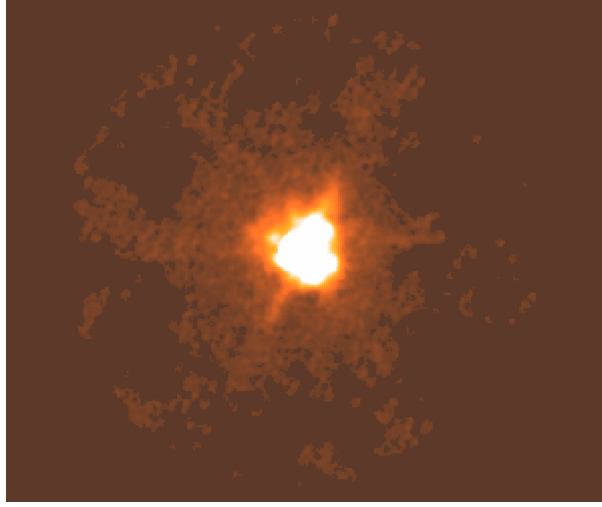tailed look into certain regions follow in Section 3.2.

Figure 3.4.: Point spread function of the PACS $70\,\mu$m image of X Her by Roland Ottensamer. Every data point of an image gets spread in the manner of the shown figure.

3.1.3. Deconvolution of Scanamorphos images

The signal of a point source is modified due to optical distortion and spreads in general over a larger area. This distortion affects every signal source of an image and is described by the point spread function (PSF). The PSF of X Her is shown in Fig. 3.4. The process to reconstruct the initial point source from the PSF is called deconvolution. To achieve this the PSF of the optical system is calculated and the image is divided by the PSF. This work was done by Roland Ottensamer and a overview of deconvolution of PACS data can be found in Ottensamer et al. (2011). In Section 3.2 and 4.2 these images are presented where they help to distinguish instabilities in the bow shock front.

Figure 3.5.: PACS $70\,\mu$m image of TX Psc created with the Scanamorphos algorithm. The image was oversampled by a factor of 3.2 with a resulting pixel size of $1''$ and the cuts were set to a black point of -0.008 and a white point of $0.0055\,\mathrm{Jy\,pix^{-1}}$ for best visibility. The triangular shaped central star is strongly affected by the PSF.

61

Figure 3.6.: PACS 160 μm image of TX Psc created with the Scanamorphos algorithm. The image was oversampled by a factor of 3.2 with a resulting pixel size of 2″. The cuts were set to a black point of -0.002 and a white point of 0.007 Jy pix^{-1} for best visibility.
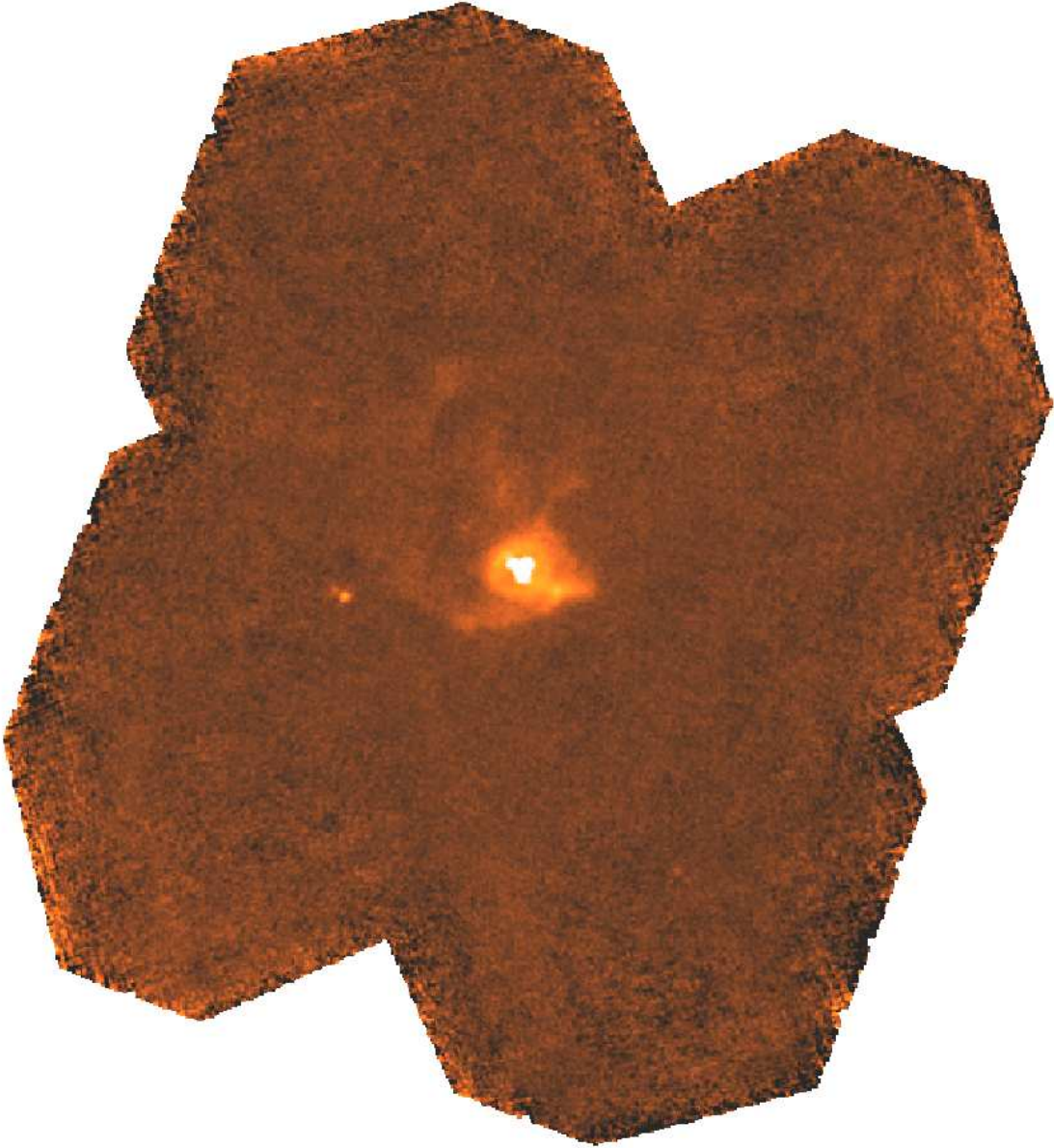
62

Figure 3.7.: PACS 70 μm image of X Her created with the Scanamorphos algorithm. The image was oversampled by a factor of 3.2 with a resulting pixel size of 1″. The cuts were set to a black point of -0.001 and a white point of 0.0025 Jy pix^{-1} for best visibility.
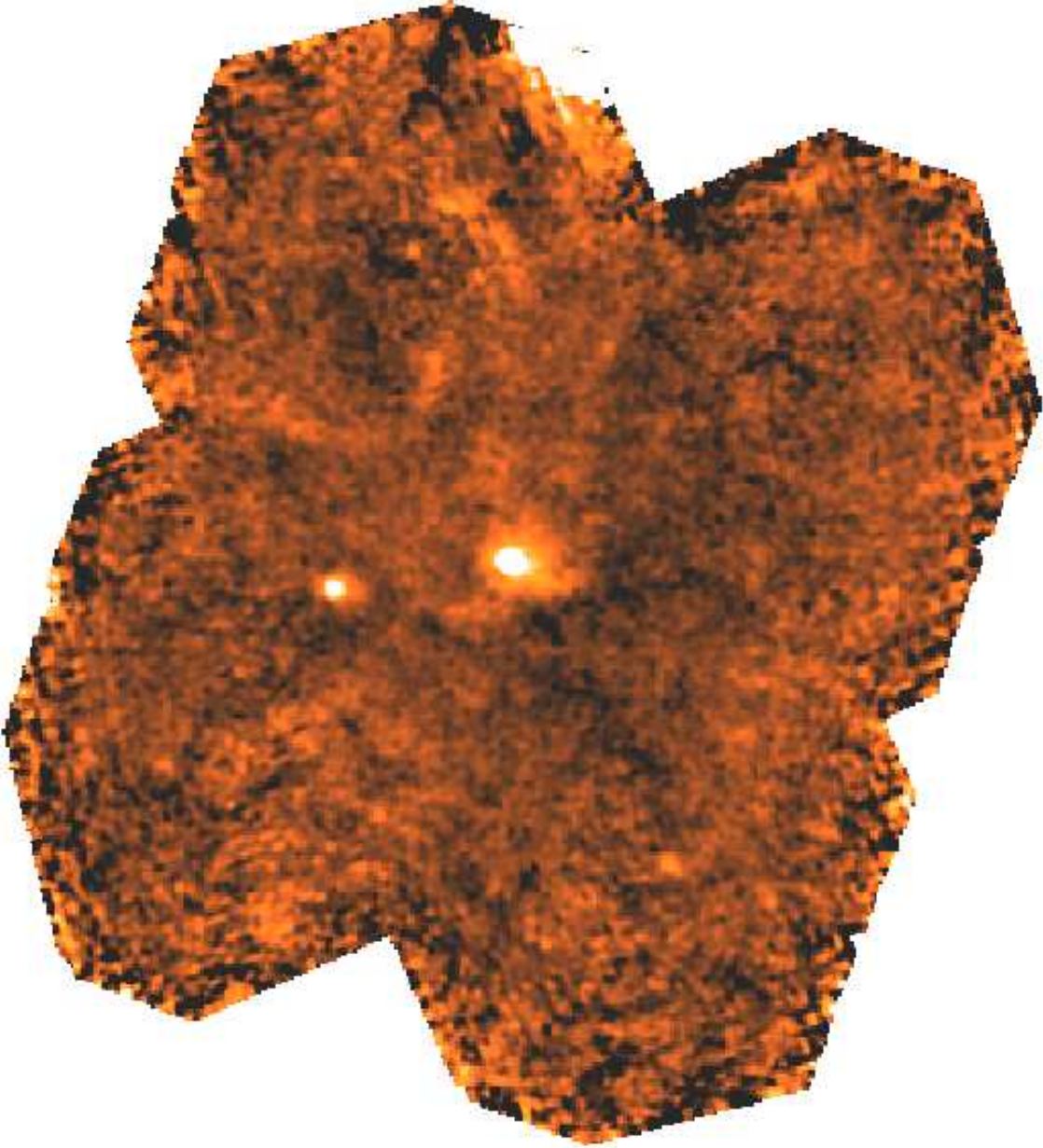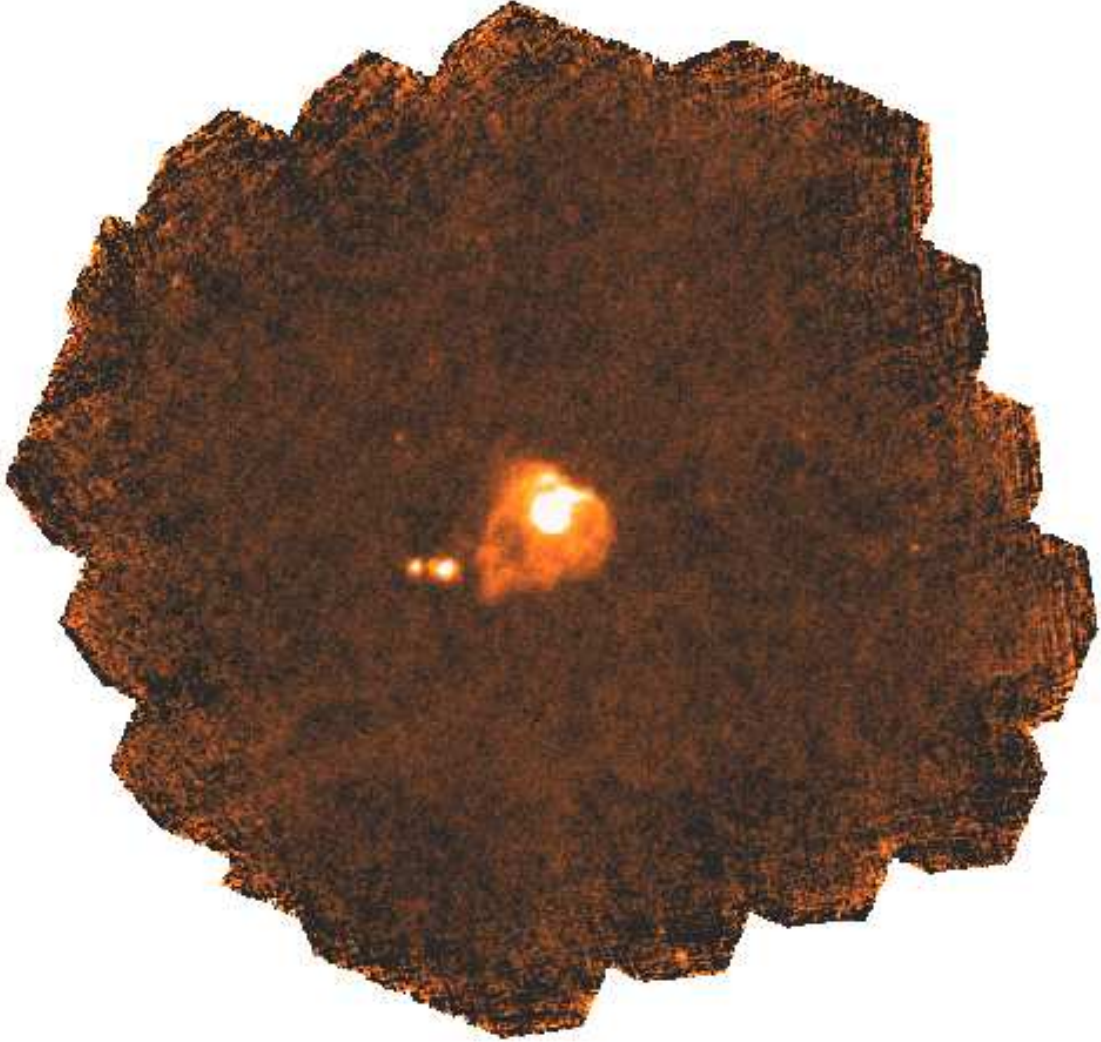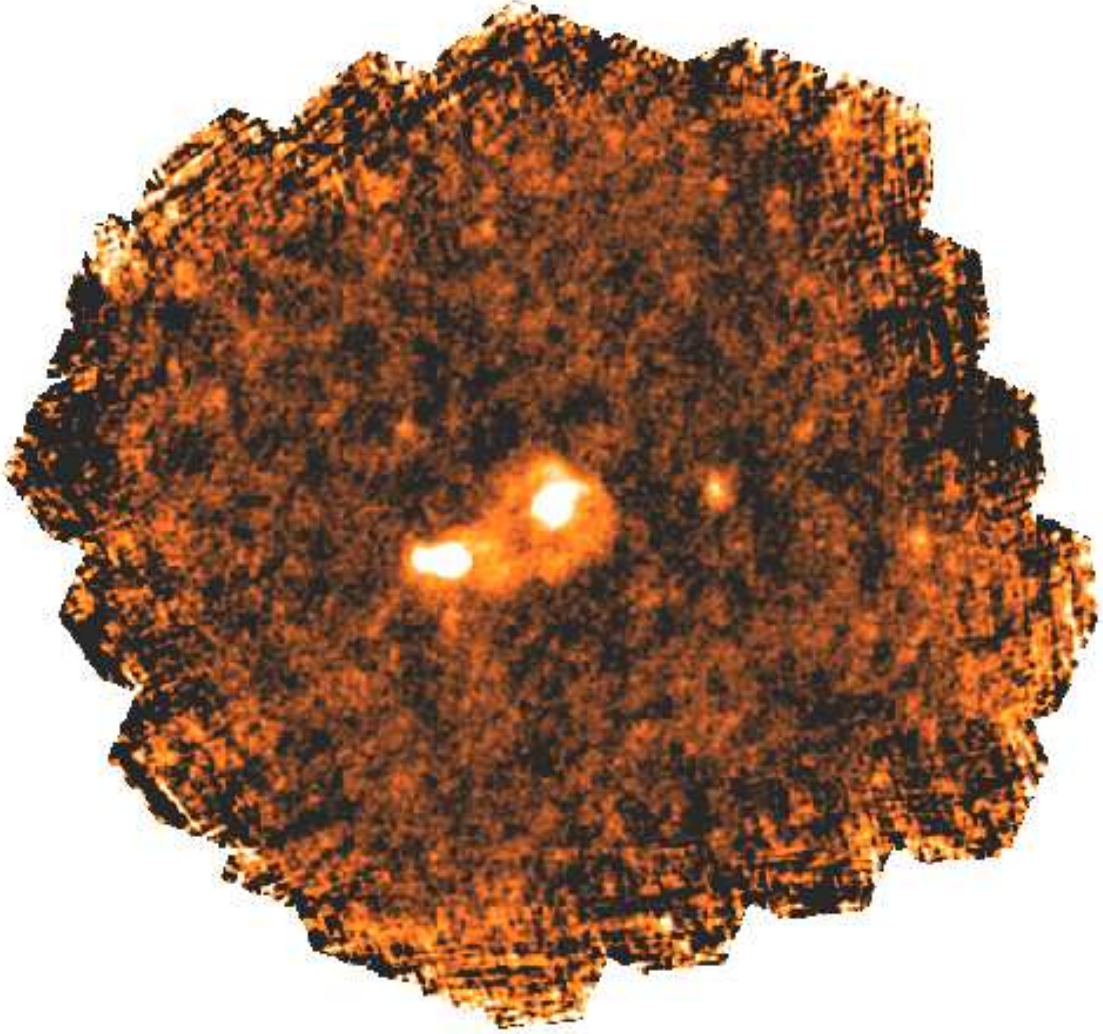
Figure 3.8.: PACS $160\,\mu$m image of X Her created with the Scanamorphos algorithm. The image was oversampled by a factor of 3.2 with a resulting pixel size of $2''$. The cuts were set to a black point of -0.002 and a white point of $0.0055\,\mathrm{Jy\,pix^{-1}}$ for best visibility.

3.2. Observational results

The observational results that are presented in the following are based on Jorissen et al. (2011) which will be published soon.

3.2.1. X Her

A closer look at the object is presented in Fig. 3.9. In the images the direction of the space motion with respect to the LSR, based on the calculations shown in Section 2.2, is indicated by an arrow. The length of the arrow shows the projected distance that the star moves in a given time. The scaling bar at the bottom left is based on the Hipparcos parallax.

Since the blue band image at $70\,\mu$m offers the better resolution compared to the red band image at $160\,\mu$m, the upcoming examination is based on this image, if not explicitly stated else.

The first feature of X Her that catches the eye is the heart-shaped CSE around the star. It is a bright structure, well above the emission of the background which is on the Scanamorphos images in the order of $1.5 \times 10^{-4}\,\mathrm{Jy\,pix^{-1}}$ at $70\,\mu$m and $3 \times 10^{-4}\,\mathrm{Jy\,pix^{-1}}$ at $160\,\mu$m. The two bright knots in the south-east of the CSE are a pair of galaxies, UGC 10156a and b. The faint structure in the west of X Her, visible only in the red band image, is another galaxy, MGC+08-29-036. Both are therefore not connected in any sense to the filamentary structures around the star. The heart-shaped pattern is a wonderful sign of the stellar wind-ISM interaction as it is precisely aligned with the space motion of the star. Moreover, the structure is brighter in the upstream region where it hits the oncoming ISM. Density enhancements in form of knots are visible north of the star, as well as a faint arm leading downstream. Different to previously observed bow shock structures with IRAS, Spitzer and AKARI the stellar wind of X Her shows a bump at the position where the apex of the bow shock is expected. This was predicted in hydrodynamic simulations of Wareing et al. (2007a) and Comeron & Kaper (1998) and is discussed more detailed in Section 4.2.

In the SE a tail structure can be seen. The position opposite to the space motion direction weakens every other interpretation than a connection to the ISM interaction.

The images also show density enhancements at the bow shock front in the north east as well as in the bump region in direction of the space motion. They are well visible in the deconvolved $70\,\mu$m image (Fig. 3.9, lower panel).

To analyse the observed structures, intensity plots are calculated in all directions on the deconvolved image. To gain a smooth curve that is not affected

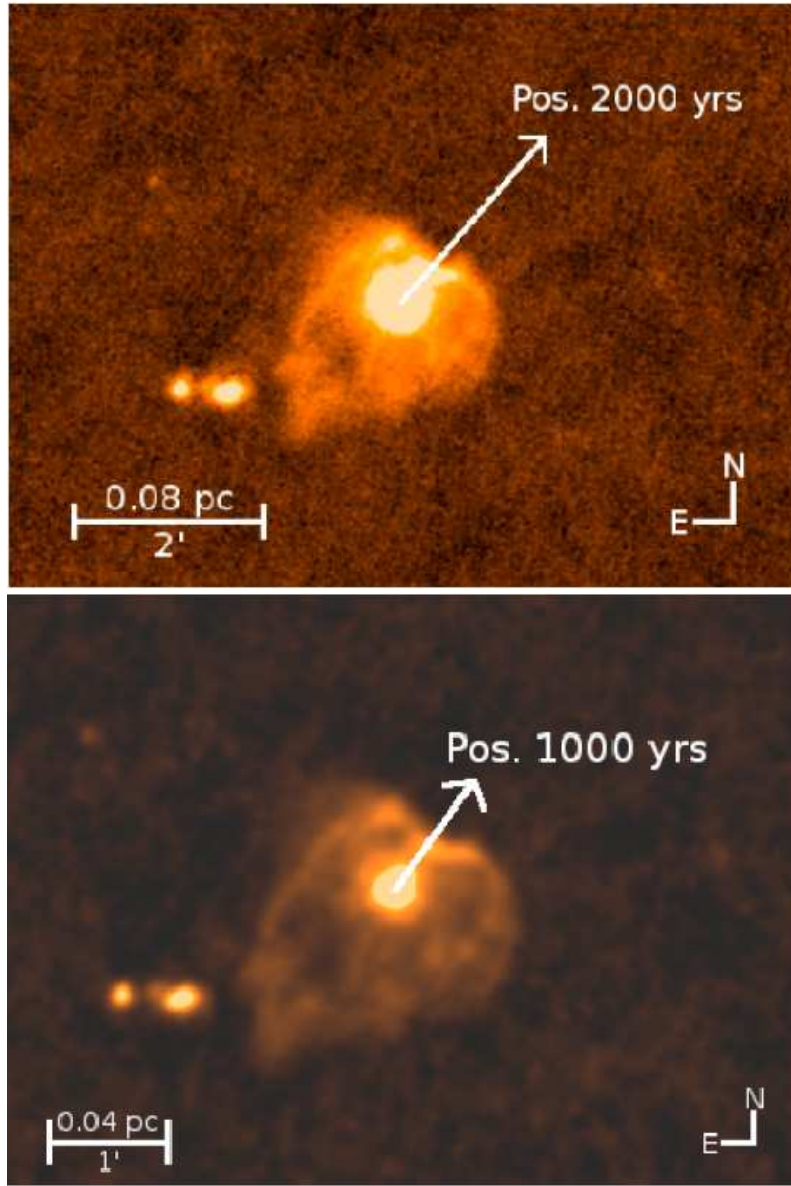Figure 3.9.: PACS images of X Her in the blue channel at $70\,\mu$m (Jorissen et al. 2011).   The upper image is created with Scanamorphos, in the lower image also deconvolution was applied.   In both images the arrows indicate the direction of the space motion and the position in 2000 yr (upper image) and 1000 yr (lower image).   The two bright sources in the south east of X Her are a pair of galaxies, UGC 10156a and b.

66

by single pixel variations the flux was integrated over a certain angle around the star. This angle defines a wedge wherein the fluxes of the pixels that lie on an arch with the same radius of the star are summed up. This flux is then divided by the number of pixels on the arch to get an average flux value per distance.

For X Her four regions are examined to cover the interesting features, two along the space motion and the other two perpendicular to it. The plots can be seen in Fig. 3.10. In addition the kinematic ages of the structures are derived with the knowledge that the stellar wind of X Her is expelled with a velocity $v_w = 6.5\,\mathrm{km\,s^{-1}}$ (González Delgado et al. 2003). The kinematic age is then the time that the wind needs to cover the observed distance. This is of course a very crude estimation because it does not take the interaction of the wind with the ISM into account that slows down the wind and piles it up, as discussed in Section 1.4. For this reason the derived kinematic ages only give the absolute minimum of the structure's age and have to be regarded as an estimation of the order of magnitude.

The upper left panel of Fig. 3.10 shows the region from position angle (PA) 145–155°, starting from north over east, thus, covering the tail of X Her in the SE. The tail is visible up to a distance of $120''$ or $0.08\,\mathrm{pc}$ from the star what corresponds to a free streaming time of the wind of 12000 ± 700 years. The plot shows also that there is a cavity next to the star between $20''$ and $60''$ (0.013–$0.04\,\mathrm{pc}$) that shows only weak emission. The tail becomes then noticeable as a plateau reaching from approximately $60''$–$120''$ (0.04–$0.08\,\mathrm{pc}$). The upper right panel of Fig. 3.10 covers the sharp density enhanced region in direction of the space motion in the NW from PA 296–320°. It is represented by the peak at a distance of $28''$ ($0.019\,\mathrm{pc}$) from the star. The peak is narrow and the intensity declines steeply which indicates that it is a sharp edge that separates the stellar wind from the ISM. The minimum kinematic age for this region is 2800 ± 200 years. Since this is the main interaction region this value has to be regarded with special caution.

In both lower panels the directions perpendicular to the space motion are presented. The lower left panel covers the NE region and reveals that the arm is reaching out as far as $40''$ or $0.027\,\mathrm{pc}$, corresponding to $4000 \pm 300\,\mathrm{yr}$ in kinematic age. Further outside the arm follows a constant decline in intensity showing no additional emission source.

In the lower right image, the NW direction is presented. The deconvolved images show the existence of a fainter arm which is also visible in the intensity plot as the outer rim of the first plateau at $\approx 50''$ ($0.033\,\mathrm{pc}$; $5000 \pm 300\,\mathrm{yr}$). In contrast to the NE side the emission extends further out until $75''$ ($0.05\,\mathrm{pc}$; $7500 \pm 400\,\mathrm{yr}$), as the second small plateau indicates.
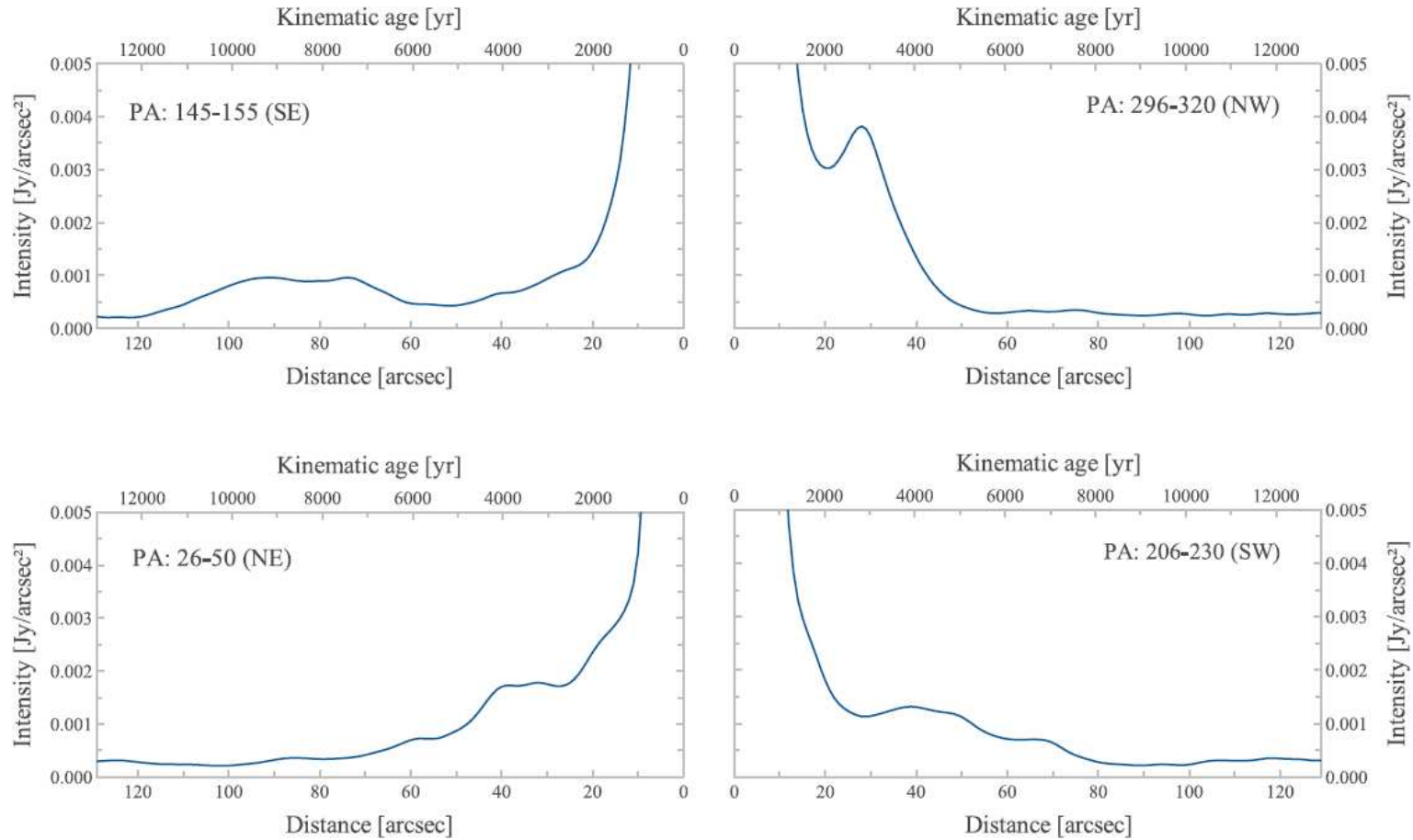
Figure 3.10.: Integrated intensity cuts for X Her from the deconvolved PACS image at $70\,\mu$m along two lines through the star by Jorissen et al. (2011). One line is along the space motion of the star and the other perpendicular to it. The kinematic ages on the upper scales are derived with the wind expansion velocity of $6.5\,\mathrm{km\,s^{-1}}$ (González Delgado et al. 2003).

3.2.2. TX Psc

Compared to the surrounding of X Her discussed in the previous Section, the CSE of TX Psc has a different outline but is not less attractive. A closer look to the object offers Fig. 3.11, where again the space motion with respect to the LSR is indicated by an arrow and the length of the arrow gives the position of the star after a given time. The upcoming analysis is fully based on the $70\,\mu$m images (Fig. 3.11) because it contains the same features as in the $160\,\mu$m image but with a better resolution.

The most significant feature in the images of TX Psc is the strong ring like structure around the star, seen especially in the lower panel of Fig. 3.11. The structure is more a ring than a disc, which means that its brightness is not homogeneous and the rim is brightened. The intensity profiles in Fig. 3.12 show that the ring is almost perfectly circular which is also a clear indication that the mass loss was isotropic at a time and the freely expanding stellar wind does not feel the oncoming ISM. This is contrary to the bipolar flow that was detected by Heske et al. (1989); Richichi et al. (1995) and Cruzalebes et al. (1998). A bipolar flow would form a distorted CSE. In addition, the circular shape means that the inclination of the structure is negligible otherwise it would be elliptical. An explanation for the ring structure may be that this is the position of the termination shock, the region where the freely expanding stellar winds hits the shocked stellar wind (see Section 1.4.2). This would explain the spherical structure as well as the brightening. Due to the fact that there are no further data like spectroscopy for this region this remains only a hypothesis. Another feature that remains undiscussed is the bright spot in the east of the star. The Aladin Sky Atlas shows that it is a galaxy and therefore does not belong to the direct environment of TX Psc.

However, there are also clear signs of a stellar wind - ISM interaction. First of all, directly in direction of the space motion a bright density enhancement is visible outside the ring. Further investigations regarding this clump come up in Section 3.2.3. From this clump a wing like structure emerges in downstream direction, perfectly aligned to the opposite of the space motion. Furthermore, the opening angles of the wings get wider more distant from the star. This is an indication that the material feels the pressure from the oncoming ISM. Mass peels off from the bow shock head and flows in downstream direction. All together the features are different to the ones seen in X Her. There is neither a direct bow shock front visible, nor a tail like structure. The wing shape, however, was reproduced by a model of Blondin & Koerwer (1998) which is discussed in Section 4.2.

In the same manner as for X Her, integrated intensity profiles were calculated

for the deconvolved image of TX Psc. A wedge of 22° was chosen to fully cover the clump in the upstream direction. Over this area the profiles were calculated along the direction of the space motion and perpendicular to it and the results are shown in Fig. 3.12. The dynamical age was calculated with the expansion velocity of the wind $v_{\mathrm{w}} = 10.5 \, \mathrm{km \, s^{-1}}$ derived by Olofsson et al. (1993).

The intensity of the region in direction of the space motion is mapped in the lower right panel of 3.12. The intensity was integrated to cover the whole clump in the south west of PA 228–250°, starting from north over east. The profile shows two big humps and a steep decline outwards. The inner hump gives the intensity of the ring structure. The peak is not well defined and shows more an extended plateau than a peak, ranging from $14''$–$22''$, or 0.019–0.029 pc. Though, the highest emission is reached at $17''$ (0.023 pc) which corresponds to a kinematic age of 2100 ± 300 years. The second hump is a more defined peak at a distance of $29''$ (0.039 pc; 3600 ± 400 yr) and shows the emission of the clump that is in direction of the space motion. More outward the intensity declines continuously showing no other emission features.

The lower left panel shows the intensity of the region opposite to the space motion from PA 48–70° in the north east. The profile has a shoulder with a peak intensity at $17''$ which is again the inner ring. Further out the intensity falls down towards a very low emission that is measurable until $52''$ (0.069 pc; 6500 ± 700 yr) when it drops under the 3σ-level of the background emission. This is a sign that there is still weak emission from material in the downstream regime of TX Psc that is not directly brightened by the interaction interface.

Both upper panels of Fig. 3.12 show the intensity along a line that is perpendicular to the space motion of the star. In the upper left panel the intensity of a region in the south east (PA 138–160°) is plotted. The ring is again visible at $17''$ as well as an extended faint emission that corresponds to the southern wing structure. The same picture gives the upper right panel (covering a PA 318–340°) putting the ring at a distance of $18''$ (0.024 pc; 2200 ± 300 yr) with a faint extended emission from the northern wing up to $60''$ (0.08 pc; 7500 ± 800 yr).
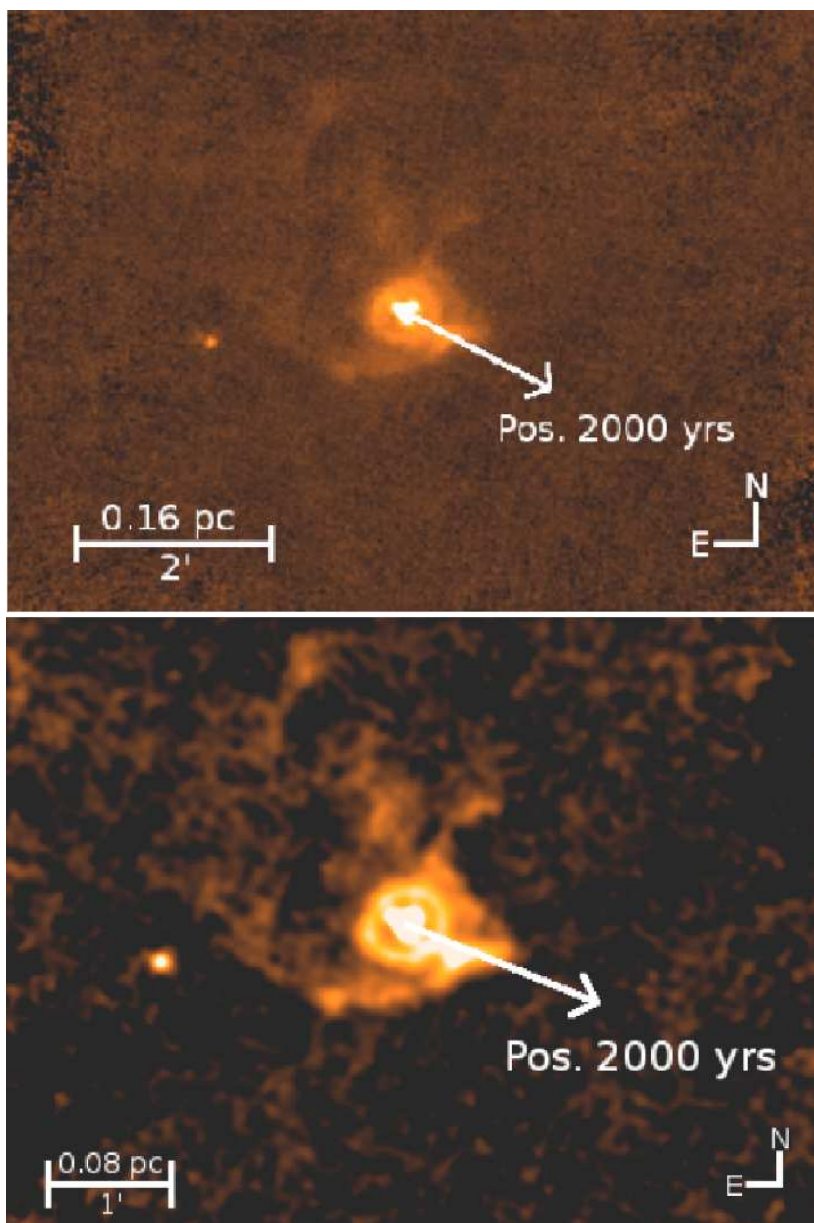
Figure 3.11.: PACS images of TX Psc in the blue channel at $70\,\mu$m (Jorissen et al. 2011). The upper image was produced with Scanamorphos, in the lower image also deconvolution was applied. In both images the arrows indicate the direction of the space motion and the position in 2000 yr. The bright source to the east of TX Psc is a galaxy and does not belong to the star's environment.

71
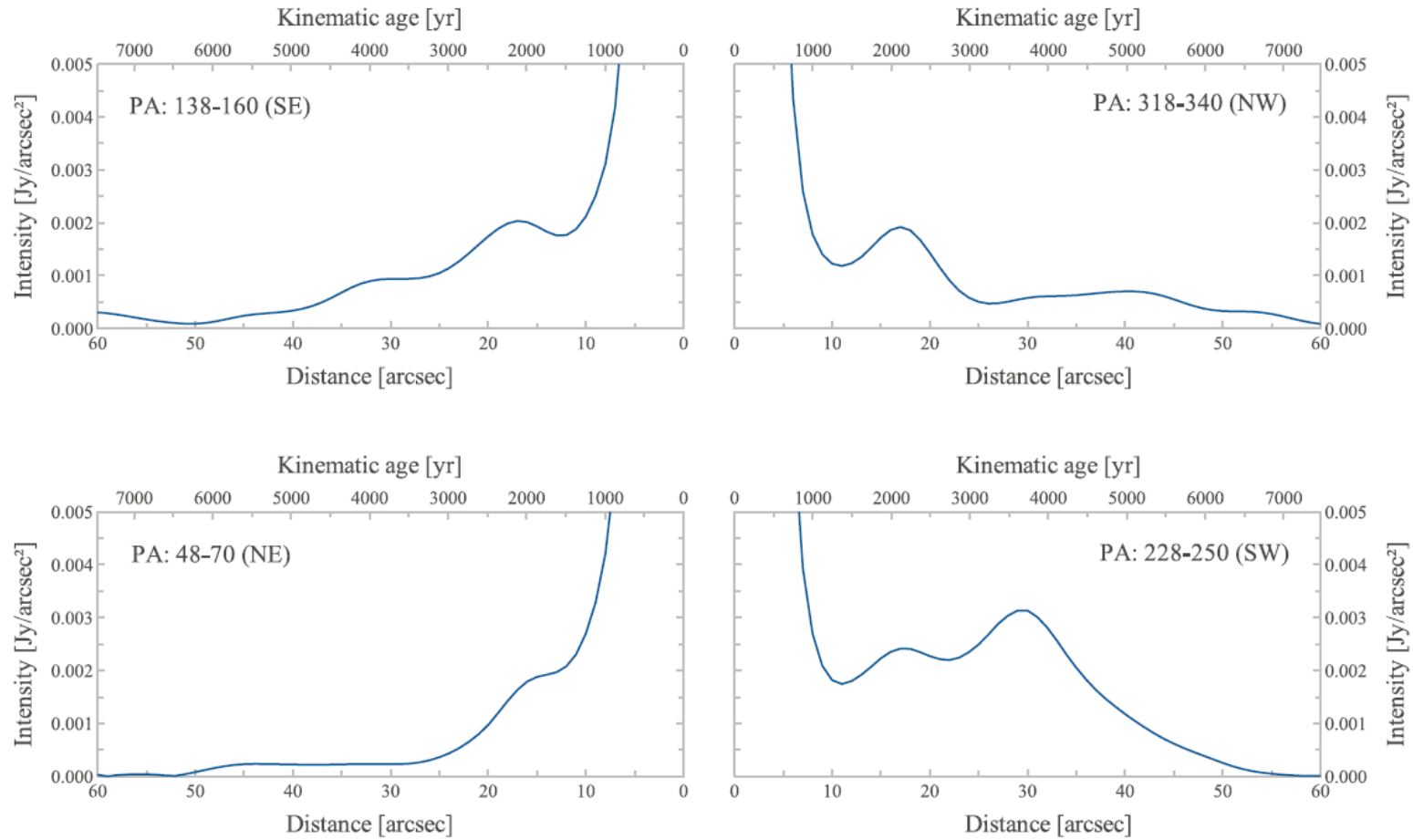
Figure 3.12.: Intensity cuts for TX Psc from the deconvolved PACS image at $70\,\mu$m along two lines through the star by Jorissen et al. (2011), similar to Fig. 3.10 for X Her. One line is along the space motion of the star and the other perpendicular to it. The kinematic ages on the upper scales are derived from the wind expansion velocity of $10.5\,\mathrm{km\,s}^{-1}$ (Olofsson et al. 1993).

3.2.3. Properties of the upstream clumps

The clumps in both objects are remarkable features that are not expected when considering an interaction scenario as described in the introduction of this work. In Section 4.2 the possible origins of these structure are presented. In this paragraph the clumps are examined with photometry. Since spectroscopic Herschel data for TX Psc and X Her are missing the remaining method is to measure the intensities through aperture photometry in both wavelength bands and derive the temperature with help of Kirchhoff's law of thermal radiation and the Planck distribution of radiation.

The aperture photometry is done in HIPE, where two automatic tasks are available: fixed sky aperture photometry (fixedSkyAperturePhotometry) and anular sky aperture photometry (anularSkyAperturePhotometry). The first task allows to chose an own background flux value that is then subtracted from the source, while the second task determines the background flux from a circular area around the source. Since the clumps are not point sources and embedded in mass loss material, the fixed sky aperture photometry task is the one that has to be used here. The task works fully automatically with a user interface that asks for the center of the source, the radius over which the flux should be integrated and the background flux per pixel. To estimate the background a region has to be chosen where no emission is visible despite the one coming from the background. An adequate region was selected and with an aperture radius of 10 pixels the background for the Scanamorphos images in both bands was estimated as 3×10^{-4} Jy per pixel in the blue and 5×10^{-4} Jy per pixel in the red band.

The center of the TX Psc clump has the coordinates

$$\alpha = 23\text{h}\,46\text{min}\,22\text{s} \qquad \delta = +03°\,28'\,56''$$

and a radius of 5 arcsec was chosen to fully cover the clump's extension. The total fluxes that are calculated by the task are 0.191 Jy at $70\,\mu$m and 0.039 Jy at $160\,\mu$m or a flux ratio $F_{\nu,70}/F_{\nu,160} = 4.89$. The intensity profiles for both bands in direction of the clump are shown in the lower panel of Fig. 3.13.

The calculation of the temperature of the clumps is based on the assumption that the far-IR emission originates only from cold dust. In principal the emission could also be from emission lines like [O I] at $63\,\mu$m, [O I] $145\,\mu$m or [C II] $158\,\mu$m that are within the bandwidth of both PACS filters. The lack of spectroscopic data prevents to assign the emission to thermal dust emission or atomic lines. However, a new Spitzer/IRS spectroscopic observation of the bow shock front of R Hya show no atomic lines (Ueta 2011) and the author suggests that the emission originates from cold dust with a temperature of

20–40K. This hypothesis was also discussed before by van Buren & McCray (1988) and Dgani et al. (1996a) with the same result.

The temperature estimation works as follows. From the Kirchhoff law of thermal radiation the dust emissivity j_ν can be written as

$$j_\nu = k_\nu j_{\mathrm{BB},\nu}(T), \tag{3.1}$$

where k_ν is the dust absorbing coefficient and $j_{\mathrm{BB},\nu}$ the black body emissivity at a frequency ν from the Planck law

$$j_{\mathrm{BB},\nu} = \frac{2h\nu^3}{c^2}\,\frac{1}{e^{\frac{h\nu}{kT}} - 1}, \tag{3.2}$$

where c is the speed of light, h the Planck-constant and k the Boltzmann-constant. TX Psc is a carbon star (see Section 2.1), thus the absorption coefficient has to be valid for amorphous carbon. The matching value for the coefficient as a function of the wavelength was found in Draine (1981) who gives so-called Q-factors, a ratio of the absorption cross section to the geometrical cross section of the dust grain. As the Q-factors are proportional to k_ν the flux ratio can be written as

$$\frac{F_{\nu,70}}{F_{\nu,160}} = \frac{Q_{70}}{Q_{160}}\frac{j_{\mathrm{BB},70}(T)}{j_{\mathrm{BB},160}(T)}. \tag{3.3}$$

For amorphous carbon Draine (1981) gives $Q_{70}/Q_{160} = 512/219 = 2.34$. Putting this ratio and the ratio for the fluxes at both bands into the upper equation gives us the temperature T of the clump. For TX Psc a temperature of $81\,\mathrm{K}$ returns from this calculation.

The temperature estimation for the clump in the environment of X Her works in the same manner. The center of the clump, which is located at PA 7–17° has the coordinates

$$\alpha = 16\mathrm{h}\,02\mathrm{min}\,39\mathrm{s} \qquad \delta = +47°\,15'\,04''.$$

Again a radius of 5 arcsec was chosen to cover the size of the clump. The aperture photometry provides then a flux ratio $F_{\nu,70}/F_{\nu,160} = 4.56$. Because of the nature of X Her as an oxygen-rich star, the Q-factors for astronomical silicates adopted from Draine (1981) are $Q_{70}/Q_{160} = 185/25 = 7.4$. This values yield then a temperature of $40\,\mathrm{K}$ for the clump of X Her.
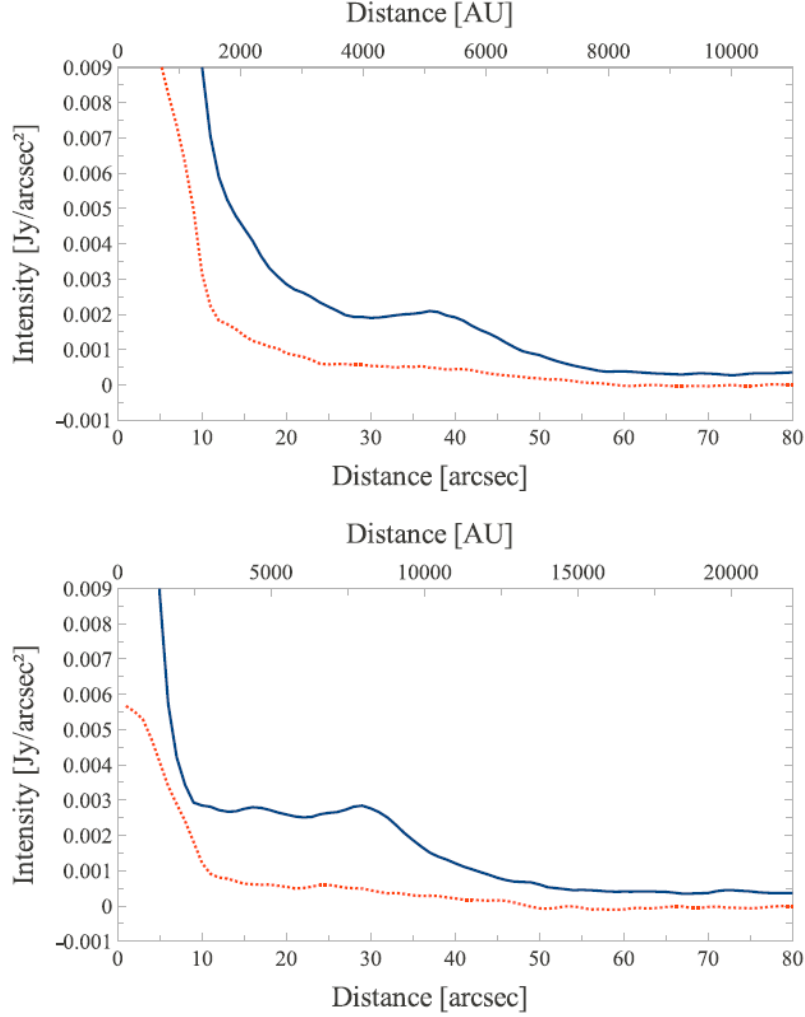
Figure 3.13.: Intensity plots for X Her (upper panel) and TX Psc (lower panel) from Scanamorphos images by Jorissen et al. (2011). In both panels the blue continuous line corresponds to the intensity at $70\,\mu$m and the red dashed line to $160\,\mu$m. The upper scales give again the kinematic age based on the wind velocities discussed in the previous paragraph. The intensity of X Her was integrated over a PA of 7–$17°$ and of TX Psc over a PA of 228–$250°$ to fully cover the clumps.

4. Models and simulations of stellar wind – ISM interaction

The theoretical part of stellar wind expansion and the interaction with the ISM was described in Section 1.5.1 while in Section 1.5.3 the observational aspects were discussed and finally in Section 3.2 the new images of TX Psc and X Her were presented and the observed features analysed.

A next logical step is the connection between the physics and the observations of bow shocks. This is the topic of the following chapter. To compare these two fields it is necessary to visualize the theory in form of numerical simulations. Various of these simulations have been carried out in the past. Their physical considerations are presented and how they match the observational constraints. Simulations give a direct hint to the key mechanisms of the interaction and also allow to adjust parameters and see directly how it affects the result. An overview of previous simulations and their results are given together with the input parameters like the velocity of the star, the densities of the wind and the ISM and the cooling rate in the shocked region.

But first the analytic solution of the stellar bow shock (see Section 1.5.1) is tested by a fit to the observed CSEs of TX Psc and X Her.

4.1. The Wilkin Fit

4.1.1. Fitting of AGB-star bow shocks

In Section 1.5.1 the relation for the shell's shape was derived. With this relation it is theoretically possible to determine the 3D orientation of the bow shock cone in space by fitting the Wilkin equation to the observed interaction outline. In the simplest case of a space motion in the plane of the sky (inclination angle $0°$) one can measure R_0 directly from the observation. It gets more complex when the space motion of the star and therefore the bow shock is inclined with respect to the plane of the sky. The observed bow shock shape is then a geometric projection of the 3D wilkinoid on the 2D plane of the sky. The geometry of the bow shock is, additionally to the stand-off distance R_0 and the position angle ϕ, described by an inclination angle i. By dealing with projections it is important to keep in mind that all lengths of the projection change with the inclination angle. This is also the case for the observed and projected R_0. The deprojected stand-off distance is in the following $R_{0,\mathrm{d}}$. With this parameters the 3D wilkinoid and thus the projected and observed stellar bow shock are fully described on the condition that the far-IR emission is due to thermal dust emission. The first calculation of the 3D orientation of a stellar bow shock after the Wilkin curve was performed by Ueta et al. (2008) on AKARI/FIS images of Betelgeuse (α Ori). The authors found for the deprojected stand-off distance $R_{0,\mathrm{d}} = 4.8 \pm 0.1$ arcsec, the inclination angle $i = 56° \pm 4°$ and the position angle $\phi = 55° \pm 2°$. The accuracy of the result is however doubtful and the method of calculation has to be checked more precisely.

The fitting process described by Ueta et al. (2008) works as follows. From the image file of the object several points in pixel-coordinates are extracted that lie on the brightened bow shock outline. This can be done simply by hand or more sophisticated with a routine that extracts the coordinates of points over a given brightness threshold. Both methods yield comparable results. With the obtained pixel coordinates of the bow shock outline and the star, the shape can be centred on the star position. The fitting routine rotates the points with an angle ϕ around the point of origin by multiplying the pixel coordinates with the two dimensional rotation matrix

$$Rot = \begin{pmatrix} \cos\phi & -\sin\phi \\ \sin\phi & \cos\phi \end{pmatrix}. \qquad (4.1)$$

On every variation step of the angle a quadratic equation in form of $y = ax^2 + bx + c$ is fitted to the points and the best fit is determined by the least deviation of all points. With this method the parameter c of the quadratic

equation gives the observed, projected R_0. The value for $y = 0$, hereafter B, is the distance from the star to the bow shock at the angle $\theta = 90°$ with respect to the symmetry axis of the bow shock. With the Wilkin equation for the bow shock shape the deprojected stand-off distance $R_{0,\mathrm{d}}$ can be derived with

$$B = R(90°) = R_{0,d} \cdot \sqrt{3}. \tag{4.2}$$

The assumption that $R_{0,\mathrm{d}}$ is deprojected stems from the consideration that the length B does not change when tilting the bow shock cone by an inclination angle i since it is also in the plane wherein the star lies. It is shown later that this assumption is not valid in case for a projection of the inclined 3D body on the 2D plane and a further determination of the inclination angle through a projection

$$i = \arccos\left(\frac{R_{0,\mathrm{d}}}{R_0}\right) \tag{4.3}$$

is geometrically not feasible.

For this reason a new concept for the Wilkin Fit was developed together with Roland Ottensamer, Franz Kerschbaum and Armin Luntzer and is described in the MESS overview paper for AGB wind - ISM interaction by Cox et al. (2011). The realisation and implementation for HIPE was done by Roland Ottensamer and Armin Luntzer.

The concept is based on the projection of a 3D rotational body based on the Wilkin relations for $R(\theta)$ that are mentioned in Section 1.5.1. The wilkinoid in parametric representation can be written as:

$$x = R(\theta) \cos i \tag{4.4}$$

$$y = R(\theta) \sin i \cos i \tag{4.5}$$

$$z = R(\theta) \sin i \sin i. \tag{4.6}$$

The envelope of this rotational body is then filled with a certain number of points by a Monte Carlo simulation. The simulation fills the area of every angle randomly with the same amount of points to simulate the brightness coverage of the optical thin wilkinoid. These points can be seen as green dots in Fig. 4.2. The rotation is then described by the 3D rotation matrices

$$Rot_x = \begin{pmatrix} 1 & 0 & 0 \\ 0 & \cos\phi & -\sin\phi \\ 0 & \sin\phi & \cos\phi \end{pmatrix} \tag{4.7}$$

$$Rot_y = \begin{pmatrix} \cos\phi & 0 & \sin\phi \\ 0 & 1 & 0 \\ -\sin\phi & 0 & \cos\phi \end{pmatrix} \quad (4.8)$$

$$Rot_z = \begin{pmatrix} \cos\phi & -\sin\phi & 0 \\ \sin\phi & \cos\phi & 0 \\ 0 & 0 & 1 \end{pmatrix}. \quad (4.9)$$

The fitting process works completely interactive in HIPE. By defining the star's position and the estimated position of the bow shock apex on the image, the generated points on the envelope of the wilkinoid are rotated around the z-axis by the position angle of the apex.

By inclining the wilkinoid, which is equal of a rotation of the body around the y-axis, the outline of the bow shock gets significantly changed. The final projection is done by setting the z-values of all points equal zero. The left panel of Fig. 4.1 shows the variation of the observed stand-off distance R_0 (A in the figure) with the inclination angle i. R_0 is the prolongation of $R_{0,\mathrm{d}}$ by a factor $q(i)$

$$R_0 = R_{0,d} \times q(i). \quad (4.10)$$

The values $q(i)$ can be found in the Appendix A.2.

The left panel of Fig. 4.1 shows a remarkable fact. The overall outline of the wilkinoid does not change much with an increasing inclination angle. This can be seen in the dashed line which represents the uninclined $B = \sqrt{3}A$ and the continuous line of the inclined B. The differences over all inclination angels can practically not be distinguished as they are in the order of a few percent and insignificant compared to the turbulent shape of an observed bow shock. This means that the observed shape of bow shock cannot be used for an estimation of the inclination angle i. The right panel of Fig. 4.1 shows this fact with an illustration of a wilkinoid that is inclined by several angles.

Since the determination of the inclination angle of the bow shock from the projected shape fails, the only remaining possibility is to determine the inclination angle from the space motion of the star. This has not to be the inclination angle of the bow shock by definition, as the local ISM flow can vary from the galactic motion, but it is a good approach for the bow shock inclination. The inclination to the plane of the sky is defined by

$$i_* = 90 - \arccos\left(\frac{v_{\mathrm{LSR}}}{R_{\mathrm{v,LSR}}}\right), \quad (4.11)$$

where v_{LSR} is the space velocity and $R_{\mathrm{v,LSR}}$ the radial velocity corrected from solar motion. A description to the calculation of this values can be found in
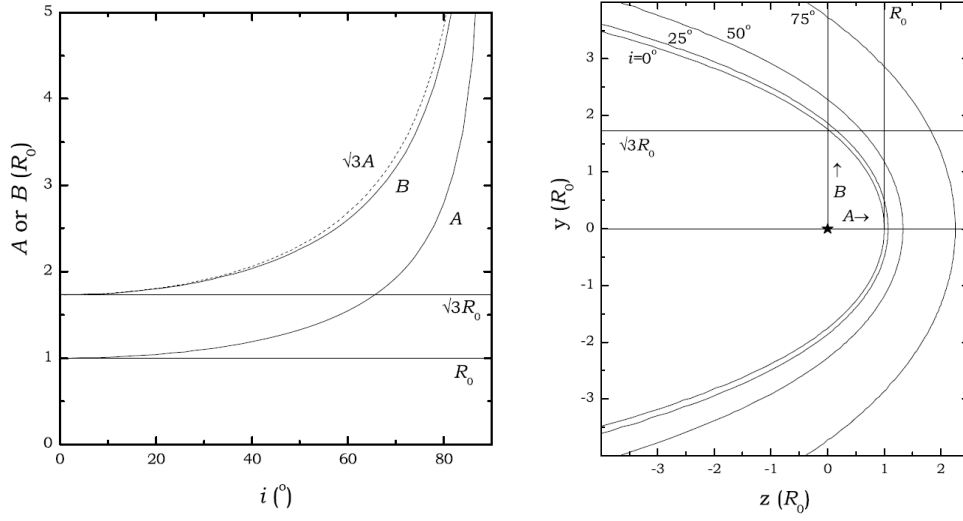
Figure 4.1.: *Left panel*: Variation of the observed stand-off distance $A = R_0$ as a function of the inclination angle i by Cox et al. (2011). B is the distance from the star to the bow shock at $\theta = 90°$. The dashed line shows the B value for an uninclined body $\sqrt{3}A$. The differences between $\sqrt{3}A$ and B are marginal over all angles. *Right panel*: Outlines of a wilkinoid tilted by several angles by Cox et al. (2011). The size of the bow shock increases since R_0 also increases with i, the shape of the outline however remains very close to an uninclined wilkinoid.

Section 2.2. The inclination angle can then be inserted in the interactive fitting routine to check if the theoretical projected shape fits to the observed one. In this interactive part R_0 and the position angle ϕ can be varied to obtain the best fitting parameters.

With the obtained $R_{0,d}$ it is possible to derive the missing parameters from the equation for the stand-off distance. In practice this is the determination of the ISM density ρ_0, since all other parameters are fairly determined from observations.

4.1.2. The Wilkin fit performed on TX Psc and X Her

By having the analytic outline of a thin shell stellar bow shock in mind it seems rather difficult to fit it to the turbulent and distorted shapes of TX Psc and X Her as seen in Section 3.2. Nevertheless, the fitting process was performed with the Scanamorphos $70\,\mu$m images of both objects. The results can be seen in Fig. 4.2 and Table 4.1. As anticipated, the theoretically predicted outline,

Table 4.1.: Parameters for the Wilkin Fitting on TX Psc and X Her.

Object	R_0 [″]	B [″]	$R_{0,\mathrm{d}}$ [″]	$R_{0,\mathrm{d}}$ [pc]	PA [°]	i [°]
TX Psc	38	46	37	0.049	238	14
X Her	45	68	36	0.022	330	-55

indicated by green dots, does not fit well to the observed structures on both stars.

The opening angle of the Wilkin fit to TX Psc is much too wide, the green dots from the Monte Carlo simulation hardly coincide with the observed outline. The stand-off distance given by the upstream knot is too large and hence the Wilkin curve is oversized. Even more, the north-east part of the density enhancement lies outside of the bow shock front but by augmenting R_0 the rest of the observed structure would even match less. Due to the strong vortices in the downstream region of TX Psc, the Wilkin fit does not seem to reflect the observed structure of the CSE.

This is also the case for X Her. The bump in the bow shock front can not be rendered by the Wilkin model, the differences between the fit and the observed shape are tremendous. The tail structure is in contrast to the Wilkin equation that produces a wider shape. Despite the bump the fit is well until $\theta = 90°$ when the Wilkin curve opens stronger and the observation shows a tail structure. The distance to the symmetry axis to the observed bow shock is over all angles much smaller than predicted by the theory, which is also the case for TX Psc.

To probe the obtained results the ISM density close to the objects can be derived from the stand-off distance

$$R_0 = \sqrt{\frac{\dot{M} v_{\mathrm{w}}}{4\pi \rho_0 v_*^2}}. \tag{4.12}$$

The results of the calculation are shown in Table 4.1.2. The ISM density ρ_0 was converted to a hydrogen density n_{H}. The hydrogen densities can also be

Table 4.2.: Input parameters and the resulting ISM density.

Object	$R_{0,\mathrm{d}}$ [pc]	$\dot{M}$ $[M_\odot\,\mathrm{yr}^{-1}]$	v_w $[\mathrm{km\,s}^{-1}]$	v_* $[\mathrm{km\,s}^{-1}]$	n_{H} $[\mathrm{cm}^{-3}]$
TX Psc	0.049	9.1×10^{-8}[a]	10.5[a]	67.9	0.16
X Her	0.022	1.5×10^{-7}[b]	6.5[b]	89.9	0.67

References:
(a): Olofsson et al. (1993)
(b): González Delgado et al. (2003)

estimated from the galactic height z. After Mihalas & Binney (1981) the ISM density drops with

$$n_{\mathrm{H}}(z) = 2.0\ e^{-\frac{|z|}{100\,\mathrm{pc}}}. \tag{4.13}$$

The observed distances to the galactic plane are $z = 227\,\mathrm{pc}$ for TX Psc and $z = 121\,\mathrm{pc}$ for X Her. This corresponds to ISM densities of $n_{\mathrm{H}} = 0.21\,\mathrm{cm}^{-3}$ and $n_{\mathrm{H}} = 0.60\,\mathrm{cm}^{-3}$, respectively, and are in good agreement with the values calculated from the stand-off distance.

As a summary it is necessary to note that on one side the Wilkin fit fails to reproduce the observed structures of both objects. The observed shells are distorted by instabilities which can not be reproduced by the momentum-support approximation that lead to the simple equation for the bow shock curve. On the other hand side, however, the surroundings of TX Psc and X Her are the worst case scenario for the fit. After applying the Wilkin fit to all of the circa 30 objects in the MESS Time Key Program catalogue that show strong stellar wind - ISM interaction most observed structures that show a more accurate coincidence with the theoretical shape. However, none of them fits perfectly since every bow shock front has some disturbances. These are the limitations of the Wilkin fit.
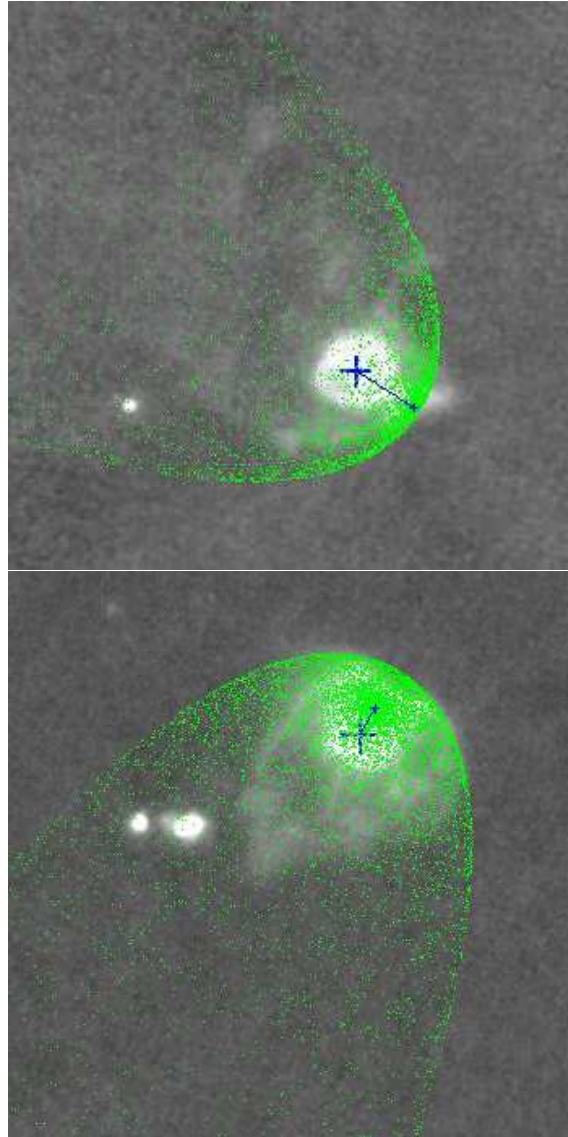
Figure 4.2.: PACS $70\,\mu$m images of TX Psc (upper panel) and X Her (lower panel) with the over-plotted projected wilkinoid (green dots). The big blue cross marks the position of the star, the blue line $R_{0,\mathrm{d}}$ and the small blue cross the apex of the bow shock. Obviously the theoretical shape does not fit well to the observed turbulent outlines of both stars.

4.2. Simulations of stellar wind bow shocks

The previous section showed that the analytic solution of the wind - ISM interaction does not provide the best results for TX Psc and X Her. The reason for this is the simplification of the model, as it is solely based on momentum support and does not include important processes like cooling of the stellar wind - ISM interface that lead to instabilities and deviation. Unfortunately, with so many free parameters it is not possible to find an exact analytic solution for this problem. It is therefore necessary to calculate numerical solutions and enhance them with physical parameters. Stellar wind bow shocks are a topic in numerical simulations since Soker et al. (1991) tested extensively the validity of the physical models of Gurzadian (1969) and Smith (1976) for a planetary nebula - ISM interaction scenario. In the following, the most important physical processes that affect the bow shock shape together with the numerical simulations that were carried out are discussed. This section is, again, based on the forthcoming paper by Jorissen et al. (2011).

4.2.1. The effect of cooling on the bow shock shell

The most significant role in the structure of the stellar wind bow shock interface plays the cooling rate of the shocked interface region of the stellar wind and the ISM. As already described in Section 1.4.2 the stellar wind bubble consists of a layer of a free flowing stellar wind that is slightly supersonic in the case of an AGB star. This wind produces a termination or reverse shock when hitting the piled up stellar wind, producing a layer of shocked stellar wind gas. This layer is followed by a contact discontinuity which separates it from the layer of shocked ISM material which is facing the stellar wind highly supersonically due to the space motion of the star. The outermost layer is a forward shock front produced by the oncoming ISM hitting the shocked ISM. The bow shock is therefore a layer bounded by the termination shock which decelerates the stellar wind and a forward shock that propagates into the ISM. The shocked layer can now cool through radiative recombination of the ionized atoms but as well through free-free emission, turbulent mixing, thermal conduction, non-equilibrium radiation losses and radiation of collisionally heated dust (Dgani et al. 1996a; Blondin & Koerwer 1998). If the density of the shocked gas is large enough, energy can be removed from the layer so that the cooling time is short compared to the flow time. The result is a collapse of the shocked layer towards an isothermal thin and dense shell.
The efficiency of cooling is determined by the cooling length which should be for rapid cooling much shorter than the stand-off distance R_0. Blondin & Koerwer

(1998) gave for the cooling length

$$L_{\mathrm{c}} \approx \frac{3}{256} \frac{\overline{m}^2 v_*^3}{\rho_0 \Lambda}, \tag{4.14}$$

where $\overline{m}$ is the average mass per particle and Λ the volume cooling rate. For a typical stellar velocity of $50\,\mathrm{km\,s^{-1}}$, a cooling rate of $10^{-21}\,\mathrm{erg\,cm^3}$ and an ISM density of $n_{\mathrm{H}} = 1\,\mathrm{cm^{-3}}$ the cooling length is in the order of $1.5 \times 10^{15}\,\mathrm{cm}$, far smaller than the stand-off distances of $1.5 \times 10^{17}\,\mathrm{cm}$ and $7 \times 10^{16}\,\mathrm{cm}$ derived in Section 4.1.2 for TX Psc and X Her, respectively. The forward shock is thus cooled effectively. In addition, also the reverse termination shock can rapidly cool because radiative cooling is enhanced by slow and dense stellar winds, as it is the case for AGB stars (Blondin & Koerwer 1998).

Nevertheless, if the density of the ISM is low, the cooling length can become comparable to the stand-off distance. The cooling might then not be efficient and this limits the compression of the shell. The shock is adiabatic and the shell remains very hot, of low density and thick (Comeron & Kaper 1998). The thickness of both kinds of shells, thick and thin, can be calculated easily. The mass balance in both approaches is dominated by the piled up mass from the interstellar gas:

$$m = \frac{4\pi}{3} \rho_0 R^3 = 4\pi R^2 \Delta R \rho_1, \tag{4.15}$$

where ΔR is the thickness and ρ_1 the density of the shell. Simplified it can be written as

$$\frac{\Delta R}{R} = \frac{\rho_0}{3\rho_1}. \tag{4.16}$$

The compression of a shock front was already discussed in Section 1.4.4 and has the form

$$\frac{\rho_1}{\rho_0} = \frac{(\gamma - 1)P_1 + (\gamma + 1)P_0}{(\gamma + 1)P_1 + (\gamma - 1)P_0}. \tag{4.17}$$

For a strong shock, $P_1 \gg P_0$ the ratio can be simplified to

$$\frac{\rho_1}{\rho_0} = \frac{\gamma + 1}{\gamma - 1}. \tag{4.18}$$

This leads for an ideal 1-atomic gas with $\gamma = 5/3$ to a compression rate of $1/4$. The upper boundary for a thick shell is then given by

$$\frac{\Delta R}{R} = \frac{\gamma - 1}{3(\gamma + 1)} = \frac{1}{12}. \tag{4.19}$$

For an isothermal ($\gamma = 1$) thin shell approach the Mach number M comes into the relation and the result is

$$\frac{\Delta R}{R} = \frac{1}{3M^2}. \qquad (4.20)$$

Both approximations, the thin shell with efficient cooling and the thick shell without efficient cooling lead to instabilities that are of different appearance. In the following paragraph the most important instabilities are presented.

4.2.2. Instabilities in thin shell shock fronts

The isothermal thin shell shock front can be distorted by three mayor forms of instabilities, the *non-linear thin shell instability* (NTSI), the *transverse acceleration instability* (TAI) and the *Kelvin-Helmholtz instability* (KHI), which are caused by different perturbations but connected to each other. While the first two instabilities are limited to the thin shell approach, the KHI is independent of the thickness of the shell.

The NTSI was first described in an analytic analysis of a planar shocked slab by Vishniac (1994). It is generated when a perturbation displaces the planar with the perturbation wavelength larger than the slab thickness, as shown in Fig. 4.3. This perturbation is also called a bending mode and is comparable to the curvature of the bow shock outline. Inside the displaced slab gas flows in the opposed direction at the boundaries which corresponds at the bow shock to the reverse and forward shock. The net result is not a transport of mass but a transport of momentum to the points of maximum displacement (Vishniac 1994). The enhanced momentum flux in the interior of the slab lead to even more displacement and non-linear wiggles and ripples in the thin shock bounded shell (Blondin & Koerwer 1998). However stabilizing forces like the ram pressure tend to fill the ripples, the NTSI is not completely suppressed.

The theory of the second instability, the TAI, was developed by Dgani et al. (1996a,b) on a planar zero-thickness shocked slab, thus allowing no internal flow that occurs at the NTSI. The TAI considers only the effect on the two sides of the slab. The authors found two distinct modes: a longitudinal (breathing) mode and a transversal (bending) mode.

The physical reason for the breathing mode is an additional small mass element on the surface of the slab. This is increasing the surface density and decreasing the acceleration that the element feels from the longitudinal flux. The element lacks behind in the flow and accretes more mass.

The bending mode arises from motion normal to the surface of the slab. This
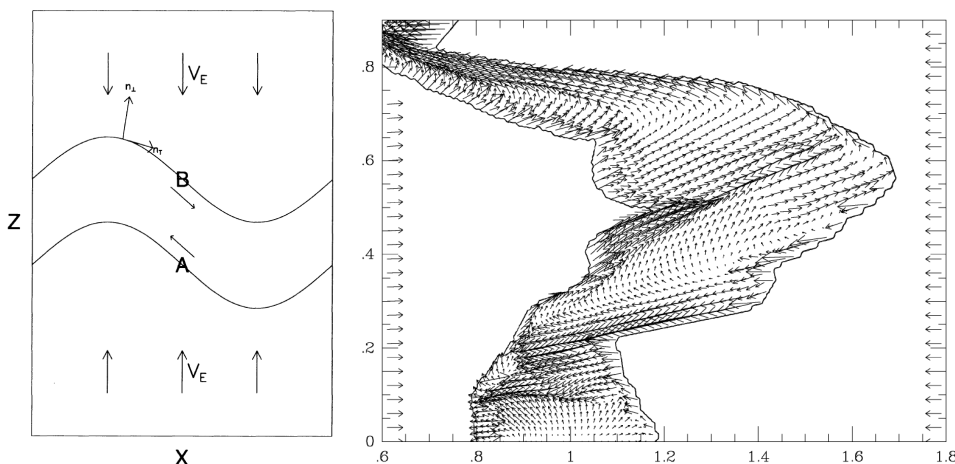
Figure 4.3.: *Left panel*: Schematic view of the oppositional flows in a shocked slab with a large bending mode by Vishniac (1994). A and B are the boundaries of the slab, comparable to the reverse and forward shock of the bow shock interface. The bending is also similar to the curvature of the parabolic bow shock front. *Right Panel*: Simulation of the shear flow in a shocked and bent slab by Blondin & Koerwer (1998).

changes the momentum flux and leads to an unstable ram pressure equilibrium. When the shocked slab collides with the ambient medium, the slab is pushed away from the equilibrium and starts to oscillate around the equilibrium position.

Dgani et al. (1996a) compared also the growth rates of both instabilities and found that the TAI grows faster than the NTSI if

$$\frac{l}{R_0} > \frac{2\pi R_0}{M^2 \lambda}, \tag{4.21}$$

where $2\pi/\lambda$ is the wavenumber of the unstable mode. This relation shows that the TAI grows faster for $l > R_0$, thus in the outer wings of the bow shock, where the growth rate for the NTSI is so small that the instability is being advected away. For large Mach numbers the zone where the NTSI dominates shrinks, however, at the apex of the bow shock it is always the dominating instability (Blondin & Koerwer 1998). The same authors also suggest that the NTSI is responsible for fast distortions near the bow shock apex. The distortions are getting advected towards the bow shock wings where the TAI amplifies them. The third instability, the KHI, is the most common instability among the three introduced. In general, KHIs occur when a shear velocity is
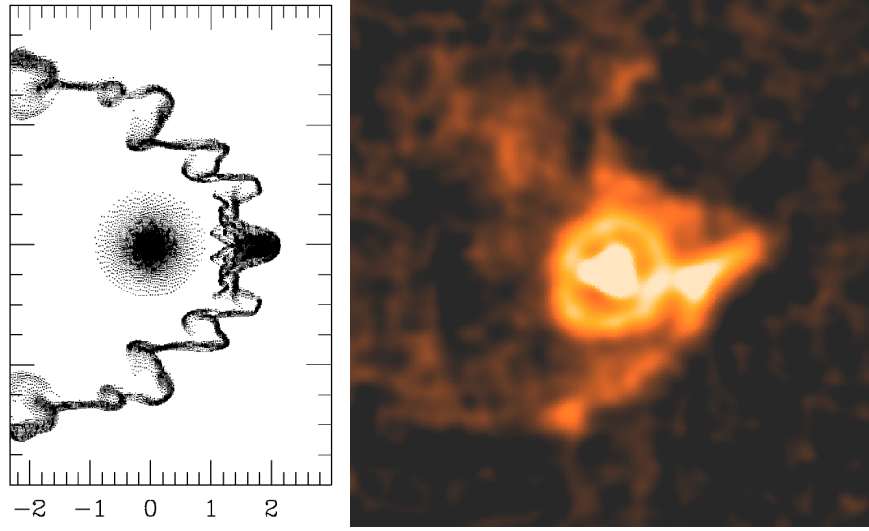
Figure 4.4.: Comparison of simulation and observation of bow shock structure. The left panel shows a Mach 10 stellar wind bow shock model by Blondin & Koerwer (1998). The right panel shows a deconvolved image in the blue band ($70\,\mu$m) of TX Psc. The simulation resemble well the clump structure in direction of the space motion that is dominant in the observation TX Psc. It also reproduces the wing like structure that extends far into the ISM.

present at the boundary between two fluids, so that one of the fluids is moving with a higher velocity than the other. The instability is visible as ripples and waves in the contact region of the fluids. In case of stellar wind bow shocks the KHI plays a similar role as the TAI when the shocked ISM flows downstream to the bow shock wings and produces ripples and waves on the bow shock shell. The growth time of the KHI is short compared to the other instabilities (Brighenti & D'Ercole 1995). When the produced waves are pushed further downstream the waves turn into vortices that are carried away from the bow shock shell (Wareing et al. (2007b); see also Section 4.3). Although, Dgani & Soker (1998) state that the KHI at the wind - ISM interface gets suppressed by the magnetic field as suggested by Chandrasekhar (1961). This would then lead to straight arms at the sides of the bow shock.

The analytic analysis of the NTSI and TAI by Vishniac (1994) and Dgani et al. (1996a), respectively, opened the field for Blondin & Koerwer (1998) and Comeron & Kaper (1998) and their extensive numerical simulations.
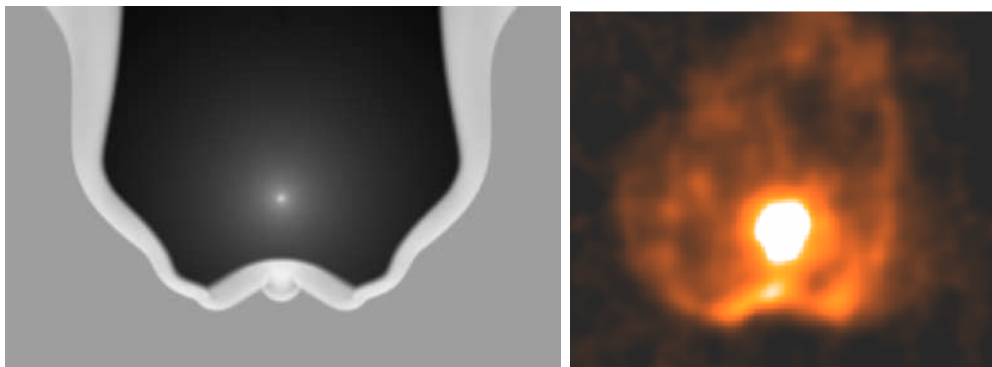The simulations by Blondin & Koerwer (1998) concentrate on the wind veloc-

Figure 4.5.: Comparison of simulation and observation of a bow shock structure. The left panel shows a model of instantaneous cooling in the simulation of Comeron & Kaper (1998), where the thickness of the shell is nearly zero. The right panel shows a deconvolved image of X Her at the $70\,\mu$m. The simulation reproduces well the bump in direction of the space motion and also the little wings next to the bump that are visible in X Her. Anyhow, it fails with the tail.

ity and the space motion of the star with a reference case of a Mach 10 stellar wind bow shock. Right from the beginning they observe instabilities in form of wiggles that distort the bow shock shell. With a wavenumber much smaller than the stand-off distance and a weaker growth rate along the wings this wiggles are a clear sign for the NTSI. Later, larger wavelength wiggles dominate the structure of the bow shock but are advected to the wings. The authors found also evidence for the TAI at the wings of the shell where segments move outward and increase the width of the bow shock outline. This feature is seen also in the observations of TX Psc where the wings of the bow shock extend far into the ISM. Also the clump in direction of the space motion is reproduced well by the simulation. A comparison of the simulation and the observation of TX Psc is shown in Fig. 4.4. It seems that the NTSI and TAI together with a strong motion of the star (Mach 10) are responsible for the observed structures of TX Psc. However, Blondin & Koerwer (1998) stress out that not the total Mach number is important for the instabilities to arise but the ratio of the wind velocity to velocity of the star through the ISM. A bow shock caused by a high space velocity is much more unstable than by a high wind velocity. This leads also to the prediction that red supergiants and AGB stars with high space velocities and slow winds are the sources for unstable isothermal bow shocks (Blondin & Koerwer 1998).

Like in the previous simulation, Comeron & Kaper (1998) concentrate mostly on the Mach number of a runaway OB star but also include its mass loss and the density of the ambient medium. In addition they include also a model for instantaneous cooling which is similar to a zero-thickness shell. In this situation the shock reverses its curvature at the apex of the bow shock and the momentum that the stellar wind injects goes into the flow parallel to the shock front. The ram pressure of the oncoming ISM pushes the bow shock closer to the star. However, when the head of the bow shock moves inwards the wing and head get detached from each other and the outer parts get swept away. The outline of this model is very similar to the observations of X Her, where a bump in direction of the space motion is noticed. Also both wings near the bump can be found in the simulation. However, there are no signs of a tail structure, rather all figures in Comeron & Kaper (1998) show a broad and wide wings. A comparison of this simulation with a deconvolved image of X Her is shown in 4.5.

The simulations by Brighenti & D'Ercole (1995) dismiss the role of the NTSI and TAI and link the appearance of instabilities in their thin shell models exclusively to Kelvin-Helmholtz instabilities. Although the simulation shows vortices in the wake of the star, they do not resemble the observed outlines of TX Psc and X Her. Not like the above mentioned, the simulation neither produces clumps in the direction of the space motion nor a reverse curvature of the bow shock.

4.2.3. Instabilities in thick shell shock fronts

When the cooling time is long the shocked ambient gas remains hot and diffuse, while on the other side of the contact discontinuity the shocked stellar wind gas is cooler and thus denser. In fluids with different densities the previous discussed Kelvin-Helmholtz instability and the well known *Rayleigh-Taylor instability* (RTI) play important roles. The RTI manifests in finger and mushroom shapes which are encountered in many planetary nebulae and supernova remnants, with the crab nebula as one of the most prominent examples for the latter.

At the interface of two fluids with different densities one of the fluids undergoes an acceleration. This can be caused by gravitation or in the case of the wind interaction by the velocity difference of the fluids. The direction of the acceleration proceeds from the lighter fluid to the heavier fluid (Soker et al. 1991) and perturbations arise at the interface. Chandrasekhar (1961) showed that the growth rate for RTI is the highest for small wavelengths. These instabilities are so strong that they can disrupt the planetary nebula shell, leaving
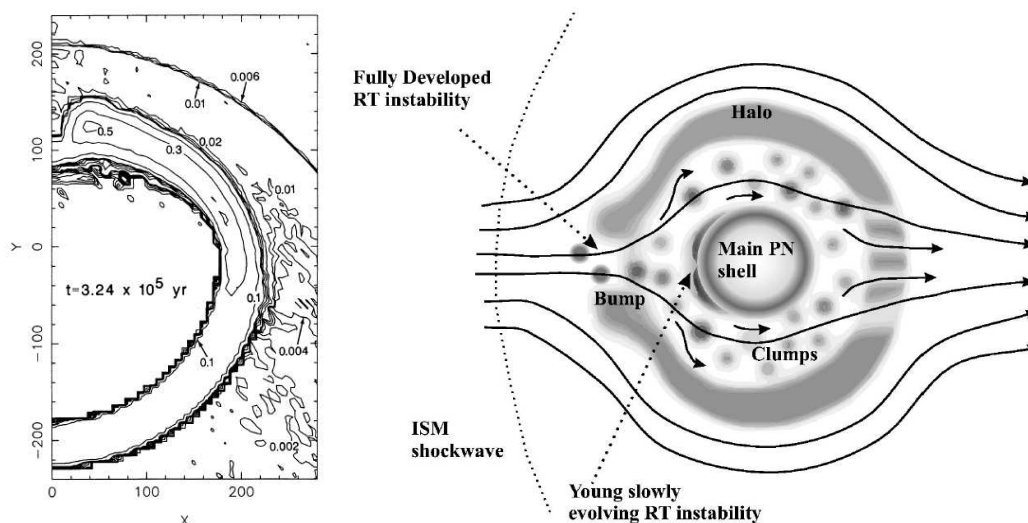
Figure 4.6.: *Left panel*: density contour map of a thick shell PN - ISM interaction model by Soker et al. (1991). The Y axis is the symmetry axis of the model and the space motion is along this axis in positive direction. The model shows a growth of RTIs in direction of the space motion. *Right panel*: schematic drawing of the fragmentation of the PN shell by the RTI (Dgani & Soker 1998). The fast ISM flows around the inner PN shell and produces new RTIs there.

it open in direction of the space motion. This happens on the time scale on which the shell is decelerated (Soker et al. 1991). After the fragmentation the ISM flows through the hole and passes the center of the nebula allowing the high speed ISM to mix with the nebula material (Dgani & Soker 1998). The same authors also give a schematic drawing of this scenario which is shown in the right panel of Fig. 4.6. One of the main thick shell simulations was carried out by Soker et al. (1991) to validate the analytic solution by Smith (1976). The simulation deals with the interaction of planetary nebulae with the ISM. The cooling time in the thick shell model is higher than the flow time of the shocked gas ($> 10^4$ yr) which is the case for velocities $v_{\rm rel} > 100$ km s^{-1} behind the shock front and a large ISM density. It is expected that most of the PNe have faster velocities and the cooling of the shocked material is thus negligible. This causes an adiabatic shell that is not compressed and remains thick.

The simulation of Soker et al. (1991) includes eight models with various space and wind velocities and ISM densities. The left panel of Fig. 4.6 shows the evolution of the fiducial model. The PN is moving along the Y axis in positive

direction. In the beginning the shell is nearly spherically symmetric with the maximum density upstream near the symmetry axis. During the evolution, RTIs appear near the symmetry axis on the upstream side in direction of the oncoming ISM. The indentation in the simulation is smooth and broad and not mushroom shaped like expected for an RTI. Anyhow, in later stages the shell disrupts at the upstream symmetry axis and creates a bump and finally a hole which is expected to happen when the RTI grows (Dgani & Soker 1998). Another model implements effective radiative cooling and shows no signs of RTI, the shell is smooth and bends towards an oval shape. As the parameters of the oncoming ISM are the same as in the previous model, the differences originate exclusively in the effective cooling. However, the simulation shows no great accordance with the observations of TX Psc and X Her. It does not produce the wing shape that can be explained with the TAI and the KHI. Nevertheless, it produces a bump or hole in the upstream region which allows the fast ISM to flow around the inner nebula shell which is analogue to the termination shock. This can produce RTIs on the termination shock with finger or mushroom shapes that are quite similar to the clump seen in TX Psc. However, the simulations with a thin shell approximation are in better consonant with the observed structures of both objects.

4.3. Simulations of AGB wind - ISM interaction

4.3.1. The PN progenitor

In the field of planetary nebulae - ISM interaction simulations are present since the late 1980s. In all these simulations the PN shell has already established before the star begins to move through the ambient medium.

The first consideration to include also the interaction of the progenitor of the PN, the AGB star, with the ISM was done by Villaver et al. (2003). The aim of the authors was to show that the interaction of the AGB wind with the ISM has large impact on the structure of the PN shell. To create an AGB star, the most important implementation is the mass loss. For the early stages of the simulation a very low mass loss rate of $10^{-8}\,M_\odot\,\mathrm{yr}^{-1}$ was chosen. This rate but also the wind velocity change continuously to simulate thermal pulses and create shocks inside the wind bubble. Apart from the mass loss rate the simulation works similar to previous simulations. Cooling was implemented for temperatures above $10^4\,\mathrm{K}$ to achieve a thin shell model.

Despite the adoption of a very conservative value of $20\,\mathrm{km\,s^{-1}}$ for the space velocity shocks are forming inside the stellar wind shell and a bow shock manifests at a distance of $0.13\,\mathrm{pc}$ but oscillates due to the changing mass loss rates. A highly asymmetric shell forms that grows in size in the downstream region. Especially the thermal pulses with their high mass loss change the outline of the outer shell. The evolution of this interaction is shown in Fig. 4.7. However, the similarity to the observations of TX Psc and X Her is not striking, since the relative velocity is much too small to develop strong instabilities.

4.3.2. Sh 2-188

Based on the results of Villaver et al. (2003) the shape of the planetary nebula Sh 2-188 was modelled by Wareing et al. (2006a) with a triple wind simulation that includes a slow AGB wind that is subsequently swept up by a faster post-AGB wind and the oncoming ISM. The AGB phase that is of interest for the present case has a mass loss rate of $\dot{M} = 10^{-6}\,M_\odot\,\mathrm{yr}^{-1}$, a moderate wind velocity $v_\mathrm{w}{=}15\,\mathrm{km\,s^{-1}}$ and a very high space velocity $v_*{=}125\,\mathrm{km\,s^{-1}}$ to represent the examined PN. Like the previous simulation this also implements cooling above $10^4\,\mathrm{K}$ for a thin shell approach.

The simulation produces a strong bow shock due to the fast movement through the ISM as well as a tail structure which is comparable to the one observed for X Her. The tail forms already in a very early stage of the evolution when material is stripped off the head of the bow shock by the ram pressure. The
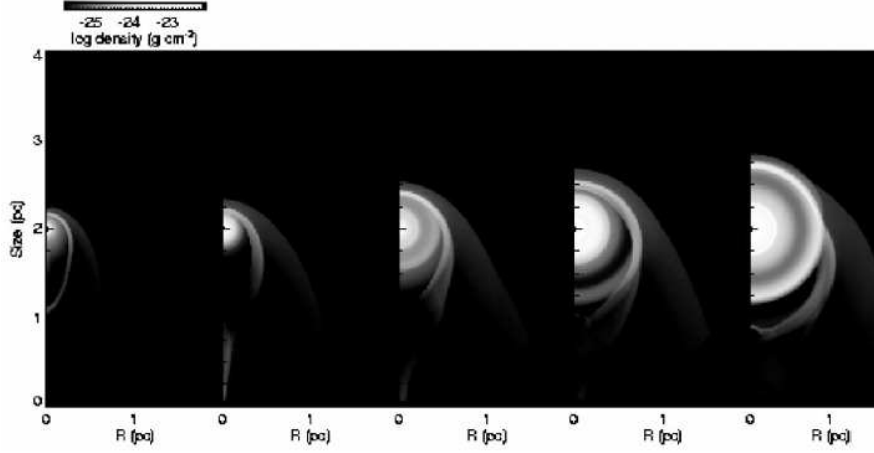
Figure 4.7.: Gas density at different stages of the evolution of an AGB wind - ISM interaction by Villaver et al. (2003). The star moves with $20\,\mathrm{km\,s^{-1}}$ through an ambient medium with n_0=$0.01\,\mathrm{cm^{-3}}$. The last two panels show the density at the end of the second and third thermal pulse, respectively.

high space velocity does not allow the flow to establish vortices as expected and the tail remains smooth. The mass loss rate is constant during this time of evolution and the bow shock remains at a stable position. This simulation, as well as the simulation of Villaver et al. (2003), is too smooth to replicate the observed structures of TX Psc and X Her in the same quality as the instability simulations by Comeron & Kaper (1998) and Blondin & Koerwer (1998). Nevertheless, the distinctive tail structure that converges is similar to the one observed for X Her. This gives a hint that it needs a large space velocity to produce this structure and X Her with a space velocity of $89.9\,\mathrm{km\,s^{-1}}$ can provide it.

4.3.3. R Hya

With the surprising observation of the first AGB star bow shock around R Hya (Ueta et al. 2006) the simulations for ISM interaction with the AGB wind gained more attention. Wareing et al. (2006b) reproduce the observed structure around R Hya with the numerical model he used for the PN Sh 2-188 (Wareing et al. 2006a). The mass loss rate ($3 \times 10^{-7}\,M_\odot\,\mathrm{yr^{-1}}$) as well as the wind ($10\,\mathrm{km\,s^{-1}}$) and the space velocity ($49.5\,\mathrm{km\,s^{-1}}$) were adopted for R Hya. The simulation was indeed able to reproduce the observed bow shock structure. Ram pressure stripping peels off material from the head of the bow shock

and moves it downstream where it cools rapidly. The head itself is smooth and the temperature of $33000\,\mathrm{K}$ is consistent with observed Hα emission.

With the same numerical two-wind model Wareing et al. (2007b,a) investigate the influence of mass loss, ISM density and space velocity on the circumstellar structure of an AGB star while the wind velocity remains constant at $15\,\mathrm{km\,s^{-1}}$. The authors applied four values for the mass loss rate from 10^{-7} to $5 \times 10^{-6}\,M_\odot\,\mathrm{yr^{-1}}$, three different ISM hydrogen densities from 2 to $0.01\,\mathrm{cm^{-3}}$ and considered values for the space velocity ranging from 0 to $200\,\mathrm{km\,s^{-1}}$. The results of both simulations are shown in Fig. 4.8.

The interaction of the wind with the ISM is already visible for a low space velocity of $25\,\mathrm{km\,s^{-1}}$. As expected from Baranov et al. (1971) the stand-off distance at this low velocity is far ahead of the star, at a distance of $2.5\,\mathrm{pc}$. The shape of the bow shock gets turbulent at $50\,\mathrm{km\,s^{-1}}$ when instabilities at the head of the bow shock get stripped off and move back down to the tail in a time span of several ten thousands years. The stand-off distance shrinks to $0.25\,\mathrm{pc}$. With higher space velocity the turbulences get serious and form high density spiralling vortices. The authors relate them to *von Karman vortex streets* that are characterized by repeated vortex shedding. Although the instabilities at the bow shock head are similar to the NTSI and TAI (see Section 4.2.2), the authors do not refer to them.

The upper panel of Fig. 4.8 shows a model with a space velocity of $125\,\mathrm{km\,s^{-1}}$ at the end of the AGB phase. A clear bent structure towards the star is visible at the bow shock with a small clump directly upstream at the direction of space motion. It also shows wings that consist of stripped off material from the bow shock head. This is very similar to the observations of X Her regarding the bent structure but as well similar to TX Psc with its wings and the upstream clump. However it fails to reproduce the tail of X Her and the ring around TX Psc.

The lower panels of Fig. 4.8 show the influence of the mass-loss on the bow shock structure. Both models have a space velocity of $75\,\mathrm{km\,s^{-1}}$, which is approximately the space velocity of TX Psc and X Her. The model in the lower left panel has a mass loss rate of $10^{-7}\,M_\odot\,\mathrm{yr^{-1}}$ whereas it is 50 times higher in the lower right. Both models show a very different shape. While the low mass loss model is bullet like without instabilities, the other shows distinct turbulences with vortices flowing downstream forming wings. Obviously, the mass loss rate has an important impact on the structure of the bow shock. However, the mass loss rates of TX Psc and X Her are with $\dot{M} = 9.1 \times 10^{-8}\,M_\odot\,\mathrm{yr^{-1}}$ and $1.5 \times 10^{-7}\,M_\odot\,\mathrm{yr^{-1}}$ lower than in both models.
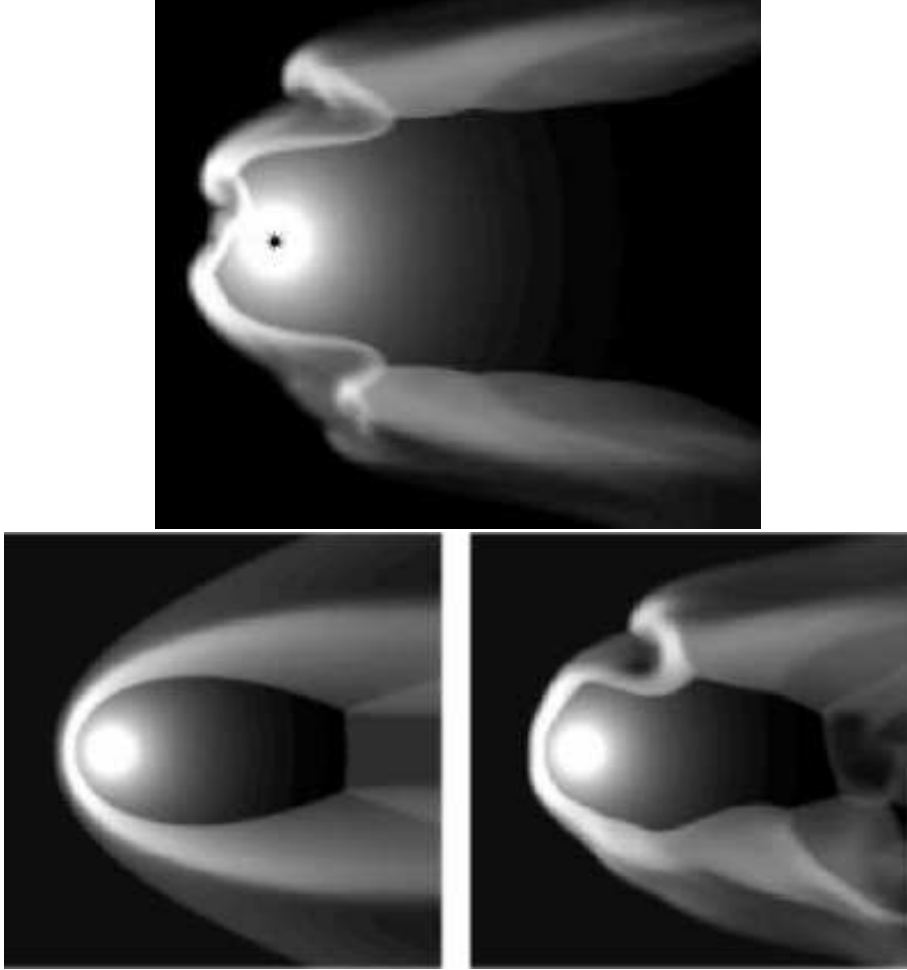
Figure 4.8.: Gas density maps during the AGB phase from numerical simulations by Wareing et al. (2007b,a). The upper panel shows a model with a space velocity of $125\,\mathrm{km\,s^{-1}}$. The bow shock bends towards the star like seen in the simulations by Comeron & Kaper (1998) and the observations of X Her. In addition this simulation produces wing structures as observed for TX Psc. In both lower panels the star moves with a space velocity of $75\,\mathrm{km\,s^{-1}}$ but has different mass loss rates. The model in the left panel has a low mass loss rate of $10^{-7}\,M_{\odot}\,\mathrm{yr^{-1}}$ whereas it is 50 times higher in the right panel. A higher mass loss rate favours the appearance of turbulences.

4.3.4. *o* **Ceti**

A special place among the AGB wind - ISM interaction simulations has *o* Ceti (Mira). Mira is the archetype of a variable AGB star and also shows strong indications of an interaction with the ISM. The high space velocity of approximately $110 \, \mathrm{km \, s^{-1}}$ produces a 4 pc long tail visible in UV (Martin et al. 2007). This was discussed before in Section 1.5.3 and shown in Fig. 1.13. This observation together with the high profile of the object made it a good case to prove stellar wind - ISM interaction models. Wareing et al. (2007c) manage to reproduce the long tail together with undulations in the shape. The tail though is much wider than the observed one and the authors estimate a kinematic age of the tail of 450000 years, about 15 times higher than the estimation of Martin et al. (2007). In this time span Mira travelled about 60 pc and entered into the low density environment of the Local Bubble which according to the authors can have an impact on shaping the tail of Mira.

Interesting is the consideration of Raga et al. (2008) to reproduce the observed filament structure of Mira's head with a latitude dependent wind. The density of the stellar wind is thus not isotropic but about 20 times denser at the equatorial region. The model produces when viewed from an appropriate direction two bow shocks along with a turbulent wake full of filamentary structures which correspond well to the observations by Martin et al. (2007). This model shows that a variation of the wind density alters the structure significantly. This also points out the possible importance of the bipolar outflows of TX Psc and X Her.

The most recent Mira model combines the Local Bubble idea and the equatorial density enhanced wind (Esquivel et al. 2010). It adopts the density gradient from Raga et al. (2008) and simulates the decreasing density of the ISM when Mira departs from the galactic plane and enters the Local Bubble. To achieve this, the density drops after 200000 years of evolution from $n_{\mathrm{H}} = 2$ to $0.05 \, \mathrm{cm^{-3}}$ and the temperature raises from $10^3 \, \mathrm{K}$ to $10^6 \, \mathrm{K}$. The tremendous consequences are presented in Fig. 4.9. The upper panel shows a model of Mira where the star stays outside the Local Bubble in a dense environment. It has a smooth bullet like shape with a narrow tail without perturbations. The lower panel is in contrast to that. It shows the same model entering the Local Bubble that goes along with a drop in density of the ambient medium and an increase of temperature. The outline of the tail is much more complex showing turbulences in all parts all along the tail. When changing the density of the ISM the space velocity of Mira becomes transonic what favours the mixing of the ISM with the wind. This result implements that also the properties of the ISM should carefully be taken into account. X Her and TX Psc have a slightly

lower space velocity than Mira but they might have also travelled dozens of pc in their AGB phase and entered into ISM regions with density gradients. However, this hypothesis is barely to prove and further investigations are beyond the scope of this work.

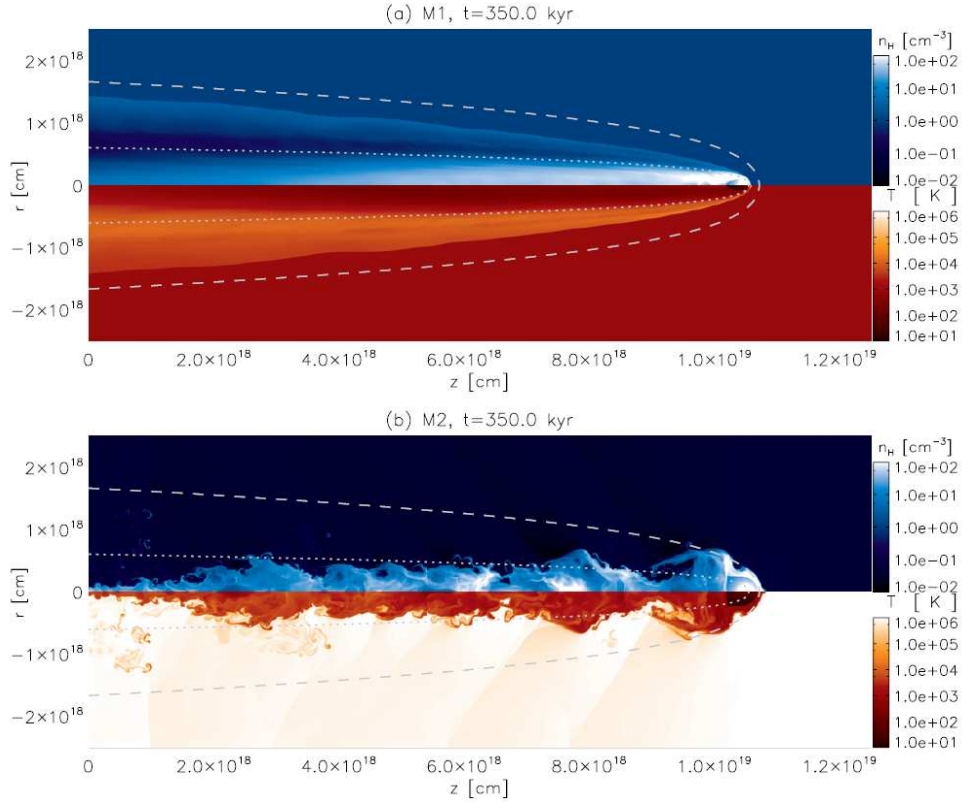Figure 4.9.: Density and temperature map of Mira after 350000 years of evolution in the AGB phase by Esquivel et al. (2010). The upper panel shows the model with a constant ISM density of $n_H=1\,cm^{-3}$. In the lower panel the density dropped after 200000 years to $n_H=0.05\,cm^{-3}$. While the upper panel model has a bullet like and smooth bow shock shape, the lower panel shows strong turbulences from head to tail.

Conclusion and outlook

The observations of X Her and TX Psc with Herschel reveal a variety of features in their stellar wind environments that can be assigned clearly to the interaction with the ISM. The stars have high velocities with respect to the ambient medium and the expected shape of the interaction zones, in form of a bow shock, is present. The outlines of both bow shocks however are different from the analytic solution. This fact can be explained by instabilities that occur due to the strength of cooling in the shock interface. Various simulations resemble the observed structures and allow some physical conclusions about the bow shock and the ambient medium.

The observation of bow shocks around AGB stars was so far limited by the sensitivity of IR telescopes. Until now it was only possible to detect them around four AGB stars: CW Leo, o Ceti, R Hya and α Ori. This border disappeared with the Herschel Space Observatory. X Her and TX Psc are part of a sample of 78 AGB stars observed in the framework of the MESS GT KP. A short overview with eight objects is given by Mayer et al. (2011b) but the whole sample reveals interaction features around more than 30 stars. An overview of the entire sample will be given in a forthcoming publication by Cox et al. (2011) where also some statistical aspects and new models are discussed. The sample shows morphologies like classic bow shocks but also disrupted structures that are predestined for a deeper examination. One of these cases is o Ceti, whose exceptional CSE shape can be traced back to the interaction of the stellar wind with the ISM, a fast bipolar outflow and the motion of a binary companion (Mayer et al. 2011a). Other objects though are still waiting for a proper analysis. This guarantees spectacular results for the future.

Bibliography

Aldcroft, T. L., Romani, R. W., & Cordes, J. M. 1992, ApJ, 400, 638

Arp, H. C., Baum, W. A., & Sandage, A. R. 1953, AJ, 58, 4

Baranov, V. B., Krasnobaev, K. V., & Kulikovskii, A. G. 1971, Soviet Physics Doklady, 15, 791

Barnbaum, C. & Hinkle, K. H. 1995, AJ, 110, 805

Bergeat, J., Knapik, A., & Rutily, B. 2001, A&A, 369, 178

Bethe, H. A. 1939, Physical Review, 55, 434

Blondin, J. M. & Koerwer, J. F. 1998, New Astron., 3, 571

Bondi, H. 1952, MNRAS, 112, 195

Borkowski, K. J., Sarazin, C. L., & Soker, N. 1990, ApJ, 360, 173

Bowen, G. H. 1988, ApJ, 329, 299

Brighenti, F. & D'Ercole, A. 1995, MNRAS, 277, 53

Burbidge, E. M., Burbidge, G. R., Fowler, W. A., & Hoyle, F. 1957, Reviews of Modern Physics, 29, 547

Castro-Carrizo, A., Quintana-Lacaci, G., Neri, R., et al. 2010, A&A, 523, A59+

Chandrasekhar, S. 1961, Hydrodynamic and hydromagnetic stability, ed. Chandrasekhar, S.

Chatterjee, S. & Cordes, J. M. 2002, ApJ, 575, 407

Comeron, F. & Kaper, L. 1998, A&A, 338, 273

Cordes, J. M., Romani, R. W., & Lundgren, S. C. 1993, Nat, 362, 133

Cox, N. L. J., Decin, L., Kerschbaum, F., et al. 2011, in preparation

Cruzalebes, P., Lopez, B., Bester, M., Gendron, E., & Sams, B. 1998, A&A, 338, 132

Danchi, W. C., Bester, M., Degiacomi, C. G., Greenhill, L. J., & Townes, C. H. 1994, AJ, 107, 1469

de Graauw, T., Helmich, F. P., Phillips, T. G., et al. 2010, A&A, 518, L6+

Dgani, R. & Soker, N. 1998, ApJ, 495, 337

Dgani, R., van Buren, D., & Noriega-Crespo, A. 1996a, ApJ, 461, 927

Dgani, R., van Buren, D., & Noriega-Crespo, A. 1996b, ApJ, 461, 372

Draine, B. T. 1981, ApJ, 245, 880

Dyck, H. M., van Belle, G. T., & Thompson, R. R. 1998, AJ, 116, 981

Dyson, J. E. 1975, , 35, 299

Eriksson, K., Gustafsson, B., Johnson, H. R., et al. 1986, A&A, 161, 305

Esquivel, A., Raga, A. C., Cantó, J., et al. 2010, ApJ, 725, 1466

Falle, S. A. E. G. 1975, A&A, 43, 323

Famaey, B., Jorissen, A., Luri, X., et al. 2005, A&A, 430, 165

Feast, M. W. & Whitelock, P. A. 2000, MNRAS, 317, 460

Freytag, B. 2006, in EAS Publications Series, Vol. 21, EAS Publications Series, ed. M. Rieutord & B. Dubrulle, 325–333

Gardan, E., Gérard, E., & Le Bertre, T. 2006, MNRAS, 365, 245

Geise, K. M., Ueta, T., Speck, A. K., Izumiura, H., & Stencel, R. E. 2010, in Bulletin of the American Astronomical Society, Vol. 42, American Astronomical Society Meeting Abstracts #215, 431.14–+

González Delgado, D., Olofsson, H., Schwarz, H. E., et al. 2003, A&A, 399, 1021

Greenstadt, E. W., Green, I. M., & Colburn, D. S. 1968, Science, 162, 898

Griffin, M. J., Abergel, A., Abreu, A., et al. 2010, A&A, 518, L3+

Groenewegen, M. A. T., Waelkens, C., Barlow, M. J., et al. 2011, A&A, 526, A162+

Gull, T. R. & Sofia, S. 1979, ApJ, 230, 782

Gurzadian, G. A. 1969, Planetary nebulae, 913–+

Gustafsson, B., Bell, R. A., Eriksson, K., & Nordlund, A. 1975, A&A, 42, 407

Gustafsson, B. & Höfner, S. 2004, Atmospheres of AGB Stars, ed. Habing, H. J. & Olofsson, H.

Habing, H. & Olofsson, H. 2004, AGB Stars: History, Structure, and Characteristics, ed. Habing, H. J. & Olofsson, H.

Hertzsprung, E. 1911, Publikationen des Astrophysikalischen Observatoriums zu Potsdam, 63

Heske, A., te Lintel Hekkert, P., & Maloney, P. R. 1989, A&A, 218, L5

Hinkle, K. H., Lebzelter, T., Joyce, R. R., & Fekel, F. C. 2002, AJ, 123, 1002

Huggins, P. J., Mauron, N., & Wirth, E. A. 2009, MNRAS, 396, 1805

Iben, Jr., I. 1975, ApJ, 196, 525

Iben, Jr., I. 1991, ApJS, 76, 55

Johnson, D. R. H. & Soderblom, D. R. 1987, AJ, 93, 864

Jorissen, A., Mayer, A., van Eck, S., et al. 2011, A&A, 532, A135+

Kahane, C. & Jura, M. 1996, A&A, 310, 952

Kerschbaum, F. & Hron, J. 1994, A&AS, 106, 397

Kippenhahn, R. & Weigert, A. 1994, Stellar Structure and Evolution, ed. Kippenhahn, R. & Weigert, A.

Knapp, G. R. 1986, ApJ, 311, 731

Kwok, S., Volk, K., & Bidelman, W. P. 1997, ApJS, 112, 557

Ladjal, D., Barlow, M. J., Groenewegen, M. A. T., et al. 2010, A&A, 518, L141+

Lambert, D. L., Gustafsson, B., Eriksson, K., & Hinkle, K. H. 1986, ApJS, 62, 373

Lamers, H. J. G. L. M. & Cassinelli, J. P. 1999, Introduction to Stellar Winds, ed. Lamers, H. J. G. L. M. & Cassinelli, J. P.

Lattanzio, J. C. & Wood, P. R. 2004, Evolution, Nucleosynthesis, and Pulsation of AGB Stars, ed. Habing, H. J. & Olofsson, H.

Le Bertre, T., Matsuura, M., Winters, J. M., et al. 2001, A&A, 376, 997

Lu, P. K., Demarque, P., van Altena, W., McAlister, H., & Hartkopf, W. 1987, AJ, 94, 1318

Mac Low, M., van Buren, D., Wood, D. O. S., & Churchwell, E. 1991, ApJ, 369, 395

Martin, D. C., Seibert, M., Neill, J. D., et al. 2007, Nat, 448, 780

Matthews, L. D., Libert, Y., Gérard, E., et al. 2011, AJ, 141, 60

Mayer, A., Jorissen, A., Kerschbaum, F., et al. 2011a, A&A, 531, L4+

Mayer, A., Jorissen, A., Kerschbaum, F., et al. 2011b, in Why galaxies care about AGB stars II, ed. T. Lebzelter, Astronomical Society of the Pacific Conference Series, in press

Meaburn, J., López, J. A., Boumis, P., Lloyd, M., & Redman, M. P. 2009, A&A, 500, 827

Mihalas, D. & Binney, J. 1981, Galactic astronomy: Structure and kinematics /2nd edition/, ed. Mihalas, D. & Binney, J.

Nakashima, J.-i. 2005, ApJ, 620, 943

Olofsson, H., Eriksson, K., Gustafsson, B., & Carlstrom, U. 1993, ApJS, 87, 267

Oort, J. H. 1951, in Problems of Cosmical Aerodynamics, 118–+

Ottensamer, R. & Kerschbaum, F. 2008, in Society of Photo-Optical Instrumentation Engineers (SPIE) Conference Series, Vol. 7019, Society of Photo-Optical Instrumentation Engineers (SPIE) Conference Series

Ottensamer, R., Luntzer, A., Mecina, M., et al. 2011, in Astronomical Society of the Pacific Conference Series, in press

Parker, E. N. 1958, ApJ, 128, 664

Phillips, J. P., Reay, N. K., & Worswick, S. P. 1977, A&A, 61, 695

Pilbratt, G. L., Riedinger, J. R., Passvogel, T., et al. 2010, A&A, 518, L1+

Poglitsch, A., Waelkens, C., Geis, N., et al. 2010, A&A, 518, L2+

Quirrenbach, A., Mozurkewich, D., Hummel, C. A., Buscher, D. F., & Armstrong, J. T. 1994, A&A, 285, 541

Raga, A. C., Cabrit, S., & Canto, J. 1995, MNRAS, 273, 422

Raga, A. C., Cantó, J., De Colle, F., et al. 2008, ApJL, 680, L45

Raskin, G., van Winckel, H., Hensberge, H., et al. 2011, A&A, 526, A69+

Reimers, D. 1975, Circumstellar envelopes and mass loss of red giant stars, ed. Baschek, B., Kegel, W. H., & Traving, G., 229–256

Richichi, A., Chandrasekhar, T., Lisi, F., et al. 1995, A&A, 301, 439

Roussel, H. 2011, AJ

Russell, H. N. 1914, Popular Astronomy, 22, 275

Sahai, R. & Chronopoulos, C. K. 2010, ApJL, 711, L53

Salpeter, E. E. 1952, ApJ, 115, 326

Sandage, A. R. & Schwarzschild, M. 1952, ApJ, 116, 463

Schönrich, R., Binney, J., & Dehnen, W. 2010, MNRAS, 403, 1829

Schwarzschild, M. & Härm, R. 1965, ApJ, 142, 855

Simis, Y. & Woitke, P. 2004, Atmospheres of AGB Stars, ed. Habing, H. J. & Olofsson, H.

Sloan, G. C., Kraemer, K. E., Goebel, J. H., & Price, S. D. 2003, ApJ, 594, 483

Smith, H. 1976, MNRAS, 175, 419

Soker, N., Borkowski, K. J., & Sarazin, C. L. 1991, AJ, 102, 1381

Stencel, R. E., Pesce, J. E., & Hagen Bauer, W. 1988, AJ, 95, 141

Strong, I. B. 1968, in Astrophysics and Space Science Library, Vol. 10, Physics of the Magnetosphere, ed. R. D. L. Carovillano & J. F. McClay, 376–+

Sugimoto, D. & Nomoto, K. 1975, PASJ, 27, 197

Tsuji, T. 1986, A&A, 156, 8

Ueta, T. 2009, in AGB Stars and Related Phenomena, ed. T. Ueta, N. Matsunaga, & Y. Ita, 20–+

Ueta, T. 2011, in Why galaxies care about AGB stars II, ed. T. Lebzelter, Astronomical Society of the Pacific Conference Series, in press

Ueta, T., Izumiura, H., Yamamura, I., et al. 2008, PASJ, 60, 407

Ueta, T., Speck, A. K., Stencel, R. E., et al. 2006, ApJL, 648, L39

van Buren, D., Mac Low, M., Wood, D. O. S., & Churchwell, E. 1990, ApJ, 353, 570

van Buren, D. & McCray, R. 1988, ApJL, 329, L93

van der Veen, W. E. C. J. & Habing, H. J. 1988, A&A, 194, 125

van Leeuwen, F. 2007, A&A, 474, 653

Villaver, E., García-Segura, G., & Manchado, A. 2003, ApJL, 585, L49

Vishniac, E. T. 1994, ApJ, 428, 186

Wareing, C. J., O'Brien, T. J., Zijlstra, A. A., et al. 2006a, MNRAS, 366, 387

Wareing, C. J., Zijlstra, A. A., & O'Brien, T. J. 2007a, MNRAS, 382, 1233

Wareing, C. J., Zijlstra, A. A., & O'Brien, T. J. 2007b, ApJL, 660, L129

Wareing, C. J., Zijlstra, A. A., O'Brien, T. J., & Seibert, M. 2007c, ApJL, 670, L125

Wareing, C. J., Zijlstra, A. A., Speck, A. K., et al. 2006b, MNRAS, 372, L63

Wasatonic, R. 1995, Information Bulletin on Variable Stars, 4159, 1

Weaver, R., McCray, R., Castor, J., Shapiro, P., & Moore, R. 1977, ApJ, 218, 377

Wilkin, F. P. 1996, ApJL, 459, L31+

Wilkin, F. P., Canto, J., & Raga, A. C. 1997, in IAU Symposium, Vol. 182, Herbig-Haro Flows and the Birth of Stars, ed. B. Reipurth & C. Bertout, 343–352

Wirsich, J. 1991, ApJ, 377, 285

Young, K., Phillips, T. G., & Knapp, G. R. 1993, ApJS, 86, 517

A. Appendix

A.1. Constants and parameters

Table A.1.: Used constants and parameters.

Name	Symbol	Value
Atomic mass unit	m_H	$1.661 \text{ x } 10^{-27}\,\mathrm{kg}$
Gravitational constant	G	$6.673 \text{ x } 10^{-11}\,\mathrm{m^3\,kg^{-1}\,s^{-2}}$
Speed of light	c	$2.998 \text{ x } 10^{8}\,\mathrm{m\,s^{-1}}$
Boltzmann constant	k	$1.381 \text{ x } 10^{-23}\,\mathrm{J\,K^{-1}}$
Planck constant	h	$6.626 \text{ x } 10^{-34}\,\mathrm{J\,s}$
Solar mass	$M_\odot$	$1.989 \text{ x } 10^{30}\,\mathrm{kg}$
Solar luminosity	$L_\odot$	$3.839 \text{ x } 10^{26}\,\mathrm{J\,s^{-1}}$
Solar radius	$R_\odot$	$6.955 \text{ x } 10^{8}\,\mathrm{m}$
Parsec	pc	$3.086 \text{ x } 10^{16}\,\mathrm{m}$
Astronomical unit	AU	$1.496 \text{ x } 10^{11}\,\mathrm{m}$
Electron volt	eV	$1.602 \text{ x } 10^{-19}\,\mathrm{J}$
Jansky	Jy	$10^{-26}\,\mathrm{J\,s^{-1}\,m^{-2}\,Hz^{-1}}$

A.2. Wilkin fit factors

Table A.2.: Variation of $R_{0,\mathrm{d}}$ ($R_{0,\mathrm{d}} = R_0/q(i)$) with inclination angle i.

i	q	i	q	i	q	i	q
0	1.00000	1	1.00026	2	1.00046	3	1.00107
4	1.00168	5	1.00270	6	1.00372	7	1.00516
8	1.00659	9	1.00843	10	1.01028	11	1.01256
12	1.01485	13	1.01758	14	1.02032	15	1.02349
16	1.02667	17	1.03030	18	1.03394	19	1.03806
20	1.04218	21	1.04680	22	1.05142	23	1.05656
24	1.06171	25	1.06742	26	1.07313	27	1.07942
28	1.08571	29	1.09260	30	1.09950	31	1.10704
32	1.11459	33	1.12284	34	1.13109	35	1.14007
36	1.14905	37	1.15886	38	1.16867	39	1.17936
40	1.19004	41	1.20165	42	1.21326	43	1.22591
44	1.23856	45	1.25233	46	1.26610	47	1.28113
48	1.29615	49	1.31258	50	1.32900	51	1.34697
52	1.36494	53	1.38462	54	1.40431	55	1.42600
56	1.44769	57	1.47158	58	1.49548	59	1.52200
60	1.54851	61	1.57805	62	1.60759	63	1.64064
64	1.67369	65	1.71095	66	1.74820	67	1.79057
68	1.83294	69	1.88161	70	1.93028	71	1.98684
72	2.04339	73	2.11019	74	2.17700	75	2.25738
76	2.33776	77	2.43710	78	2.53644	79	2.66350
80	2.79056	81	2.96167	82	3.13279	83	3.38170
84	3.63061	85	4.04468	86	4.45876	87	5.38820
88	6.31764						

B. Curriculum Vitae

Personal Information

Name	Andreas Mayer
Address	Wienerbergstraße 20/4/9, 1120 Wien, Austria
Telephone	+43–6502035399
E-mail	a.mayer@univie.ac.at
Birthday	16th of January, 1984
Birthplace	Heilbronn, Germany
Nationality	German
Sex	Male

Education

–2003	Grammar School: Friedrich-von-Alberti Gymnasium, Bad Friedrichshall, Germany with qualification for university entrance
2003–2004	Sabbatical year in South America
2004–2011	Student at the University of Vienna, Department of Astronomy
2008	Bachelor degree in Astronomy with thesis "Nucleosynthesis: Chemical elements and their astrophysical origin"
2011	Master degree in Astronomy with thesis "X Herculis and TX Piscium: The interaction of their stellar winds with the interstellar medium observed by Herschel"

Publications

2011   *Herschel's view into Mira's head*,
A. Mayer, A. Jorissen, F. Kerschbaum, S. Mohamed,
S. van Eck, R. Ottensamer, J.A.D.L. Blommaert,
L. Decin, M.A.T. Groenewegen, Th. Posch,
B. Vandenbussche, and Ch. Waelkens, 2011,
A&A 531, L4+

2011   *X Her and TX Psc: Two cases of ISM interaction
with stellar winds observed by Herschel*,
A. Jorissen, A. Mayer, S. van Eck, R. Ottensamer,
F. Kerschbaum, T. Ueta, P. Bergman,
J.A.D.L. Blommaert, L. Decin, M.A.T. Groenewegen,
J. Hron, W. Nowothny, H. Olofsson, Th. Posch,
L.O. Sjouwerman, B. Vandenbussche,
and Ch. Waelkens, 2011, A&A 532, A165+

2011   *Headwind: The AGB-ISM frontier*,
A. Mayer, A. Jorissen, F. Kerschbaum, S. van Eck,
M. Mecina, R. Ottensamer, A. Luntzer,
J.A.D.L. Blommaert, L. Decin, M.A.T. Groenewegen,
Th. Posch, B. Vandenbussche, and Ch. Waelkens,
2011, in *Why Galaxies Care About AGB Stars II*,
Astronomical Society of the Pacific Conference Series,
in press

Conferences

2010   Why Galaxies Care About AGB Stars II,
Vienna, with poster presentation